

FILTERING OF ACOUSTIC INFORMATION FROM AERO-OPTICAL MEASUREMENTS

A Dissertation

Submitted to the Graduate School
of the University of Notre Dame
in Partial Fulfillment of the Requirements
for the Degree of

Doctor of Philosophy

by
Brian Lowell Catron

R. Mark Rennie , Co-Director

Eric J. Jumper, Co-Director

Graduate Program in Aerospace and Mechanical Engineering

Notre Dame, Indiana

January 2022

FILTERING OF ACOUSTIC INFORMATION FROM AERO-OPTICAL MEASUREMENTS

Abstract

by

Brian Lowell Catron

With development of new airborne optical systems, there is a significant amount of effort being put into maximizing the farfield performance of these optical systems. To meet this goal, the root mean square of the optical path difference, OPD_{RMS} , over the aperture, a measure of the nearfield optical distortions, is being reduced as much as possible. Part of this development process involves testing models of these systems with various configurations in wind tunnels. In these tests, the optical disturbances due to the testing environment are becoming a large percentage of the measured optical disturbances. It is now a necessity to be able to identify, measure, and remove the various noise sources that appear in aero-optical measurements that take place in wind tunnels.

One of the primary sources of signal noise in these measurements, is acoustics. Both the wing-tunnel fan and the flow through out the tunnel generate large amounts of acoustic noise that travel throughout the tunnel as acoustic duct modes. The fan generates strong narrow-band signals at the blade-passing frequency and its harmonics. There are also significant broad-band acoustic duct mode signals along with vibration related signals and strong mostly-steady optical lensing signals that add to the overall measurement.

A significant portion of this dissertation is dedicated to analyzing wind-tunnel optical wavefront data in multidimensional spectral space. The signal identification and filtering mostly take place in the multidimensional spectrum, where the optical wavefront is not only split into its temporal frequency components but also its spatial frequency components. A combination of three filters is able to remove most of the noise signals while retaining most of the aero-optical signal. A velocity filter, which retains a narrow band of signal that is traveling within a small velocity range, is able to remove most of the broad-band signal noise, especially at higher temporal-frequencies. A backward filter, which retains only the portion of a signal that is traveling in the direction of flow, removes signal that the velocity filter is not able to at lower temporal-frequencies. Finally a baseline filter identifies the baseline spectrum and removes narrow-band peaks.

To my wife Karen & our son Arthur

CONTENTS

Figures	v
Tables	ix
Symbols	xi
Acknowledgments	xv
Chapter 1: Introduction	1
Chapter 2: Literature Review	7
2.1 Aero-Optics	7
2.1.1 Typical Optical Wavefront Measurement System	12
2.1.2 Boundary Layer Optical Distortions	16
2.2 Duct Acoustics	16
2.2.1 Characteristic Equations of Cross-Sections	20
Chapter 3: Aero-Optical and Acoustical Coupling	23
3.1 Simulating an Optical Wavefront Measurement from an Acoustic Field Function	23
3.2 Simple Examples of Acoustic-Optical Coupling	25
3.2.1 Planar Acoustic Waves	25
3.2.2 Spherical Acoustic Waves	28
3.2.2.1 Theoretical OPD Calculations	29
3.2.2.2 Measurement of a Spherical Acoustic Wave with an Optical Beam	30
3.3 Estimating the Acoustic Field Inside a Wind-Tunnel Test-Section	34
3.3.1 Mode-Marching Method Procedure	37
3.3.2 University of Notre Dame White Field Wind-Tunnel Simulation	38
3.4 Summary	45
Chapter 4: Multidimensional Spectral Estimation of Optical Wavefronts	47
4.1 One-Dimensional Power Spectrum Calculation	50
4.2 N-Dimensional Power Spectra Calculation	51
4.3 Non-Rectangular Spatial Windows	52
4.4 Wavefront Multidimensional Spectrum	53
4.4.1 2-D Slices of the Multidimensional Spectral Estimation	56
4.4.2 3-D Representations of Multidimensional Spectral Estimation	60
4.4.3 Acoustic Cone	66
4.4.4 Signal Aliasing	68
4.5 Summary	74

Chapter 5: Synthetic Wavefront	75
5.1 General Spectrum Construction	76
5.2 Aero-Optical Signal	79
5.3 Stationary Mode Signals	80
5.4 Sound and Vibration Signals	80
5.4.1 Blade-Passing Frequency Disturbance	80
5.4.2 Acoustic Cone	81
5.5 Mean-Lensing Signal	83
5.6 Background Noise Signal	83
5.7 Synthetic Wavefront Creation	84
5.8 Comparison to Measured Data	84
Chapter 6: Wavefront Multidimensional Spectral Filtering Techniques	89
6.1 Temporal Filter Methods	90
6.2 Upstream/Downstream Moving	92
6.3 Velocity Filtering	96
6.4 Baseline Spectrum	101
6.5 Basic Filter Summary	101
6.6 Multiple Sensor Filtering of Optical Wavefronts	103
6.6.1 Optical Tip and Tilt	104
6.6.2 LSE-SPOD	105
6.6.3 Filtering Experimental Data	107
6.7 Results	110
Chapter 7: Combination of Filters	117
7.1 Velocity and LSE-SPOD Filter	117
7.2 Backward, Velocity, and Baseline Filter	119
Chapter 8: Conclusion	125
8.1 Filtering of Optical Wavefronts	127
8.1.1 Single Sensor Filters	127
8.2 Other Useful Products	128
8.2.1 Synthetic Wavefront	128
8.2.2 Measuring Acoustic Field Optically	128
8.2.3 Acoustic Mode-Marching	128
8.3 Recommendations For Future Research	129
Bibliography	131

FIGURES

1.1	Diffraction-limited far-field intensity of a beam normalized by the performance at 1- μm .	2
1.2	Strehl ratio due to the OPD _{RMS} of the Airborne Laser Laboratory (ALL) at various laser wavelengths. ALL had an estimated Strehl ratio of 95% with its 10.6- μm laser.	3
1.3	Hypothetical iterative design process of an airborne directed-energy system. The required performance level is shown by the red line and the testing environment's contamination is shown by the orange line.	4
2.1	Gladstone-Dale constant for air over the visible wavelength range.	8
2.2	(a) Diffraction limited on target intensity as a function of wavelength normalized by the value at $\lambda = 1 \mu\text{m}$. (b) Strehl ratio as a function of wavelength for an aberration that gives SR = 0.95 at $\lambda = 10.6 \mu\text{m}$.	12
2.3	OPD _{RMS} values necessary to obtain Strehl ratios of 0.9, 0.7, and 0.5 over a range of wavelengths.	13
2.4	Typical double-pass optical wavefront measurement setup.	14
2.5	Diagram of a Shack-Hartmann wavefront sensor comprised of four lenslets. The black line represents the perturbed wavefront and the red line the mean slope over each lenslet. The focal point of the wavefront is shifted by Δx from the center-line of the lenslet based on the mean slope of the wavefront. [1]	15
2.6	Aperture size correction for OPD _{RMS} (Figure 18 in Gordeyev [23]).	17
2.7	Duct with a rectangular cross-section.	17
2.8	Characteristic solutions to Equation 2.36 with rigid wall in a rectangular cross-section where m=0:2 and n=0:3. Nodal lines are depicted by the dot-dash lines. The cross-sectional wave numbers, k_m , listed are for a duct of unit length and height.	21
2.9	Characteristic solutions to Equation 2.36 with rigid wall in a circular cross-section where m=0:2 and n=0:3. Nodal lines are depicted by the dot-dash lines. The cross-sectional wave numbers, k_m , listed are for a duct of unit radius.	22
3.1	General geometry for various sample calculations for showing the acoustic-optical coupling effect.	26
3.2	Theoretical time-averaged OPD _{RMS} per meter of beam propagation as a function of sound pressure level, SPL, for several Λ/A_p ratios and $\theta = 0$.	27
3.3	Theoretical time-averaged OPD _{RMS} for a RMS sound pressure of 1 Pa (SPL of 94 dB), l_n of 1 m, and various angles and Λ/A_p ratios.	27
3.4	Theoretical time-averaged OPD _{RMS} for the two acoustic waves ($u+c$ and $u-c$) for the blade pass frequency (534 Hz) at Mach 0.6 with a RMS sound pressure of 1 Pa (SPL of 94 dB), l_n of 1 m, and A_p of 15 cm.	28
3.5	Diagram of the geometry used in the spherical wave simulation.	30

3.6	Theoretical time-averaged OPD _{RMS} for a spherical acoustic wave. The top plot shows a perfect spherical acoustic signal integrated over ± 5 m. The bottom plot shows has a Tukey window applied along the beam length to partially emulate source directivity which significantly reduces the measured oscillations.	31
3.7	Spherical acoustic wave measurement test.	32
3.8	Comparison of measured wavefront to simulated ones for the highest-amplitude speaker excitation at each frequency.	35
3.9	Deformable mesh for calculating the acoustic modes in the circular to square transitions at three stages.	36
3.10	CAD model of the University of Notre Dame Whitefield wind-tunnel. The specifications of the tunnel at the numbered cross-sections are shown in Table 3.3.	40
3.11	Wind-tunnel discretization at a Mach number of 0.6. The solid lines in the sound transmission plots represent the transmitted pressure ratio while the dotted lines represent the reflected pressure ratio.	41
3.12	Cross-sectional slices of the acoustic field through the circle to square transition for the acoustic waves traveling upstream. Left side are the waves traveling from the fan at a phase of 0 radians and the right side at a phase of $\pi/2$ radians. The top plots are the fan acoustic field, the middle plots are halfway through the transition, and the bottom plots are just into the square duct.	42
3.13	Cross-sectional acoustic field slices in the center of the test-section at various initial phase angles.	43
3.14	The real component of the acoustic mode coefficients making up the upstream-traveling acoustic field in the middle of the test-section as a function of the initial phase angle.	44
3.15	The real component of the acoustic mode coefficients making up the downstream-traveling acoustic field in the middle of the test-section as a function of the initial phase angle.	45
3.16	Comparison of a measured optical wavefront and a simulated one passing through the estimated acoustic field.	46
4.1	Multidimensional spectral estimation plot example and comparison to traditional power spectrum measurements. A single row of an optical wavefront measurement was used in this example. The top plot shows the typical power spectrum averaged over the entire row of data. Both the middle and bottom plots show the multidimensional spectrum plot with the y-axis as spatial frequency in the middle and velocity in the bottom assuming $u = f/\xi_x$	48
4.2	Horizontal moving optical disturbances comparison. The top plot shows a slice of the three-dimensional spectrum focusing on the plane waves that are traveling in the horizontal direction. The middle plot is a recreation of the two-dimensional spectrum by integrating through the the vertical spatial frequencies. The bottom plot is the two-dimensional spectrum.	55
4.3	Recovery of time-based power spectrum from two-dimensional spectral estimate. . .	56
4.4	Horizontal and vertical moving optical disturbances. This is the same data as presented in Figure 4.1 but after calculating the full three-dimensional spectral estimate. These optical disturbances are plane waves that are traveling solely in their respective directions.	57
4.5	Temporal-frequency slices at 5 and 10 kHz with the various horizontal velocities labeled.	58
4.6	Three-dimensional view of the multidimensional spectral plot showing an isosurface at a power of $10^{-14} \mu\text{m}^2/\text{Hz}/\text{m}^{-2}$	61

4.7	Multidimensional spectral estimate isosurfaces as the Mach number increased from 0.3 to 0.5. The isosurfaces are all shown at a power of $10^{-14} \mu\text{m}^2/\text{Hz}/\text{m}^{-2}$	62
4.8	Multidimensional spectral estimate isosurfaces of different viewing angles through the test section at a Mach number of 0.5. The isosurfaces are all shown at a power of $10^{-14} \mu\text{m}^2/\text{Hz}/\text{m}^{-2}$	64
4.9	Multidimensional spectral estimate slices at various temporal frequencies.	65
4.10	Acoustic duct mode lines showing the spatial frequency location as a function of temporal frequency, Mach number, and mode number.	67
4.11	Acoustic duct mode lines as a function of viewing angle, γ , at a Mach number of 0.6.	69
4.12	Spectrum tiling method to identify aliased data. Shown here as the horizontal moving (stream-wise) disturbance slices, along with lines representing the various characteristic velocities. The thick outline shows the extent of the base spectrum with the thick dashed outlines representing the various tiles of that base spectrum.	70
4.13	Artificially increased temporal sample rate using a dispersion analysis. The black box represents original dispersion plot.	72
4.14	Three-dimensional tiling of an isosurface of the spectrum at a power of $10^{-14.5} \mu\text{m}^2/\text{Hz}/\text{m}^{-2}$	73
5.1	Multidimensional spectral estimation that the synthetic wavefront is based on.	77
5.2	Synthetic wavefront input dispersion plot of an aero-optical signal and various signal corruption components. The aero-optical signal is shown in red, the stationary modes in blue, duct acoustics in magenta, blade-passing frequency related corruption in green, slowly varying mean-lensing in yellow, and background in cyan.	78
5.3	Sample frames from the synthetic wavefront with the total wavefront signal on top and the aero-optical only signal bottom. Flow is from right to left.	85
5.4	Synthetic wavefront output dispersion plot of an aero-optical signal and various signal corruption components.	86
6.1	The <i>opdrms</i> of high-pass temporal filtered wavefronts relative to the <i>opdrms</i> of the aero-optical only unfiltered wavefront (top). Power spectra of both of the simulated wavefront versions (bottom).	91
6.2	Measured wavefronts filtered at the blade-passing frequency (532 ± 10 Hz). The left column is band-stop filtered while the right is band-pass filtered.	93
6.3	Multidimensional spectral isosurface of the synthetic wavefront with a downstream filter in place.	95
6.4	Multidimensional spectral isosurface of the synthetic wavefront with a low-pass velocity filter in place.	97
6.5	Boundary layer velocity measurement of the synthetic wavefront using a combination of a low-pass velocity filter and a high-pass radial frequency filter. The maximum value at $u_{BL}/U = 0.8$ corresponds with the actual value used in the creation of the synthetic wavefront.	99
6.6	Velocity low-pass filter used to determine the mean disturbance velocity of measured data presented in Figure 4.6. The velocity in the x-direction was measured to be 152 m/s and 3 m/s in the y-direction.	100
6.7	Baseline spectrum estimation. The top left plot shows the unfiltered multidimensional spectrum and the baseline spectrum on the top right. The green line in each of these plots represents the location at which the spectra in the bottom plot is shown.	102

6.8	Schematic of the SPOD algorithm (taken from [53]). The numbers in parentheses denote the equations used.	105
6.9	The locations of some of the additional sensors used in the LSE-SPOD filtering. The sensors are labeled with the sensor numbers, see Table 6.1.	108
6.10	CAD drawing view of the inside of the test-section with some of the sensor locations labeled. Flow is from left to right. The numbers in the circles are the sensor numbers on the model side of the test-section. The numbers in the square are the sensor numbers opposite of the model side. The dashed line represents the optics window opposite of the model for the beam angle of 90°. The window was moved up and downstream depending on the beam angle.	108
6.11	Power-spectra of the additional sensor measurements at the three Mach numbers tested. The x-axis is in Strouhal number per characteristic length (St/l).	111
6.12	A multidimensional power spectrum of an unfiltered wavefront and the same wavefront filtered with the LSE-SPOD method using all 16 additional microphone or accelerometer measurements.	112
6.13	A multidimensional power spectrum of an unfiltered wavefront and the same wavefront filtered with the LSE-MSPOD method using all 16 additional microphone or accelerometer measurements.	113
7.1	Percent reduction in OPD_{RMS} from the tip/tilt removed case using LSE-SPOD filtering.	118
7.2	Reduction in $OPD_{RMS}(t)$ as a function of temporal frequency using 16 sensors with LSE-SPOD in the $M=0.5$ case when compared to tip/tilt removal.	119
7.3	Multidimensional spectra of three single sensor filtering techniques and a combination filter.	121
7.4	Multidimensional spectral slices for the various single sensor filtering techniques showing the horizontal moving plane waves.	122
8.1	Multidimensional spectral estimation of an optical wavefront measurement made in a wind tunnel.	126

TABLES

3.1	Curve fit values for Figure 3.6 and Equation 3.14	33
3.2	Comparison of microphone and wavefront computation of $ A_0 $	34
3.3	Wind-tunnel cross-section specifications	39
5.1	Values used in the construction of the multidimensional spectrum for the boundary layer signal	79
5.2	Values used in the construction of the multidimensional spectrum for the signal of the stationary modes	80
5.3	Values used in the construction of the multidimensional spectrum for the blade-passing frequency disturbance	81
5.4	Values used in the construction of the multidimensional spectrum for the acoustic cone disturbance	82
5.5	Values used in the construction of the multidimensional spectrum for the mean-lensing disturbance	83
6.1	Additional sensors used the the LSE-SPOD filtering.	109
6.2	OPD_{RMS} (μm) comparison of using different combinations of additional sensor information in the LSE-MSPOD filtering process.	114
7.1	OPD_{RMS} (μm) comparison of using LSE-MSPOD filtering process when combined with a velocity filter.	118
7.2	Summary of single sensor filters	123

SYMBOLS

A_0	Fluctuating pressure strength of a spherical wave
Ap	Aperture size - Typically diameter
c	Speed of sound
c_w	Windowing correction factor
C_f	Coefficient of friction
C_m	Pressure coefficient for mode m
f	Temporal frequency ($\omega = 2\pi f = \frac{2\pi}{T}$)
f_s	Sample rate
FFT	Fast Fourier Transform
FT	Fourier Transform
I	Actual on target irradiance
I_0	Diffraction-limited irradiance
j	$\sqrt{-1}$
k	Wavenumber ($k = 2\pi\xi = \frac{2\pi}{\Lambda}$)
K_{GD}	Gladstone-Dale constant
l	Duct length
m	Acoustic mode m
M	Mach number
n	Index of refraction
	Acoustic mode n
n	Normal vector
N	Sample count
OPD	Optical path difference
OPD_{RMS}	Time-averaged spatial OPD root-mean-square
$OPD_{RMS}(t)$	Spatial OPD root-mean-square as a function of time
OPL	Optical path length
p	Fluid pressure

p_0	Reference pressure ($20 \mu\text{Pa}$ for air)
P	Laser output power
r	Distance from center of disturbance
R	Distance from center of disturbance to measurement beam
r_{01}	Distance from a point in the observation plane to point in the aperture plane
SPL	Sound pressure level
SR	Strehl ratio ($\text{SR} = I/I_0$)
S_{xx}	Power spectra
T	Fluid temperature
	Temporal period ($\omega = 2\pi f = \frac{2\pi}{T}$)
u	Fluid velocity
u_d	Disturbance velocity
U	Free-stream fluid velocity
	Complex amplitude in diffraction
w	Windowing function
z	Distance from aperture
GREEK	
γ	Beam angle relative to flow direction (0° upstream, 180° downstream)
δ	Boundary layer thickness
θ	Deflection angle
	Angle of beam from perpendicular to wave propagation
λ	Wavelength of light
Λ	Wavelength of disturbance ($k = 2\pi\xi = \frac{2\pi}{\Lambda}$)
ξ	Spatial frequency ($k = 2\pi\xi = \frac{2\pi}{\Lambda}$)
ρ	Fluid density
σ^2	Signal total energy
Ψ_m	m^{th} mode characteristic function for the cross-section
ω	Angular temporal frequency ($\omega = 2\pi f = \frac{2\pi}{T}$)
SUB/SUPERSCRIPTS	
$_m$	m^{th} mode
RMS	Root mean square
T	Total fluid properties
x	Duct property in the x-direction

y	Duct property in the y-direction
z	Duct property in the z-direction
zm	m^{th} mode in the z-direction
0	Fluid properties at average conditions
	Observation plane coordinates
1	Aperture plane coordinates
$-$	Average fluid properties
$\hat{\cdot}$	Complex fluid properties
$'$	Fluctuating fluid properties
\rightarrow	Vector quantity
$*$	Complex conjugate
$+$	Acoustic mode traveling in the direction of flow
$-$	Acoustic mode traveling upstream
∞	Free-stream fluid properties

ACKNOWLEDGMENTS

I would like to thank my advisors R. Mark Rennie and Eric J. Jumper along with Stanislav Gordeyev for helping me grow not only in my ability to take measurements, but also as a researcher, designing experiments and analyzing the data. I would also like to think my fellow grad students, particularly Jon Wells, Barry Pawlowski, Matt Kalensky, and Matt Kemnetz, who endured alongside me. You helped me when I needed help and gave me some interesting problems to solve.

Most of all I would like to thank my family. My parents, Kevin and Nila, who pushed me to meet my potential when I was younger. I would like to think you for the sacrifices you made for my benefit. Thank you Karen, my wife, for putting up with my slow progress at times. Thank you for everything you do for me and our child. Arthur, watching you grow and learn brings me joy everyday.

CHAPTER 1

INTRODUCTION

There have been two major attempts to field a directed-energy system aboard an aircraft to date [33]. The first was the Airborne Laser Laboratory (ALL) which took place in the late 1970's and early 1980's which used a CO₂ laser with a wavelength of 10.6-μm. The second was the Airborne Laser (ABL) program which operated in the 2000's and used a COIL laser at 1.315-μm. Airborne optical systems like ALL and ABL have to deal with a phenomenon known as “aero-optics,” which refers to optical distortions caused by compressible aero-dynamic flow features that pass through the outgoing beam. These optical distortions were first noticed due to image degradation in wind tunnel measurements in the 1950's [61] as well as in photo-reconnaissance missions in the 1960's [35].

The peak on-target irradiance of a beam passing through an optical disturbance, I , divided by the diffraction-limited performance, I_0 , is known as the Strehl ratio [40], SR,

$$\text{SR} = \frac{I}{I_0}. \quad (1.1)$$

The diffraction-limited performance is the beam intensity that would exist on the same target if not for the optical disturbance. The Airborne Laser Laboratory had an estimated Strehl ratio of 95%[33] so that the “aero-optics problem” effectively did not apply for this case. Following the Airborne Laser Laboratory program there was a desire to move toward shorter wavelengths in order to take advantage of improved diffraction-limited performance, leading to a smaller-diameter focused spot on target with a higher irradiance I_0 : [31],

$$\frac{I_0}{P} = \frac{1}{\pi} \left(\frac{Ap}{\lambda z} \right)^2, \quad (1.2)$$

where P is the laser output power, Ap is the aperture size, and z is the propagation distance. The improvement in diffraction-limited performance as the laser wavelength is decreased is shown in Figure 1.1. By only changing the laser source from a 10-μm to 1-μm wavelength the diffraction-limited performance can be increased 100 times.

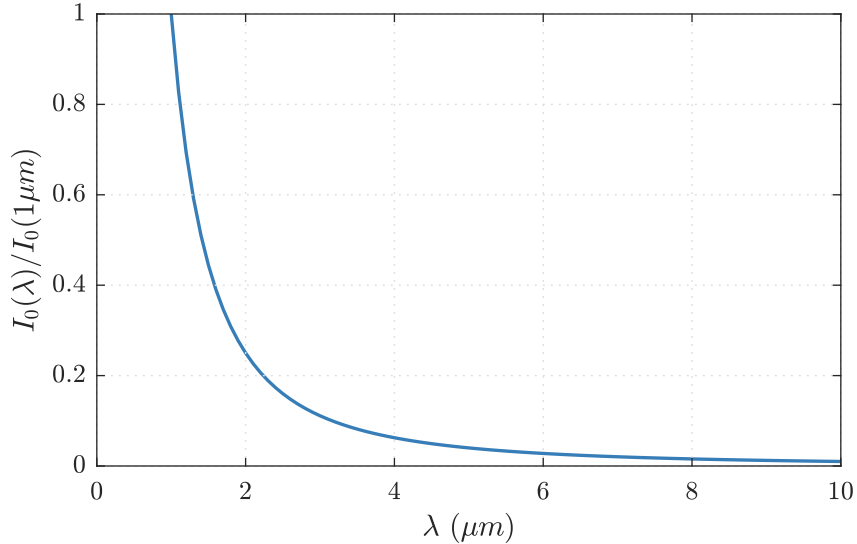


Figure 1.1. Diffraction-limited far-field intensity of a beam normalized by the performance at 1-μm.

Aero-optical issues start to become important as the wavelength is decreased as is evident from the Maréchal approximation [41] which relates the Strehl ratio to wavelength,

$$\text{SR} \approx \exp \left\{ - \left[\frac{2\pi \text{OPD}_{\text{RMS}}}{\lambda} \right]^2 \right\}, \quad (1.3)$$

where OPD_{RMS} is the spatial root-mean-square of the optical path difference over the aperture and is a way to quantify the optical disturbance as will be discussed further in Chapter 2. As stated above, the ALL had a Strehl ratio of 95%; however, if the ALL system's laser was swapped with another laser of a lower wavelength, the Strehl ratio would significantly decrease as shown by Figure 1.2. While going from 10 to 1-μm hypothetically results in a 100-fold increase in diffraction-limited performance, the actual on-target intensity that this hypothetical system obtains would be essentially zero due to the much larger effect that aero-optical aberrations have on the outgoing beam as the wavelength is reduced. This means that the aero-optical problem can no longer be ignored, which was recognized as one of the main developmental risks of the ABL program [16].

As the next generation of airborne directed-energy systems are developed some amount of ground testing of those systems will need to occur. In order to understand the aero-optical environment that these systems will experience in the air, wind tunnel tests will need to be employed. These tests are cheaper to perform than, for example, flight testing, and allow for quicker iteration of design

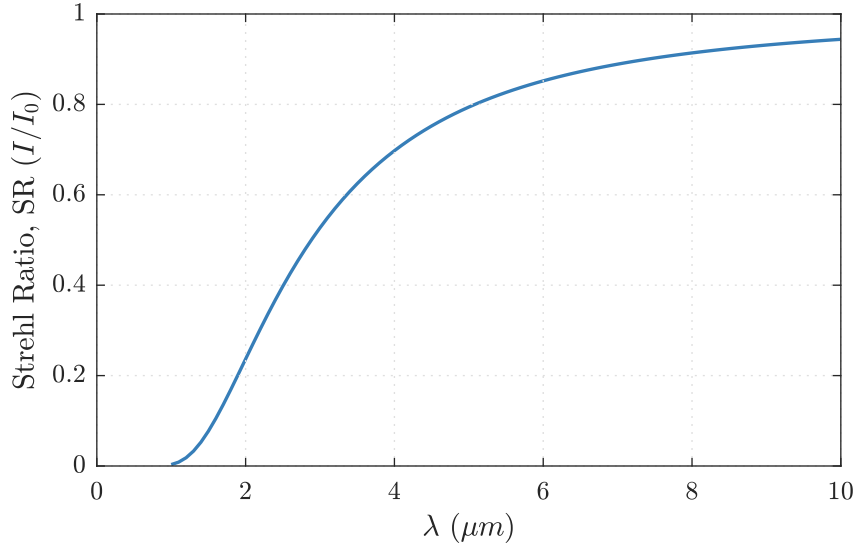


Figure 1.2. Strehl ratio due to the OPD_{RMS} of the Airborne Laser Laboratory (ALL) at various laser wavelengths. ALL had an estimated Strehl ratio of 95% with its 10.6- μm laser.

parameters. However, as will be described in further detail in Chapter 2, wind-tunnel measurements of aero-optical effects typically require passing a test beam into and through the test-section, so that the test beam is susceptible to acquiring additional optical contamination including but not limited to the boundary layer present on the wall and the acoustic environment generated by the wind tunnel fan [23]. Note that it is common in signal-processing terminology to use the word “noise” to describe unwanted interference that appears in addition to the “signal” that is the objective of the measurement; however, in this dissertation, the word “contamination” is used to describe any optical noise sources that are unrelated to the aero-optical signal, in order to avoid confusion with use of the word “noise” to describe acoustic noise which, as will be shown, is also a source of optical contamination.

Assuming that the optical disturbances from aero-optical effects are statistically independent from the contaminating optical disturbances from the testing environment, we can estimate the total optical disturbance as

$$OPD_{RMS,TOTAL}^2 = OPD_{RMS,MODEL}^2 + OPD_{RMS,ENVIRONMENT}^2. \quad (1.4)$$

As an example of the effect that optical contamination may have on system design, Figure 1.3 illustrates a hypothetical iterative design process, where the design objective is to obtain a design that

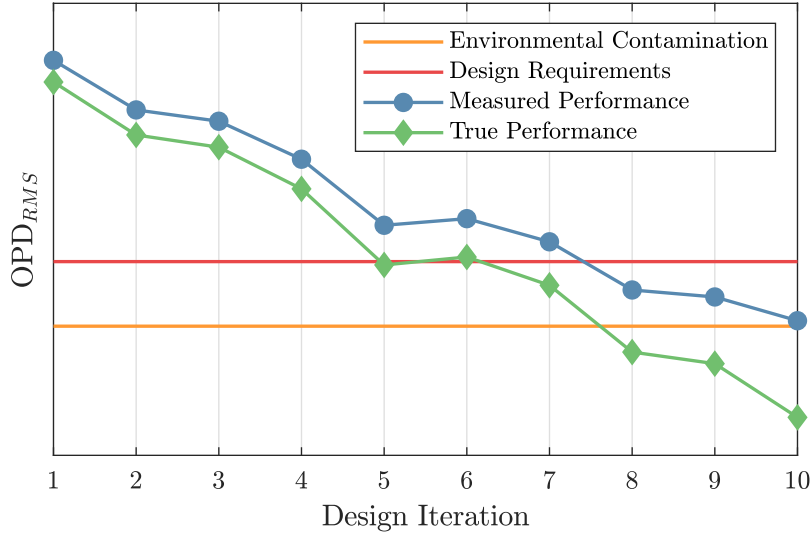


Figure 1.3. Hypothetical iterative design process of an airborne directed-energy system. The required performance level is shown by the red line and the testing environment's contamination is shown by the orange line.

meets a required level of performance shown in red, in the presence of a level of environmental optical contamination shown in orange. The design process was simulated by an initial aero-optical OPD_{RMS} shown on the left of the plot, and the improvement in system performance achieved with each design iteration was simulated as a nearly linear reduction in OPD_{RMS} combined with 15% random variation. If only the measured data, that is, including the effect of environmental contamination using Equation 1.4, is used to assess the system's performance then three additional design iterations are needed to achieve a usable design, which can add significantly to the development time and costs. If the environmental contamination is greater than the design requirement, the measured performance will never reach the required performance criteria. However, if the environmental contamination can be estimated, mitigated and/or removed, then the measured performance is a more accurate evaluation of the true aero-optical performance, and design convergence can be achieved more quickly and with more accurate results.

This dissertation will examine the environmental contamination of aero-optical measurements in wind tunnels, with a particular focus on the contamination due to acoustic noise within the wind tunnel. A review of the available literature and important concepts is given in Chapter 2. In Chapter 3, the optical disturbances caused by acoustic waves from simple plane and spherical waves are presented, leading to a process for estimating the acoustical environment within the test section of a wind tunnel. The strength of an spherical acoustic wave will be assessed with both microphone

and optical measurements. Multi-dimensional spectral techniques will be used to analyze optical wavefronts in Chapter 4 and to filter optical wavefronts in Chapter 6. These filtering techniques will contain some optical contamination particularly in regions where the various signal components interfere with one another. In order to further reduce the optical contamination, Chapter 7 will utilize additional sensor information from both microphones and accelerometers to remove some of the overlapping contamination to obtain a better picture of the actual optical performance of an airborne directed-energy system from ground test measurements. This document along with the source code is archived at <https://github.com/bcatronnd/Dissertation>.

CHAPTER 2

LITERATURE REVIEW

Strong narrow-band acoustic waves traveling upstream have been measured in-flight with optical wavefronts from a turret as part of the AAOL program [15]. This was one of the first indications that a temporally narrow-band acoustic signal related to a fan was a noise source that could contribute significantly to the overall signal. Additional measurements have shown both narrow-band and broad-band acoustic signals measured in-flight through a flat window with both boundary and shear layers present [22]. Broad-band acoustic signals have been reported previously in optical wavefront measurements during boundary layer measurements in wind-tunnels but the effect was only important at low temporal frequencies [23, 58]. Optical measurements have also been made looking specifically for the acoustic waves inside a wind-tunnel, by looking for narrow-band optical disturbances associated with the wind-tunnel fan, with various model support structures [10], or with acoustic duct modes, showing that the optical disturbances due to the acoustic environment not only travel upstream at $u - c$, but also downstream at $u + c$ and cross-stream at $\pm c$ [11].

The literature review will consist of primarily two sections. The first section will examine aero-optics while the second will look at acoustics inside of ducts.

2.1 Aero-Optics

In optically active flows the index-of-refraction, n , varies locally along with other fluid properties. Gladstone and Dale [20] found that the index-of-refraction is primarily a function of density with a loose dependence on the wavelength of light. Gladstone and Dale proposed a “specific refractive energy” now known as the Gladstone-Dale constant, K_{GD} ,

$$K_{GD} = \frac{n - 1}{\rho}. \quad (2.1)$$

For air the refractive index can be related to state quantities [62]

$$n - 1 = 77.6 \times 10^{-6} \frac{p}{T} \left(1 + \frac{7.53 \times 10^{-3}}{\lambda^2} \right), \quad (2.2)$$

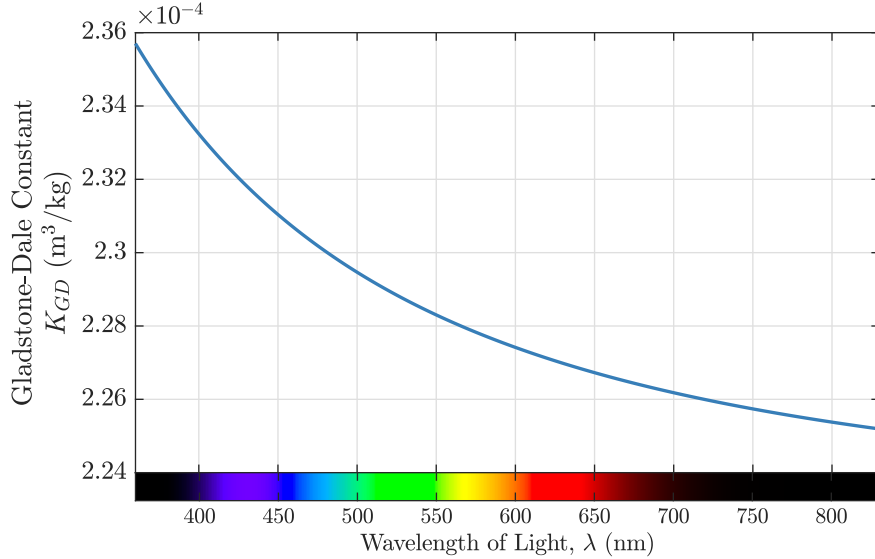


Figure 2.1. Gladstone-Dale constant for air over the visible wavelength range.

where p is in mbar, T is in K, and λ is in μm . By combining this relationship with the ideal gas law, the Gladstone-Dale constant can be determined as a function of light wavelength,

$$K_{GD} = 2.23 \times 10^{-4} \left(1 + \frac{7.53 \times 10^{-3}}{\lambda_{\mu\text{m}}^2} \right) \left[\frac{\text{m}^3}{\text{kg}} \right]. \quad (2.3)$$

The Gladstone-Dale constant for air over the visible range is shown in Figure 2.1. While the value for K_{GD} does vary over the visible range, it is only a few percent, and many sources use an average value of $2.27 \times 10^{-4} \text{ m}^3/\text{kg}$ for the visible and near-infrared [30]. The Gladstone-Dale relationship is typically presented as

$$n = 1 + K_{GD}\rho \quad (2.4)$$

but when applied to situations where there are significant fluctuations in the flow an alternate form is often more useful

$$n' = K_{GD}\rho' \quad (2.5)$$

where ' denotes the fluctuating component ($n' = n - \bar{n}$).

When a beam with an initially planar wave front passes through a region of optically active flow its wavefront becomes aberrated. The optical path length (OPL) at any point in the beam can be

obtained by integrating the index of refraction along the propagation of an optical ray [34].

$$\text{OPL}(x, y, t) = \int_{s_1}^{s_2} n(x, y, z, t) ds \quad (2.6)$$

The optical path difference (OPD), is then the spatially-averaged OPL over an aperture removed from the OPL.

$$\text{OPD}(x, y, t) = \text{OPL}(x, y, t) - \langle \text{OPL}(x, y, t) \rangle \quad (2.7)$$

When working with fluctuating components, the OPD can be calculated directly

$$\text{OPD}(x, y, t) = \int_{s_1}^{s_2} n'(x, y, z, t) ds. \quad (2.8)$$

As a finite beam of light travels normal to its wavefront it is diffracted, producing a theoretical limit on the performance of an optical system, i.e. diffraction-limited [5]. Sommerfeld defined diffraction as “any deviation of light rays from rectilinear paths which cannot be interpreted as reflection or refraction” [59]. Diffraction through an aperture can be approximated with the Huygens-Fresnel principle by assuming that every point within the aperture produces a spherical wavelet [27],

$$U(x_0, y_0) = \iint_{Ap} h(x_0, y_0; x_1, y_1) U(x_1, y_1) dx_1 dy_1, \quad (2.9)$$

where U is the complex amplitude, the subscripts 0 and 1 represent the coordinates of the observation plane and aperture plane respectively, and

$$h(x_0, y_0; x_1, y_1) = \frac{1}{j\lambda} \frac{\exp\{jkr_{01}\}}{r_{01}} \cos(\vec{n}, \vec{r}_{01}), \quad (2.10)$$

where $r_{01} = \sqrt{z^2 + (x_0 - x_1)^2 + (y_0 - y_1)^2}$, is the distance between any point in the observation and aperture planes. Equation 2.9 can be expanded to infinite limits of integration with the Kirchhoff boundary conditions where $U(x_1, y_1)$ is equal to zero outside of the aperture. The obliquity factor, $\cos(\vec{n}, \vec{r}_{01})$, can be approximated as being equal to one by assuming that the observation plane is at a much greater distance than the size of the aperture and is a small finite region. The accuracy of this assumption is with 5% if the angle between \vec{n} and \vec{r}_{01} does not exceed 18°[21]. With this assumption and for similar accuracy, r_{01} in the denominator of Equation 2.10 can be replaced with z , resulting in

$$h(x_0, y_0; x_1, y_1) \approx \frac{1}{j\lambda z} \exp\{jkr_{01}\}. \quad (2.11)$$

The Fresnel approximation replaces the spherical wavelets with a quadratic surface [17],

$$h(x_0, y_0; x_1, y_1) = \frac{\exp\{j k z\}}{j \lambda z} \exp \left\{ j \frac{k}{2z} [(x_0 - x_1)^2 + (y_0 - y_1)^2] \right\}, \quad (2.12)$$

which has a theoretical requirement that $z^3 \gg \frac{\pi}{4\lambda} \max\{[(x_0 - x_1)^2 + (y_0 - y_1)^2]^2\}$ due to the limited number of terms used in a binomial expansion of r_{01} . In practice this limit is not that critical [21]. By combining Equations 2.16 and 2.12, an expression for Fresnel diffraction can be obtained,

$$\begin{aligned} U(x_0, y_0) = & \frac{\exp\{j k z\}}{j \lambda z} \exp \left\{ j \frac{k}{2z} (x_0^2 + y_0^2) \right\} \iint_{-\infty}^{+\infty} \left[U(x_1, y_1) \exp \left\{ j \frac{k}{2z} (x_1^2 + y_1^2) \right\} \right] \\ & \exp \left\{ -j \frac{2\pi}{\lambda z} (x_0 x_1 + y_0 y_1) \right\} dx_1 dy_1. \end{aligned} \quad (2.13)$$

The function $U(x_0, y_0)$ may therefore be found from a two-dimensional Fourier transform:

$$U(x_0, y_0) = \text{FT}_2 \left[U(x_1, y_1) \exp \left\{ j \frac{k}{2z} (x_1^2 + y_1^2) \right\} \right] \quad (2.14)$$

where FT_2 is the two-dimensional Fourier transform and transform is evaluated at the spatial frequencies $\xi_x = x_0/\lambda z$, $\xi_y = y_0/\lambda z$.

The Fraunhofer approximation [21],

$$z \gg \frac{k \max[x_1^2 + y_1^2]}{2}, \quad (2.15)$$

places further restrictions than the Fresnel assumption approximation which results in $\exp \left\{ j \frac{k}{2z} (x_1^2 + y_1^2) \right\}$ being approximately unity over the aperture further simplifying Equation 2.13 to

$$\begin{aligned} U(x_0, y_0) = & \frac{\exp\{j k z\}}{j \lambda z} \exp \left\{ j \frac{k}{2z} (x_0^2 + y_0^2) \right\} \\ & \iint_{-\infty}^{+\infty} U(x_1, y_1) \exp \left\{ -j \frac{2\pi}{\lambda z} (x_0 x_1 + y_0 y_1) \right\} dx_1 dy_1. \end{aligned} \quad (2.16)$$

Equation 2.16 known as the Fraunhofer diffraction integral. In Fraunhofer diffraction, the function $U(x_0, y_0)$ maybe found from the Fourier transform of $U(x_1, y_1)$, when evaluated at the spatial frequencies $\xi_x = x_0/\lambda z$, $\xi_y = y_0/\lambda z$. For additional details on the derivation of Huygens, Fresnel, and Fraunhofer diffraction, including more in depth discussion on the assumptions and limits, see Goodman [21].

The optical path difference can be related to the complex amplitude by [12],

$$U(x_1, y_1) = \exp \left\{ j \frac{2\pi}{\lambda} \text{OPD}(x_1, y_1) \right\}. \quad (2.17)$$

Using the Fraunhofer diffraction integral, the nearfield OPD disturbance can therefore be used to calculate the farfield intensity profile ($I = UU^*$),

$$I(x_0, y_0) = \left| \text{FT}_2 \left(\exp \left\{ j \frac{2\pi}{\lambda} \text{OPD}(x_1, y_1) \right\} \right) \right|^2, \quad (2.18)$$

where the transform is evaluated at the spatial frequencies $\xi_x = x_0/\lambda z$, $\xi_y = y_0/\lambda z$ in the observation plane and the complex amplitude outside of the aperture is zero. For cases in which optical aberrations are nonexistent (i.e. $\text{OPD}(x, y, t) = 0$), the farfield irradiance pattern that results from Equation 2.16 is caused entirely by diffraction from the optical aperture, and is referred to as the “diffraction-limited” irradiance pattern. For a beam with a flat wave front and circular aperture, the farfield irradiance pattern is the Airy’s disk, and the peak irradiance at the center of the disk, I_0 , is the maximum irradiance that can be achieved by the optical system:

$$I_0 = \left(\frac{kAp^2}{8z} \right)^2 \quad (2.19)$$

where k is the wavenumber ($k = 2\pi/\lambda$), Ap is the aperture diameter, and z is the distance from the aperture to the observation plane. In the presence of aero-optical aberrations, $\text{OPD}(x, y, t)$ is non-zero, and the farfield irradiance pattern in this case tends to be more spread out and diffuse than the diffraction-limited case; furthermore, the beam may be shifted off target by optical tip/tilt imposed by the aberrations.

The Strehl ratio (SR), is the ratio of intensity on target (I) to the diffraction-limited on target intensity (I_0):

$$\text{SR} = \frac{I}{I_0} \quad (2.20)$$

The Strehl ratio can be computed accurately by applying Equation 2.16 twice, once for the diffraction-limited case to obtain I_0 , and a second time with the OPD field due to aero-optical aberrations included to obtain I . The farfield performance, can also be estimated via the Maréchal approximation:

$$\text{SR}(t) \equiv \frac{I(t)}{I_0} \approx \exp \left\{ - \left[\frac{2\pi \text{OPD}_{\text{RMS}}(t)}{\lambda} \right]^2 \right\} \quad (2.21)$$

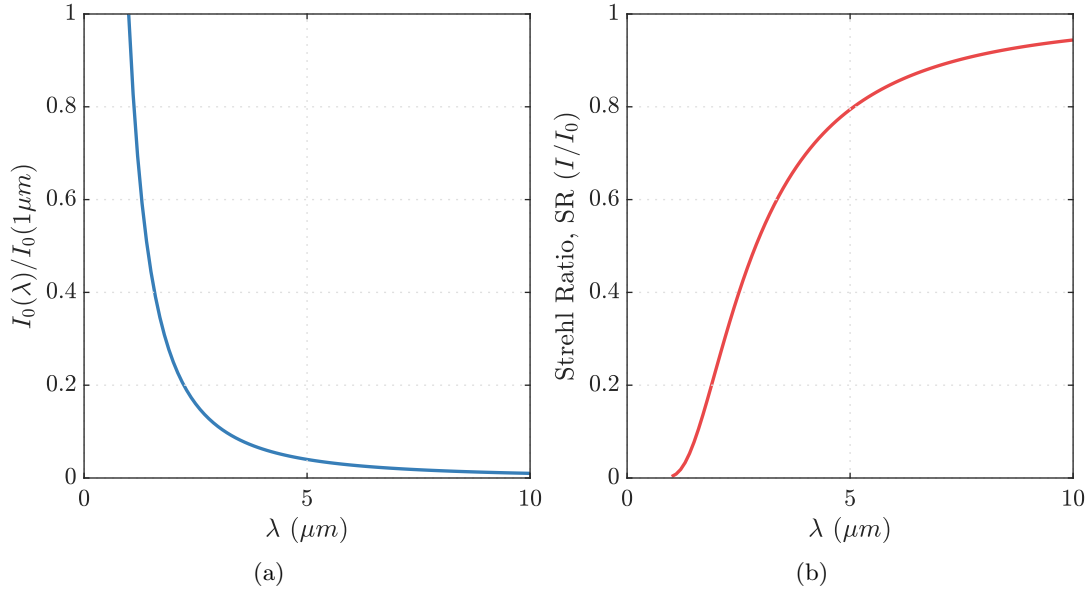


Figure 2.2. (a) Diffraction limited on target intensity as a function of wavelength normalized by the value at $\lambda = 1 \mu m$. (b) Strehl ratio as a function of wavelength for an aberration that gives SR = 0.95 at $\lambda = 10.6 \mu m$.

where OPD_{RMS} is the spatial rms of the wave front and λ is the wavelength of the beam. Equation 2.21 reveals a key relationship between OPD, wavelength, and the farfield performance, plotted in Figure 2.2b, and shows that, for the same aero-optical aberration, the Strehl ratio decreases substantially as system wavelength decreases. On the other hand, Equation 2.19 shows that the diffraction-limited farfield irradiance increases as the wavelength is shortened, plotted in Figure 2.2a. Together, Figure 2.2a and 2.2b show that as modern optical systems move to shorter wavelengths to increase I_0 , aero-optical aberrations cause a much more serious degradation of the Strehl ratio, illustrating why aero-optical considerations are critical in the development of new airborne optical systems. Figure 2.3 shows the OPD_{RMS} necessary to achieve various Strehl ratios over a range of wavelengths. As the wavelength of light decreases the required OPD_{RMS} decreases linearly for a fixed Strehl ratio.

2.1.1 Typical Optical Wavefront Measurement System

A diagram of a typical double-pass Shack-Hartmann wavefront front sensor setup is shown in Figure 2.4. The system starts with the laser in the bottom of the plot, which is then expanded to a larger diameter. The beam expander used in this research increased the diameter of the beam

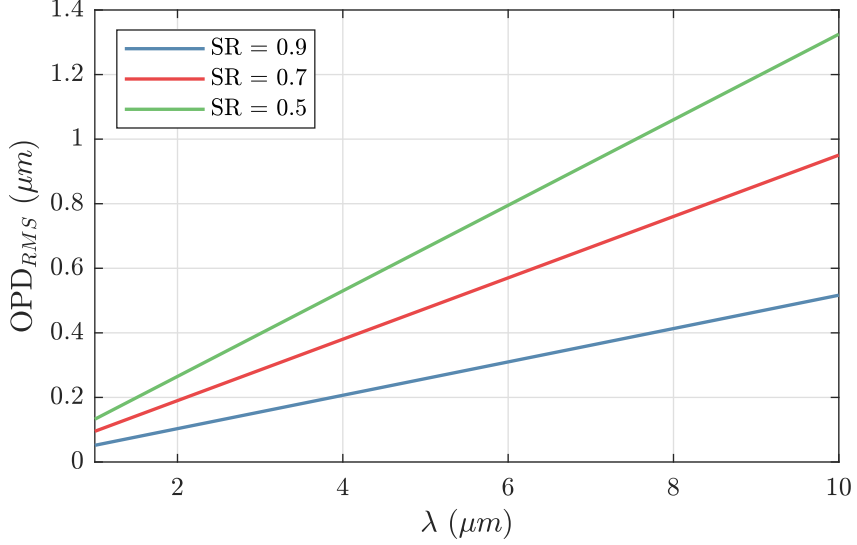


Figure 2.3. OPD_{RMS} values necessary to obtain Strehl ratios of 0.9, 0.7, and 0.5 over a range of wavelengths.

to approximately 1-inch. The larger diameter beam then passes through a beam splitter where half of the intensity is discarded and the other half proceeds to the primary telescope. The primary telescope expands the beam to the desired size for the first passage through the measurement region. For measurements made in a wind-tunnel, the beam angle, γ , is typically defined based on the flow direction [23] with 0° being looking straight into the flow and 180° looking downstream.

A large mirror is used to return the beam along the same path for a second passage through the measurement region where the primary telescope shrinks the beam back down to a 1-inch diameter. On the return path, the beam splitter sends half of the intensity back through the beam expander to the laser and half to the reimaging telescope. The reimaging telescope serves two purposes, the first is to create an image plane for the wavefront sensor at the desired object plane location, typically the return mirror for a double-pass setup. The second is to reduce the beam diameter for the wavefront sensor to a size that depends on the resolution and frame rate needed for a measurement.

The Shack-Hartmann wavefront sensor is comprised of a lenslet array and a camera [19]. A diagram of how the wavefront sensor functions can be seen in Figure 2.5. The perturbed wavefront is represented by the black lines on the top of the figure. Each lenslet produces a focused spot on the image plane with a location given by the average slope of the portion of the wavefront that passes through the lenslet. By measuring the displacement, [46], of the focal dot from its

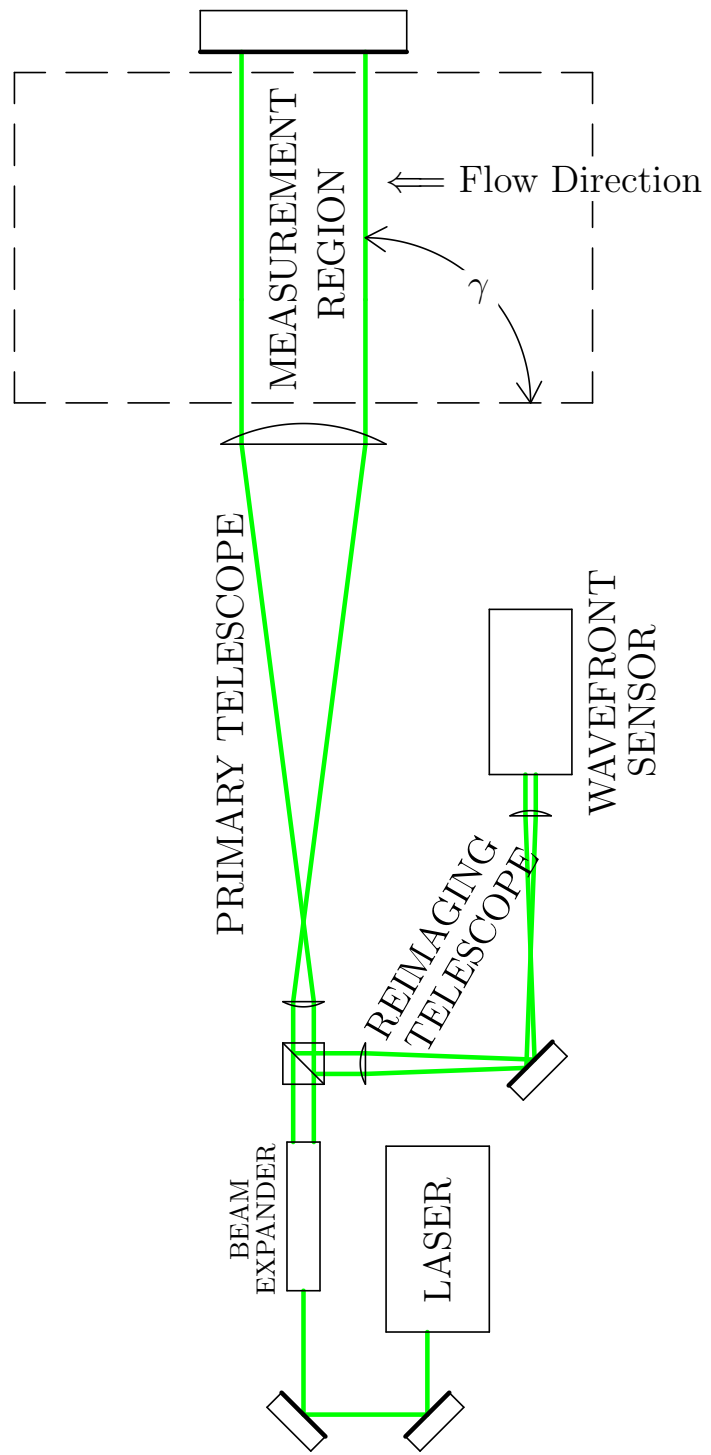


Figure 2.4. Typical double-pass optical wavefront measurement setup.

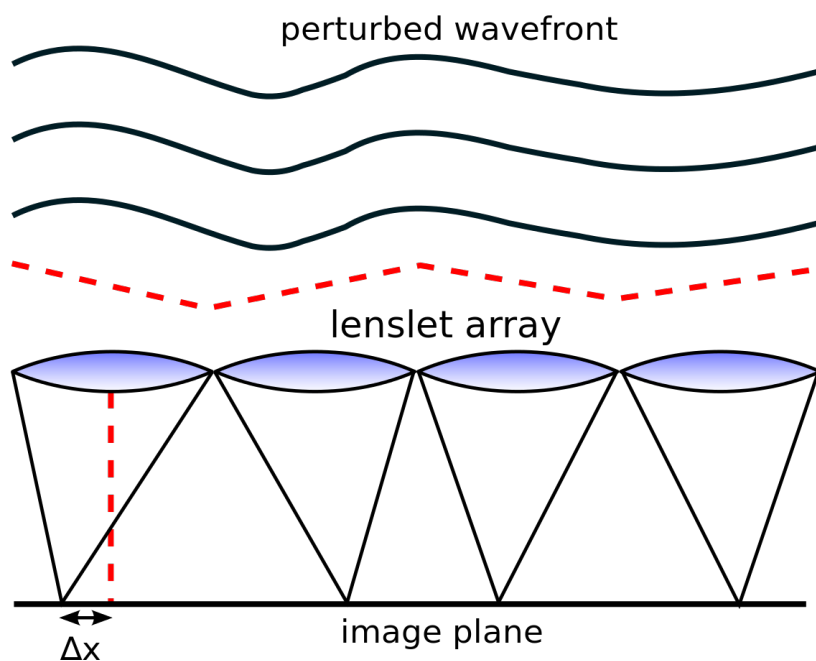


Figure 2.5. Diagram of a Shack-Hartmann wavefront sensor comprised of four lenslets. The black line represents the perturbed wavefront and the red line the mean slope over each lenslet. The focal point of the wavefront is shifted by Δx from the center-line of the lenslet based on the mean slope of the wavefront. [1]

normal position, the average slope, θ_x and θ_y , of the wavefront over a lenslet can be measured,

$$\theta_x = \tan^{-1} \frac{\Delta x}{f} \approx \frac{\Delta x}{f}, \quad (2.22)$$

where f is the focal length of the lenslet. With an array of gradient data, the optical path difference at each lenslet can be calculated using a number of integration methods [26], for example, one well-known method is the Southwell method [60].

2.1.2 Boundary Layer Optical Distortions

Because optical wavefront measurements within a wind tunnel will usually include the optical distortion from the boundary layer(s) on the wind-tunnel wall(s), it is important to have some familiarity. The time-averaged optical disturbance for a large aperture has been reported as,

$$\text{OPD}_{\text{RMS}} = B(\gamma) K_{GD} \rho_\infty M^2 \delta \sqrt{C_f} G(M), \quad (2.23)$$

where C_f is the skin-friction coefficient. The function $B(\gamma)$ accounts for angle between the beam and the direction of flow, γ :

$$B(\gamma) = \frac{0.19}{\sin(\gamma)}, \quad (2.24)$$

and

$$G(M) = 1 - 0.19M^2 + 0.03M^4. \quad (2.25)$$

Aperture size can be accounted for by Figure 2.6 (Figure 18 in Gordeyev [23]) with an approximation for the fit,

$$\frac{\text{OPD}_{\text{RMS}}(Ap)}{\text{OPD}_{\text{RMS}}} \approx 1 - a \exp \left\{ b \frac{Ap}{\delta} \right\} - (1 - a) \exp \left\{ c \frac{Ap}{\delta} \right\}, \quad (2.26)$$

where $a = 0.7795$, $b = -0.9616$, and $c = -0.1382$.

2.2 Duct Acoustics

This section will look at acoustics when confined to a duct in which the acoustic waves primarily travel in the direction of one axis and have walls confining the acoustics along the other two axes as is the case inside of a wind tunnel. Figure 2.7 shows the diagram used for deriving the acoustic properties inside of a constant area duct.

The derivation presented here is primarily influenced by Munjal [45] along with Jacobsen and

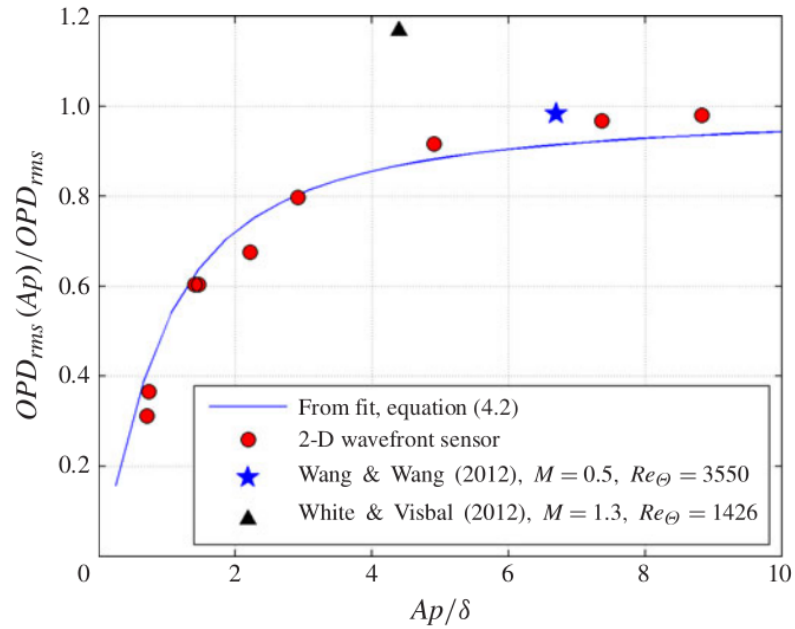


Figure 2.6. Aperture size correction for OPD_{RMS} (Figure 18 in Gordeyev [23]).

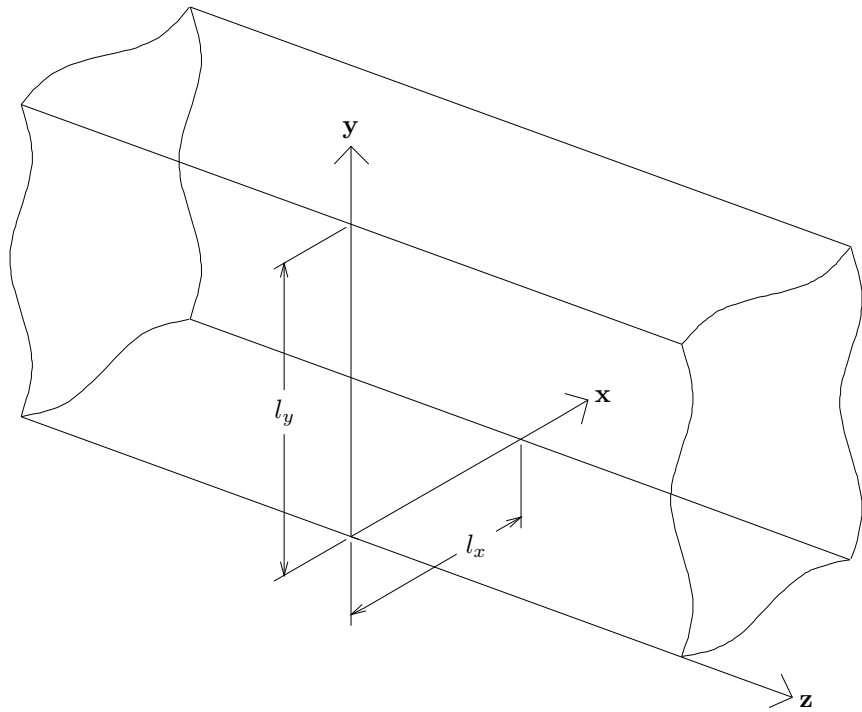


Figure 2.7. Duct with a rectangular cross-section.

Juhl [28]. The assumption used in this derivation is that the duct is of constant cross-section; methods used to solve for the acoustic field in a wind tunnel with varying flow cross sections are presented later in Section 3.3. This means that all mean quantities (ρ_0 , \mathbf{u}_0 , ...) are constant throughout space and time. Starting with the linearized inviscid forms of the conservation of mass,

$$\frac{\mathbf{D}\rho}{\mathbf{Dt}} + \rho_0 \nabla \cdot \mathbf{u} = 0, \quad (2.27)$$

and conservation of momentum,

$$\rho_0 \frac{\mathbf{D}\mathbf{u}}{\mathbf{Dt}} + \nabla p = 0. \quad (2.28)$$

The definition of the speed of sound ($\left. \frac{\partial p}{\partial \rho} \right|_s = c_0^2$) is then substituted into Equation 2.27,

$$\frac{1}{c_0^2} \frac{\mathbf{D}p}{\mathbf{Dt}} + \rho_0 \nabla \cdot \mathbf{u} = 0, \quad (2.29)$$

where c_0 is the speed of sound at average fluid properties (ρ_0, p_0, T_0, \dots). Next the difference between the material derivative (\mathbf{D}/\mathbf{Dt}) of Equation 2.29 and the partial derivative ($\partial/\partial\mathbf{x}$) of Equation 2.28 with respect to space is taken which results in the convected 3-D wave equation,

$$\left(\frac{\mathbf{D}^2}{\mathbf{Dt}^2} - c_0^2 \nabla^2 \right) p = 0. \quad (2.30)$$

Expanding the material derivative and dividing by c_0^2 ,

$$\left(\frac{1}{c_0^2} \frac{\partial^2}{\partial t^2} + \frac{2\mathbf{M}}{c_0} \frac{\partial^2}{\partial t \partial \mathbf{x}} - (1 - \mathbf{M}^2) \nabla^2 \right) p = 0, \quad (2.31)$$

where $\mathbf{M} = \mathbf{u}_0/c_0$. By using the fact that $c_0 = \omega/k_0$, Equation 2.30 can be written in a more convenient form,

$$\left(\frac{1}{\omega^2} \frac{\partial^2}{\partial t^2} + \frac{2\mathbf{M}}{\omega k_0} \frac{\partial^2}{\partial t \partial \mathbf{x}} - \frac{1 - \mathbf{M}^2}{k_0^2} \nabla^2 \right) p = 0, \quad (2.32)$$

where ω is the angular frequency and k_0 is the total wavenumber.

At this point the pressure field is written in complex form and assumed to be separable in both time and space such that $\hat{p}(\mathbf{x}, t) = \hat{p}(x, y)\hat{p}(z)\hat{p}(t)$. The temporal solution is assumed to take the form

$$\hat{p}(t) = \exp \{j\omega t\}, \quad (2.33)$$

which results in the spatial component of the convecting wave equation

$$\left((1 - \mathbf{M}^2) \nabla^2 - 2jk_0 \mathbf{M} \nabla + k_0^2 \right) \hat{p}(x, y) \hat{p}(z) = 0. \quad (2.34)$$

This can be further split into axial and cross-sectional components by splitting k_0 into components,

$$k_0 = \sqrt{k_{xy}^2 + k_z^2}, \quad (2.35)$$

and because the mean flow is only in the axial direction ($\mathbf{M} = M\hat{\mathbf{k}}$). The cross-sectional component is a typical Helmholtz equation

$$\left(\frac{\partial^2}{\partial x^2} + \frac{\partial^2}{\partial y^2} \right) \hat{p}_{xy}(x, y) + k_{xy}^2 \hat{p}(x, y) = 0, \quad (2.36)$$

whose solution,

$$\hat{p}(x, y) = \Psi_m(x, y), \quad (2.37)$$

is one of an infinite number of eigen-function solutions with discrete wavenumbers, k_m . The axial component of the convecting wave equation,

$$(1 - M^2) \frac{\partial^2 \hat{p}(z)}{\partial z^2} - 2jk_0 M \frac{\partial \hat{p}(z)}{\partial z} + k_z^2 \hat{p}(z) = 0, \quad (2.38)$$

retains the total wavenumber in the second term which means its solution will depend on the cross-sectional wavenumber value of the cross-sectional mode. The solution to the axial convecting wave equation,

$$\hat{p}(z) = C_m^+ \exp \{-jk_{zm}^+ z\} + C_m^- \exp \{+jk_{zm}^- z\}, \quad (2.39)$$

has waves traveling in both directions with the axial wavenumber in each direction for a given mode

$$k_{zm}^\pm = \frac{\mp M k_0 + \sqrt{k_0^2 - (1 - M^2) k_m^2}}{1 - M^2}. \quad (2.40)$$

The solution for a three-dimensional acoustic wave in a duct with a constant but arbitrary cross-section in complex pressure is the combination of the component solutions presented in Equations 2.33, 2.37, and 2.39,

$$\hat{p}(x, y, z, t) = \Psi_m(x, y) (C_m^+ \exp \{-jk_{zm}^+ z\} + C_m^- \exp \{+jk_{zm}^- z\}) \exp \{j\omega t\}. \quad (2.41)$$

The two solutions for a plane wave ($\Psi_m = 1$, $k_m = 0$) traveling in a duct have a characteristic speed of $u \pm c_0$. Acoustic modes will travel indefinitely if $k_0^2 - (1 - M^2)k_m^2 > 0$ (the quantity inside of the square-root of Equation 2.40). This presents a frequency at which a given mode will cut-on,

$$f_{cuton} = \frac{c_0}{2\pi} \sqrt{(1 - M^2)k_m^2}. \quad (2.42)$$

Below this frequency, an acoustic mode will be exponentially attenuated as it travels through the duct.

2.2.1 Characteristic Equations of Cross-Sections

In order to determine the characteristic equations of an acoustic field within a cross-section the solution to Equation 2.36 needs to be determined. In this research, it will be assumed that the walls of the duct are perfectly rigid, giving the following boundary condition for the 2-D Helmholtz equation:

$$\nabla p_{x,y}(x, y) \cdot \mathbf{n}_{wall} = 0 \quad (2.43)$$

This boundary condition results in the acoustic waves being perfectly reflected off of the duct walls. There are several known empirical solution sets of the characteristic equations for specific geometries with the rigid wall assumption.

The first of these solutions is for a duct with rectangular cross-section,

$$\Psi_{m,n}(x, y) = \cos(k_x x) \cos(k_y y), \quad (2.44)$$

where the wave numbers along each axis are $k_x = m\pi/l_x$ and $k_y = n\pi/l_y$. The duct has a width of l_x and a height of l_y . The total cross-sectional wave number for use in determining the axial wave numbers is

$$k_m^2 = k_x^2 + k_y^2. \quad (2.45)$$

Figure 2.8 shows the characteristic functions when $m=0:2$ and $n=0:3$ for a rectangular cross-section of width of l_x and height of l_y . The lines depicted in the figure are nodal lines and represent locations where there is zero pressure fluctuations for that acoustic mode.

The second set of known empirical solutions is for a circular cross-section with radius R ,

$$\Psi_{m,n}(r, \theta) = J_m(k_{mn}r) \exp \{ \pm jm\theta \}, \quad (2.46)$$

Characteristic Functions for a Rectangular Duct

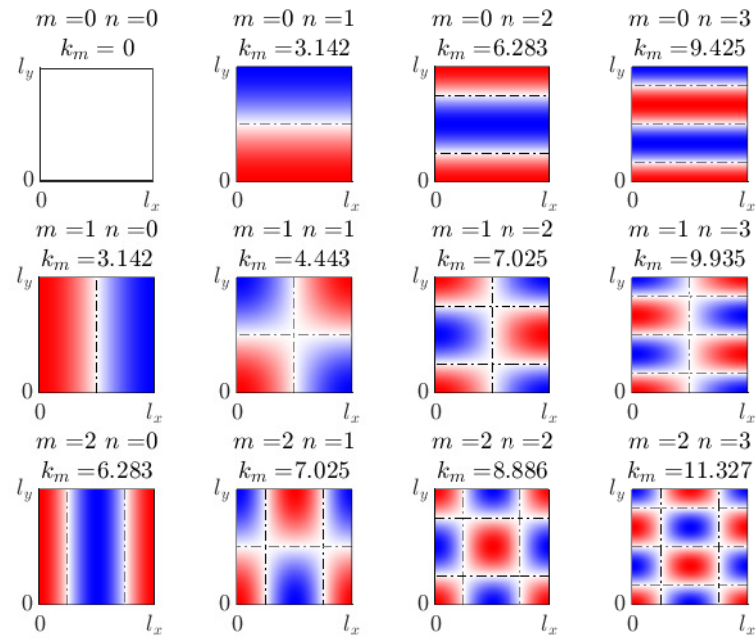


Figure 2.8. Characteristic solutions to Equation 2.36 with rigid wall in a rectangular cross-section where $m=0:2$ and $n=0:3$. Nodal lines are depicted by the dot-dash lines. The cross-sectional wave numbers, k_m , listed are for a duct of unit length and height.

Characteristic Functions for a Circular Duct

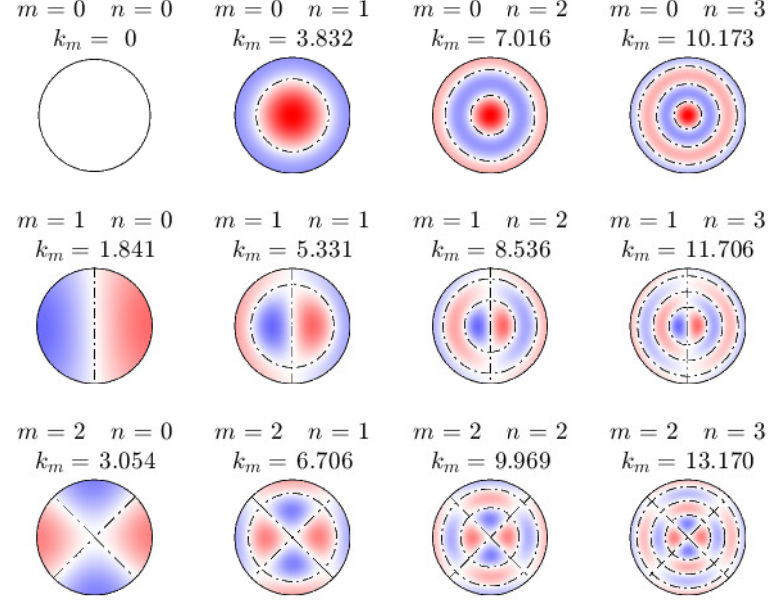


Figure 2.9. Characteristic solutions to Equation 2.36 with rigid wall in a circular cross-section where $m=0:2$ and $n=0:3$. Nodal lines are depicted by the dot-dash lines. The cross-sectional wave numbers, k_m , listed are for a duct of unit radius.

where J_m is the m^{th} Bessel function of the first kind and the \pm indicates the direction of spin. If the left and right spin coefficients are equal in magnitude then a non-spinning mode is created. In order to satisfy the solid wall boundary condition $J'_m(k_{mn}R) = 0$ which determines a set of discrete values for the cross-sectional wave number at the n^{th} zero for the m^{th} Bessel function. Figure 2.9 shows the characteristic functions for a circular duct.

CHAPTER 3

AERO-OPTICAL AND ACOUSTICAL COUPLING

Acoustic waves are isentropic compression waves with the fluctuating pressure, p' , determining the strength of the wave. This fluctuating pressure is related to the sound pressure level, SPL by

$$\text{SPL} = 20 \log_{10} \left(\frac{p_{RMS}}{p_0} \right) \quad (3.1)$$

where p_{RMS} is the root mean square of the pressure fluctuation, and p_0 is the reference pressure (20 μPa for air). The pressure fluctuations can be related to the density fluctuations via the definition of the speed of sound:

$$c_0^2 = \left(\frac{\partial p}{\partial \rho} \right)_s = \frac{p'}{\rho'} \quad (3.2)$$

where c_0 is the speed of sound at mean fluid properties and the subscript s denotes constant entropy. It can be shown by combining Equations 2.5 and 2.7 that the fluctuating density can be related to the OPD,

$$\text{OPD} = K_{GD} \int_{s_1}^{s_2} \rho' ds. \quad (3.3)$$

This can be combined with Equation 3.2,

$$\text{OPD} = \frac{K_{GD}}{c_0^2} \int_{s_1}^{s_2} p' ds, \quad (3.4)$$

to provide a way of computing the optical path difference of a sound pressure field.

3.1 Simulating an Optical Wavefront Measurement from an Acoustic Field Function

The following analysis is presented for the case of a measurement field subject to acoustic excitation at a discrete frequency. Parameter values at each point in the field oscillate at the frequency of the acoustic field, with a magnitude and phase relationship to the acoustic field that can be represented by complex notation and that depends on the physics of the interaction with the acoustic field.

The effect of a complex acoustic pressure field on an optical wavefront can be simulated by applying Equation 3.4. To accomplish this, two separate coordinate systems will need to be defined. The first is the beam coordinate system, \mathbf{x}_B , that will have a measurement aperture, which is typically circular, defined in the xy-plane and assuming the beam propagates in the z-direction. The second is the acoustic coordinate system, \mathbf{x}_A , that will be defined based on the source location or the geometry that the acoustic waves are propagating through. A function representing the transformation from one coordinate system to the other can be defined as

$$\mathbf{x}_A = R\mathbf{x}_B + T, \quad (3.5)$$

where R is a matrix which represents the rotation and T is a vector that represents the translation.

The important parameters for defining the aperture on which the beam coordinate system is based are the aperture size, Ap , and the spatial discretization which, if the beam is measured using a Shack-Hartmann wavefront sensor, is the number of lenslets or sub-apertures in the wavefront sensor, $N_{lenslets}$. Assuming that the aperture is either circular or square and the lenslet size and sub-aperture size is approximately $Ap/N_{lenslets}$, the x locations of the center of the sub-apertures go from $-Ap/2(1 - 1/N_{lenslets})$ to $Ap/2(1 - 1/N_{lenslets})$ by steps of $Ap/N_{lenslets}$ with the y locations having the same values. This gives a matrix representing both x_{Ap} and y_{Ap} that is $N_{lenslets}$ by $N_{lenslets}$. For the purpose of removing piston, tip, and tilt and creating a mask that represents the beam aperture, the radial coordinates, ρ_{Ap} and θ_{Ap} , of the aperture should also be calculated. A circular beam will have a mask defined by,

$$Mask_{Ap} = \begin{cases} 1, & \text{if } \rho_{Ap} \leq Ap/2 \\ 0, & \text{otherwise.} \end{cases} \quad (3.6)$$

The beam coordinate frame is the aperture coordinates extruded in the z-direction over the range of desired z-values.

After the beam coordinates are transformed into the acoustic coordinates using Equation 3.5, the complex pressure field, $\hat{p}(x, y, z, t)$ can be calculated at the points that are within the optical beam. If the pressure field is separable into spatial and temporal components, then the integration along the beam length only needs to be done once for each temporal frequency,

$$\widehat{\text{OPD}}(x, y) = \frac{K_{GD}}{c_0^2} \int_{z_1}^{z_2} \hat{p}(x, y, z)_{Ap} dz, \quad (3.7)$$

where $\widehat{\text{OPD}}(x, y)$ is the complex optical path difference as measured in the aperture plane. If a complex density field is known instead, than Equation 3.24 becomes

$$\widehat{\text{OPD}}(x, y) = K_{GD} \int_{z_1}^{z_2} \hat{\rho}(x, y, z)_{Ap} dz. \quad (3.8)$$

For the purposes of calculating time-averaged optical properties of simulated beam passing through a known complex pressure or density field a phase vector was defined, $\phi = [0, 2\pi)$. The measurable component as a function of phase is

$$\text{OPD}(x, y, \phi) = \text{REAL} \left[\widehat{\text{OPD}}(x, y) \exp\{-j\phi\} \right], \quad (3.9)$$

or as a function of time for all temporal frequencies,

$$\text{OPD}(x, y, t) = \text{REAL} \left[\sum \widehat{\text{OPD}}(x, y) \exp\{-j\omega t\} \right], \quad (3.10)$$

where there is a separate $\widehat{\text{OPD}}(x, y)$ computed for each temporal frequency. One of the more important parameters that can be calculated from OPD is the spatial RMS, OPD_{RMS} , which is calculated at each time or phase step at the points where the aperture mask equals one.

3.2 Simple Examples of Acoustic-Optical Coupling

Two basic acoustic pressure fields will be numerically examined for their optical properties. The first will be a planar acoustic wave that will be numerically simulated over a variety of conditions. The second will be a spherical acoustic wave that will be both numerically simulated and validated experimentally.

3.2.1 Planar Acoustic Waves

A planar wave is the simplest solution to the wave equation and varies only in time and the direction of travel. A planar wave can be calculated from the set of solutions for duct acoustics, Equation 2.41, given that $\Psi_m(x, y) = 1$,

$$\hat{p}(z, t) = C_m \exp \left\{ j(\omega t \mp k_{zm}^{\pm} z) \right\}. \quad (3.11)$$

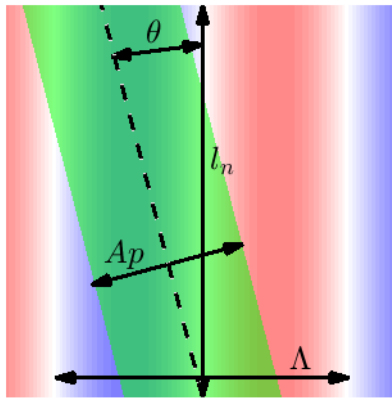


Figure 3.1. General geometry for various sample calculations for showing the acoustic-optical coupling effect.

This section will show the effect that acoustic waves have on the optical wavefront of a planar wave with the general geometry shown in Figure 3.1. For the following example, l_n is the width of the acoustic disturbance (for example, the width of the wind tunnel), θ is the angle between the planar acoustic wave and the beam direction, A_p is the aperture diameter of the beam, and Λ is the wavelength of the acoustic wave.

Figure 3.2 shows the time averaged OPD_{RMS} per meter of beam propagation when the beam path is parallel ($\theta = 0$) to the peaks and troughs of the planar acoustic wave as SPL is varied. As the sound pressure level increases the time averaged OPD_{RMS} also increases and can easily reach the point of being a significant factor in the measured optical disturbance. There is little difference between 0.1 and $1 \Lambda/A_p$, but as the wavelength gets much larger compared to the beam diameter, then the optical effect of the noise is greatly reduced, this effect is known as “aperture filtering.” Aperture filtering accounts for the fact that an aperture that is smaller than the wavelength of the optical disturbance only passes a portion of that optical disturbance, so that the measured OPD_{RMS} is reduced [57].

The effect of aperture filtering is more clearly shown in Figure 3.3. As the Λ/A_p ratio increases from 0.1, time-averaged OPD_{RMS} remains fairly constant until it starts to drop around Λ/A_p of 0.7 and starts to asymptotically approach zero which it basically reaches by Λ/A_p of 10. Figure 3.3 also shows the effect of changing the beam angle, θ , through the acoustic field. For nonzero θ , the beam encounters alternating high and low index of refraction as it passes through the test

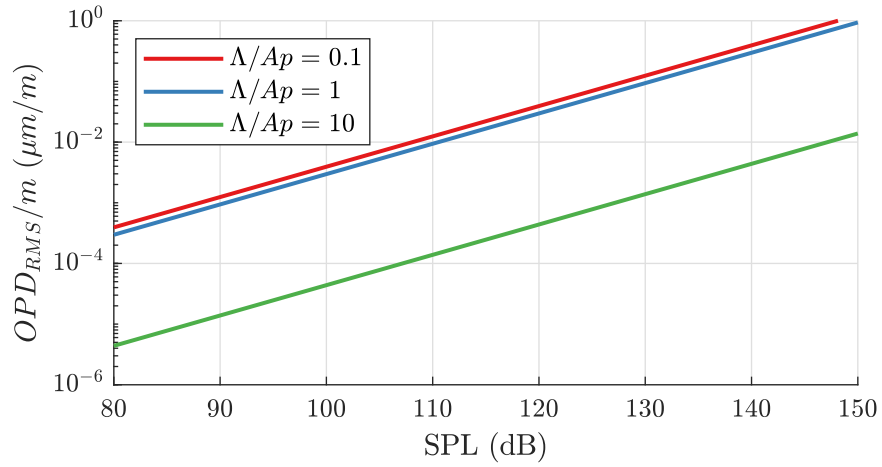


Figure 3.2. Theoretical time-averaged OPD_{RMS} per meter of beam propagation as a function of sound pressure level, SPL, for several Λ/Ap ratios and $\theta = 0$.

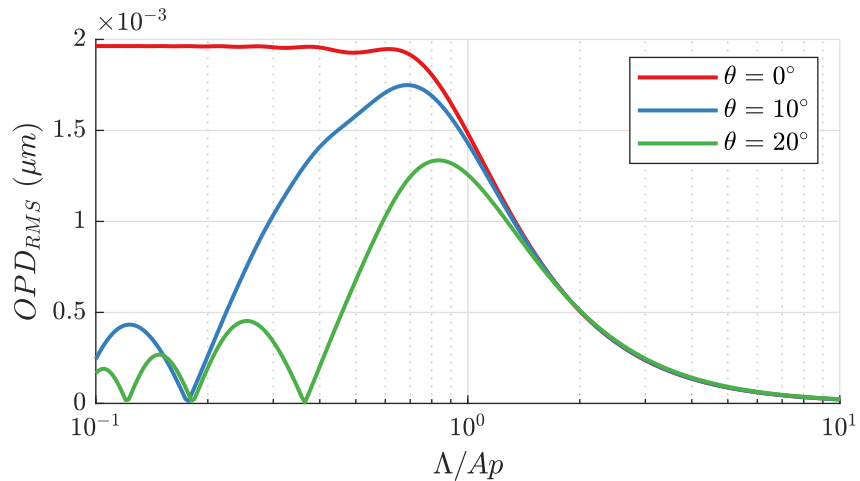


Figure 3.3. Theoretical time-averaged OPD_{RMS} for a RMS sound pressure of 1 Pa (SPL of 94 dB), l_n of 1 m, and various angles and Λ/Ap ratios.

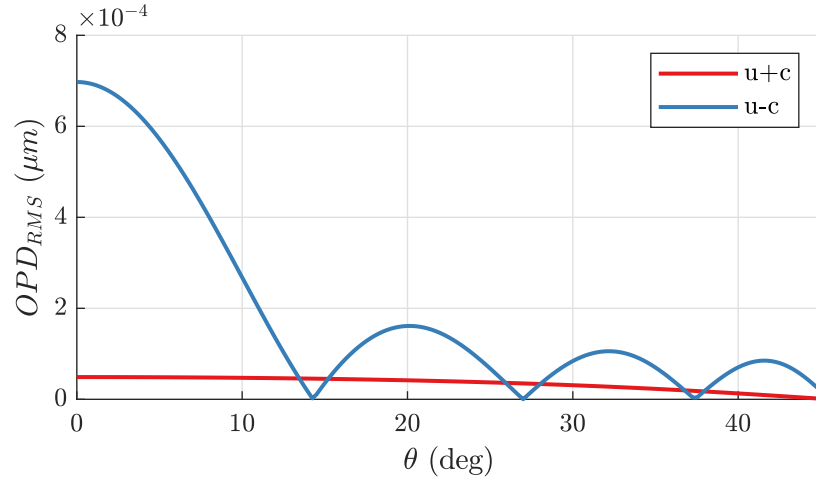


Figure 3.4. Theoretical time-averaged OPD_{RMS} for the two acoustic waves ($u+c$ and $u-c$) for the blade pass frequency (534 Hz) at Mach 0.6 with a RMS sound pressure of 1 Pa (SPL of 94 dB), l_n of 1 m, and Ap of 15 cm.

region, so that the time-averaged OPD_{RMS} begins to decrease compared to the $\theta = 0^\circ$ case below $\Lambda/Ap = 1$. There are also points of zero optical disturbance that occur at $\theta_{zero} = \tan^{-1}(n\Lambda/l_n)$ for $n \neq 0$; these points occur because the peaks and valleys of the optical disturbance caused by the sound wave effectively cancel out over the length of the integration path, $l_n/\cos\theta$.

Figures 3.2 and 3.3 show the optical effect of plane acoustic waves in a no-flow environment. The effect of wind-tunnel flow is to stretch (downstream-traveling waves) or compress (upstream-traveling waves) the wavelength of the acoustic noise thereby altering the filtering effect of the beam aperture. Figure 3.4 shows a typical optical disturbance from the two transverse acoustic waves ($u+c$ and $u-c$) present in a wind tunnel at Mach 0.6. Both waves have an RMS sound pressure of 1 Pa and the beam has an aperture of 15 cm and propagates through an acoustic field inside a duct of width, l_n , of 1 m. Over the vast majority of the look back angles the upstream-traveling acoustic wave has a much greater effect on the optical disturbance compared to the downstream-traveling acoustic wave, due to the much shorter wavelength of the upstream-traveling waves which is less affected by aperture filtering. However, the upstream-traveling wave goes through several zero points so that the downstream-traveling wave dominates at some beam angles.

3.2.2 Spherical Acoustic Waves

The acoustic field from a speaker may be assumed to be a spherical wave from a pulsating point if the frequency is sufficiently low and the measurement region is far enough away from the source

[52]. This pressure field when converted to complex pressure is represented by

$$\hat{p}(r, t) = \frac{A_0}{r} \exp \{-j(kr - \omega t)\}, \quad (3.12)$$

where A_0 is the fluctuating pressure strength and r is the distance from the source to the measurement point. The RMS pressure of this field can be represented by

$$p_{RMS} = \frac{|A_0|}{r\sqrt{2}}. \quad (3.13)$$

3.2.2.1 Theoretical OPD Calculations

A set of optical properties were calculated for a beam passing through a spherical acoustic field as defined by a point source using the process described previously in Section 3.1 and shown in Figure 3.5. These calculations used a circular aperture size of 0.25 m in diameter that was assumed to be measured using a Shack-Hartmann WFS with 32x32 sub-apertures with a non-dimensional acoustic wavelength, Λ , of $Ap/4$ to $10Ap$. The normal vector from the point source to the axis of the measurement beam defined the coordinate system. This normal distance, R , was a minimum $5Ap$ and a maximum of $25Ap$, keeping the measurement beam away from the singularity at the origin of the acoustic source. The OPD for the beam was integrated over a distance of ± 5 -m from the plane of the point source. To calculate the time-averaged OPD_{RMS} the phase of the source was varied from 0 to 2π with 25 total steps.

The result of these OPD_{RMS} calculations is shown in Figure 3.6. The top plots shows the expected optical disturbance ratio, $OPD_{RMS} / |A_0|$, for a perfectly spherical acoustic field measured over the beam length. The oscillations in the solutions for different R/Ap are caused by end effects in the integration. Because speakers often have a directivity in their emission, the oscillations can be greatly reduced by using a windowing function in the z-direction, such as a Hanning or Tukey window, the roughly model this directivity as shown in the bottom plot. While this plot was calculated with a single aperture diameter, the general trend holds for all other aperture diameters that were tested, the only effect was the size and width of the oscillations.

The peak of the optical disturbance ratio, $OPD_{RMS} / |A_0|$, is located at $\Lambda/Ap \approx 0.75$ for a circular aperture. The signal is reduced above this value due to aperture filtering and below this value because the shorter wavelengths have a reduced distance before alternating high and low index-of-refraction regions reduce the optical path difference. When the acoustic source point is sufficiently far enough away from the measurement beam, $R/Ap \geq 2$, the optical disturbance ratio,

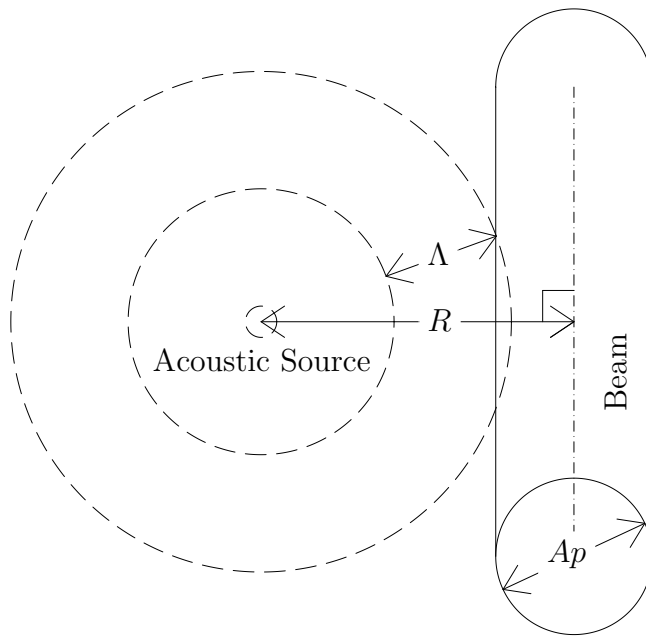


Figure 3.5. Diagram of the geometry used in the spherical wave simulation.

$\text{OPD}_{\text{RMS}} / |A_0|$ when multiplied by $\sqrt{R/Ap}$, can be collapsed onto a single curve for a range of Λ/Ap of 0.1 to 10. Above $\Lambda/Ap = 10$ the curves start to diverge away from one another. An approximate function fit to these data is

$$\frac{\text{OPD}_{\text{RMS}} \sqrt{R/Ap}}{|A_0|} \approx \frac{p_1(\Lambda/Ap)^3 + p_2(\Lambda/Ap)^2 + p_3(\Lambda/Ap) + p_4}{(\Lambda/Ap)^3 + q_1(\Lambda/Ap)^2 + q_2(\Lambda/Ap) + q_3} \quad (3.14)$$

with coefficient values shown Table 3.1. This functional fit has a coefficient of determination, R^2 , value of 0.9991.

3.2.2.2 Measurement of a Spherical Acoustic Wave with an Optical Beam

A small bench top experiment was used to compare the simultaneous optical and microphone measurements of an acoustic field from a speaker as shown in Figure 3.7. The distance from the center of the beam to the speaker was 102 mm with a beam diameter of 28 mm. An ACO model 7016B microphone [13] was placed directly over the speaker at a distance of 158 mm and was used with a Brüel & Kjær model 2670 preamplifier [7]. The speaker used was a Peerless model XT25SC90-04 [50] which has a fairly flat on-axis response from 1 kHz to 40 kHz.

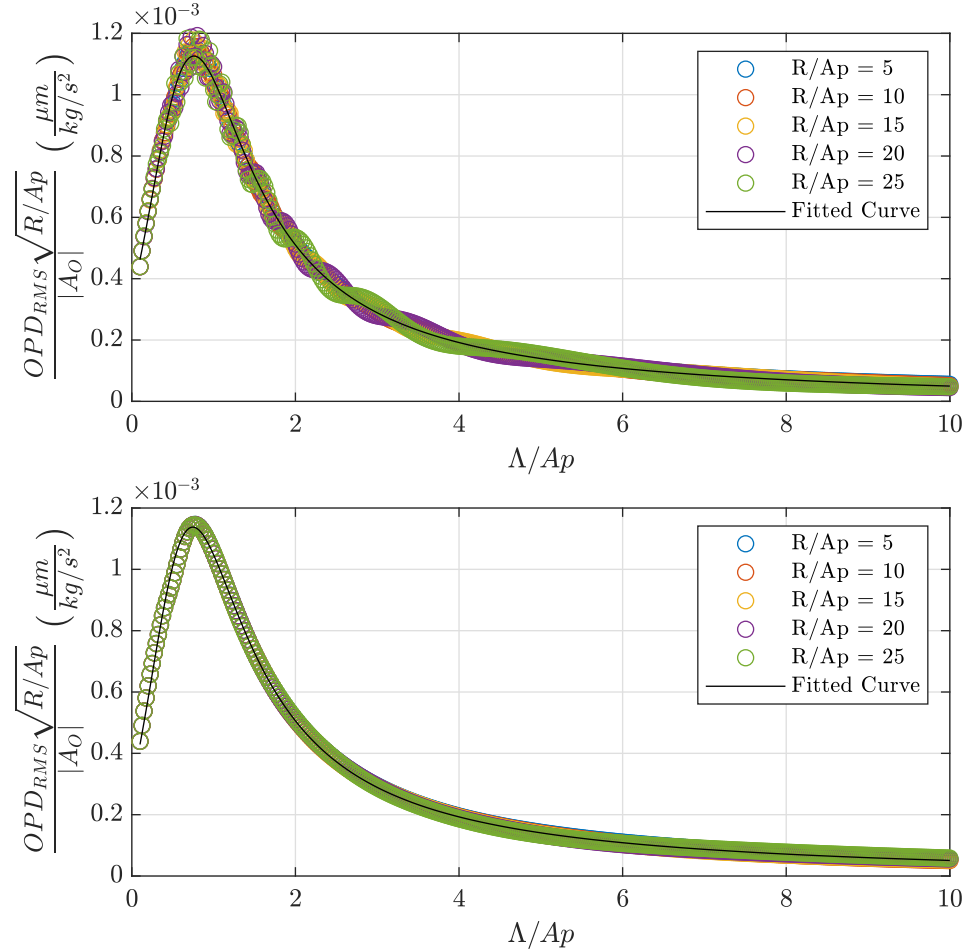


Figure 3.6. Theoretical time-averaged OPD_{RMS} for a spherical acoustic wave. The top plot shows a perfect spherical acoustic signal integrated over ± 5 m. The bottom plot shows has a Tukey window applied along the beam length to partially emulate source directivity which significantly reduces the measured oscillations.

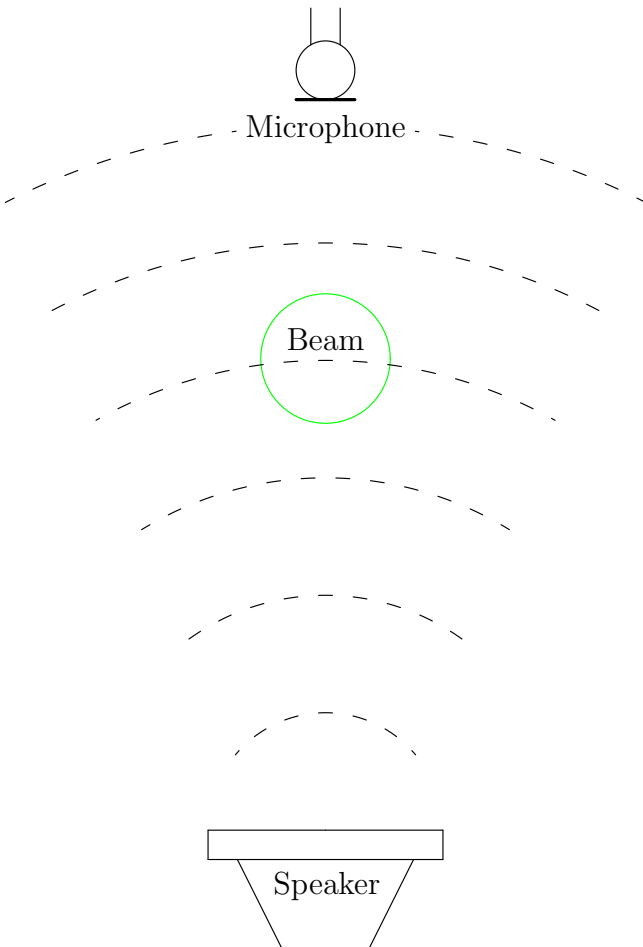


Figure 3.7. Spherical acoustic wave measurement test.

TABLE 3.1
CURVE FIT VALUES FOR FIGURE 3.6 AND EQUATION 3.14

Coefficient	Value
p_1	-1.845e-05
p_2	4.769e-04
p_3	4.520e-03
p_4	1.435e-03
q_1	5.399e+00
q_2	-5.145e+00
q_3	4.869e+00

The wavefront measurements system utilized in these measurements is similar to that shown in Figure 2.4 except there was no primary telescope. The speaker was located in the center of the measurement region which was about 2 feet in length and the re-imaging telescope reduced the beam diameter by a factor of two and re-imaged the return mirror. Optical wavefronts and microphone measurements were taken at 49 kHz. The speaker was sinusoidally excited at three different frequencies (9, 14, and 18 kHz) at a variety of voltages.

The absolute value of the fluctuating pressure strength, $|A_0|$, was calculated two different ways. First, the power spectrum of the microphone data was used to calculate the average p_{RMS} at the excitation frequency and the fluctuating pressure strength using Equation 3.13. For the second method, the optical wavefront was band-pass filtered at the excitation frequency using a process that will be discussed in Chapter 6. The time averaged OPD_{RMS} of the filtered wavefront data was then used to calculate the fluctuating pressure strength using Equation 3.14.

The results of these measurements of the fluctuating pressure strength is shown in Table 3.2. The differences between the two techniques for measuring the fluctuating pressure strength fell into two groups. For the 9 kHz cases, the differences ranged from 20-26% while for the higher frequency cases the differences were between 1.1-1.5%. In all cases the wavefront measurement reported a higher fluctuating pressure strength. With the exception of the highest excitation case at 9 kHz, the differences between the two techniques was fairly constant for each frequency group. Some of these differences maybe attributable to the frequency response of the microphone.

TABLE 3.2

COMPARISON OF MICROPHONE AND WAVEFRONT COMPUTATION OF $|A_0|$

$f_{speaker}$ (Hz)	$V_{speaker}$ (mV)	p_{RMS} (Pa)	OPD_{RMS} (μm)	$ A_0 _{mic}$ (kg/s^2)	$ A_0 _{wf}$ (kg/s^2)	Diff (%)
9000	100	5.65	6.545e-04	1.26	1.55	20.38
9000	250	12.23	1.421e-03	2.73	3.36	20.56
9000	500	19.52	2.386e-03	4.36	5.64	25.62
14000	1250	5.20	6.831e-04	1.16	1.18	1.24
14000	250	9.33	1.230e-03	2.09	2.12	1.50
14000	375	9.68	1.272e-03	2.16	2.19	1.16
18000	125	3.73	4.987e-04	0.83	0.84	1.10

In Figure 3.8, measured wavefronts are compared to the wavefronts simulated using the method described in Section 3.1 for the highest excitation cases at each frequency. The 9 kHz case shows some anomalies on the measured wavefront on the right side, and deviates from a spherical wave significantly, likely contributing to the significantly higher estimated pulsating field strength value when compared to the microphone estimate in Table 3.2. The 14 and 18 kHz cases show some remarkable agreement between the measured and simulated images. Optical wavefront measurements can therefore be used for making non-intrusive acoustic field measurements especially when the acoustic field is simple.

3.3 Estimating the Acoustic Field Inside a Wind-Tunnel Test-Section

Several mode-matching methods have been previously employed to solve the acoustic field in ducts, ranging from methods designed to solve axially-segmented turbofan duct liners [42] to muffler modeling [29]. These methods require the entire field to be solved simultaneously because there are duct modes traveling in both directions at each axial-spatial location. Using the turbofan duct liner version, a single azimuthal order, m , and only a few radial orders, n , need to be computed for the various boundary conditions with a constant mesh used through all the segments. In the muffler model version, step changes in the cross-section are employed, allowing for a constant mesh to be generated to account for all possible cross-sections.

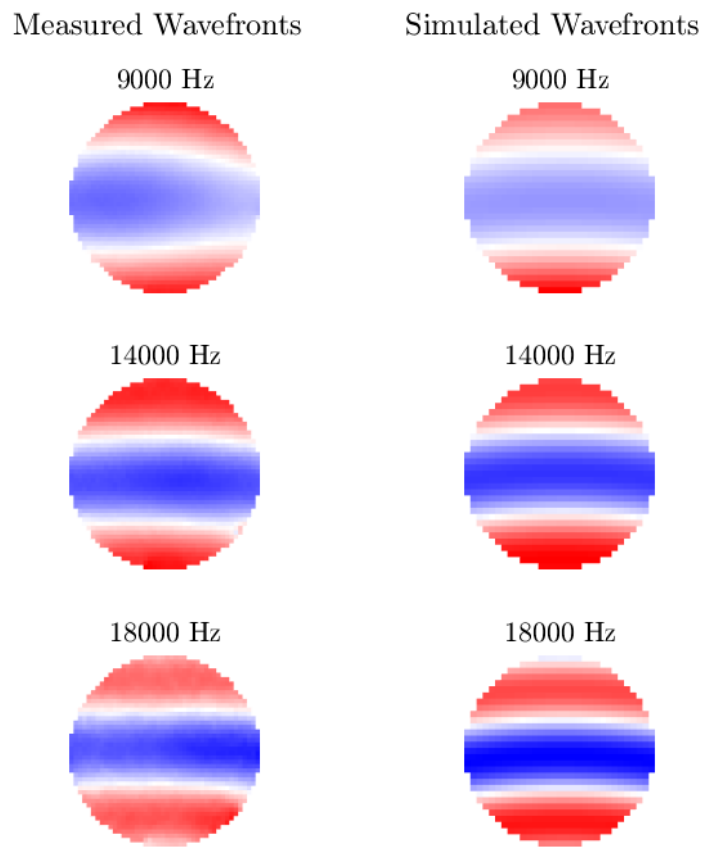


Figure 3.8. Comparison of measured wavefront to simulated ones for the highest-amplitude speaker excitation at each frequency.

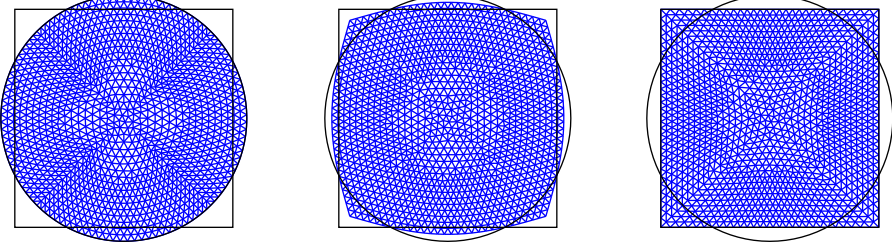


Figure 3.9. Deformable mesh for calculating the acoustic modes in the circular to square transitions at three stages.

For a wind-tunnel that has numerous cross-sectional area changes, specifically, a square cross-section for the test-section and a circular cross-section for the fan, the mode-matching method can become computational expensive. At each axial-location, all possible duct modes need to be calculated up to at the very least the cutoff mode k_m , if not higher [18], to fully resolve local duct modes. As such, in order to reduce the computational cost of simulating the acoustic environment inside of a wind tunnel, a mode marching method was employed instead of a mode-matching method, where an initial cross-sectional pressure field was marched from the wind-tunnel fan in both directions around the wind-tunnel and through the test-section. Although the mode-marching method is computationally simpler than the mode-matching method, there are also arguments for using the mode-marching method that are justified by the expected acoustic behavior in typical wind-tunnel circuits. Specifically, since the wind-tunnel test section normally has the smallest cross-sectional dimensions, higher-order acoustic modes tend to be reflected away from the test section; hence using a mode-marching method that does not rigorously account for reflections or all high-order modes should not add significant inaccuracy to the predicted results.

For the circular to square transition on either side of the wind-tunnel fan, a deformable mesh was used such that there would be a one-to-one mapping of mesh points throughout the transition. An example of the deformable mesh is shown in Figure 3.9 at both the square and circular limits and halfway in between. Because cross-sectional wavenumber scales with the area ($k_m^2 A = \text{const}$), all modes were solved for a cross-section of unit area. For the simulation of the Notre Dame White Field wind tunnel (described below) modes in the square cross-sections of the wind tunnel were calculated with both the deformable mesh and a rectangular mesh in order to allow for easy transitions in the cruciform region of this wind-tunnel's diffuser.

3.3.1 Mode-Marching Method Procedure

1. Starting Acoustic Pressure Disturbance

The method starts with an initial acoustic pressure disturbance that could be either measured, computed, or assumed.

$$\hat{p}^0(x, y) \quad (3.15)$$

For wind tunnels, the acoustic disturbance is generated by the main fan; hence \hat{p}^0 is the rotating radial fan modes associated with the rotating fan blades [14].

2. Modal Best Fit

The pressure disturbance at the current axial location is best fit to the possible modes.

$$\hat{p}^i(x, y) = \Psi_m^i(x, y) \cdot C_m^i \quad (3.16)$$

where Ψ_m^i are the possible modes for the local duct shape.

3. Transmitted Pressure Ratio

The pressure attenuation due to Mach number change [51] as a ratio of transmitted pressure to incident pressure is computed for an acoustic wave traveling with subsonic flow,

$$\frac{p_t}{p_i} = \left(\frac{1 + M_n}{1 + M_{n+1}} \right) \left(\frac{2M_{n+1}}{M_n + M_{n+1}} \right) \left(\frac{X_{n,n}}{X_{n,n+1}} \right) \left(\frac{X_{n,n}}{X_{n+1,n+1}} \right)^{1/(\gamma-1)}, \quad (3.17)$$

or traveling against subsonic flow,

$$\frac{p_t}{p_i} = \left(\frac{1 - M_n}{1 - M_{n+1}} \right) \left(\frac{2M_{n+1}}{M_n + M_{n+1}} \right) \left(\frac{X_{n,n}}{X_{n,n+1}} \right) \left(\frac{X_{n,n}}{X_{n+1,n+1}} \right)^{1/(\gamma-1)}, \quad (3.18)$$

where

$$X_{a,b} = 1 + \frac{\gamma - 1}{2} M_a M_b. \quad (3.19)$$

4. Reflected Pressure Ratio

The reflected pressure ratio is a useful quantity to keeping track of, because one of the main assumptions of the mode marching method is that the reflections are negligible. The pressure attenuation due to Mach number change [51] as a ratio of reflected pressure to incident pressure is computed for an acoustic wave traveling with subsonic flow,

$$\frac{p_r}{p_i} = \left(\frac{1 + M_n}{1 - M_n} \right) \left(\frac{M_{n+1} - M_n}{M_{n+1} + M_n} \right) \frac{Y_{n,n+1}}{X_{m,n+1}}, \quad (3.20)$$

or traveling against subsonic flow,

$$\frac{p_r}{p_i} = \left(\frac{1 - M_n}{1 + M_n} \right) \left(\frac{M_{n+1} - M_n}{M_{n+1} + M_n} \right) \frac{Y_{n,n+1}}{X_{m,n+1}}, \quad (3.21)$$

where

$$Y_{a,b} = 1 - \frac{\gamma - 1}{2} M_a M_b. \quad (3.22)$$

5. March Modes Forward

March the acoustic modes forward to the next axial location.

$$\hat{p}_{i+1}(x, y) = \frac{p_t}{p_i} \sum \Psi_m^i(x, y) \cdot C_m^i \cdot \exp\{\mp j k_{zm}^\pm z\} \quad (3.23)$$

6. Repeat

Repeat steps 2-5 until the desired location is reached (i.e. the wind-tunnel test section). Different starting pressure disturbances can also be checked.

3.3.2 University of Notre Dame White Field Wind-Tunnel Simulation

The University of Notre Dame White Field wind-tunnel is capable of reaching speeds of Mach 0.6 in the 3 foot by 3 foot test-section. A CAD model of the wind-tunnel is shown in Figure 3.10. The cross-sectional area and distance from the wind-tunnel fan going upstream are presented in Table 3.3 along with some comments on the segments between some of the cross-sections. For the distances in Table 3.3 the corners have been straightened out and set to a length equal to the center-line arc from the entrance to the exit of that segment. The transition segments on either side of the wind-tunnel fan convert the circular cross-section to a square cross-section. Between cross-section 6 and 7 the diffuser has a cruciform splitting it into four separate segments in which the duct modes were independently marched. The test-section is 2.75 m long and the main contraction shape from section 8 to 9 follows a fifth-order polynomial. Acoustic reflections that would be due to turning vanes or other internal structures have been neglected along with the fan hub and motor shaft geometry.

The wind-tunnel was discretized into smaller segments that were a maximum of 0.25 m in length. The speed throughout the wind-tunnel was determined via isentropic relations and the pressure transmission ratios were computed using Equations 3.17 and 3.18. Pressure reflection ratios were calculated using Equations 3.20 and 3.21 and verified to be small. Figure 3.11 shows these parameters for the tunnel at a Mach number of 0.6 in the test-section with flow going from right-to-left. For most of the wind-tunnel the Mach number is around 0.1 with the transmission pressure ratio (solid lines) at effectively unity. In the regions of rapid Mach number change around the contraction and the test-section diffuser, the transmission pressure ratio can deviated significantly from unity, especially for sound waves traveling upstream. These regions also show some reflected pressure ratios (dotted lines) that are non-negligible. For acoustic waves traveling in both directions, the section on the opposite side of the test section produces some reflected acoustic waves back into the test section.

The wind-tunnel fan was modeled using a circular duct mode of $m = 8$ and $n = 0$ at a frequency of 520 Hz which corresponds to the blade-passing frequency of the Mach number 0.6 case. The duct mode of $m = 8$ and $n = 0$ is the largest cut-on mode in which the azimuthal mode number is a whole-number fraction of the total number of fan blades, 32. The peak-to-peak acoustic pressure of the fan was set to unity to allow the results to be easily scaled. To check for the possibility of

TABLE 3.3
WIND-TUNNEL CROSS-SECTION SPECIFICATIONS

Section	Area (m^2)	Z (m)	Comment
1	5.07	0.00	
2	4.68	2.42	
3	4.68	4.56	
4	3.57	8.65	
5	3.57	10.71	
6	1.97	14.33	Cruciform
7	0.84	17.99	Test-Section
8	0.84	20.73	Sixth Order Contraction
9	5.44	23.07	
10	5.44	24.30	
11	5.44	26.54	
12	8.04	29.65	
13	8.04	31.88	Circle to Square Transition
14	4.67	39.25	

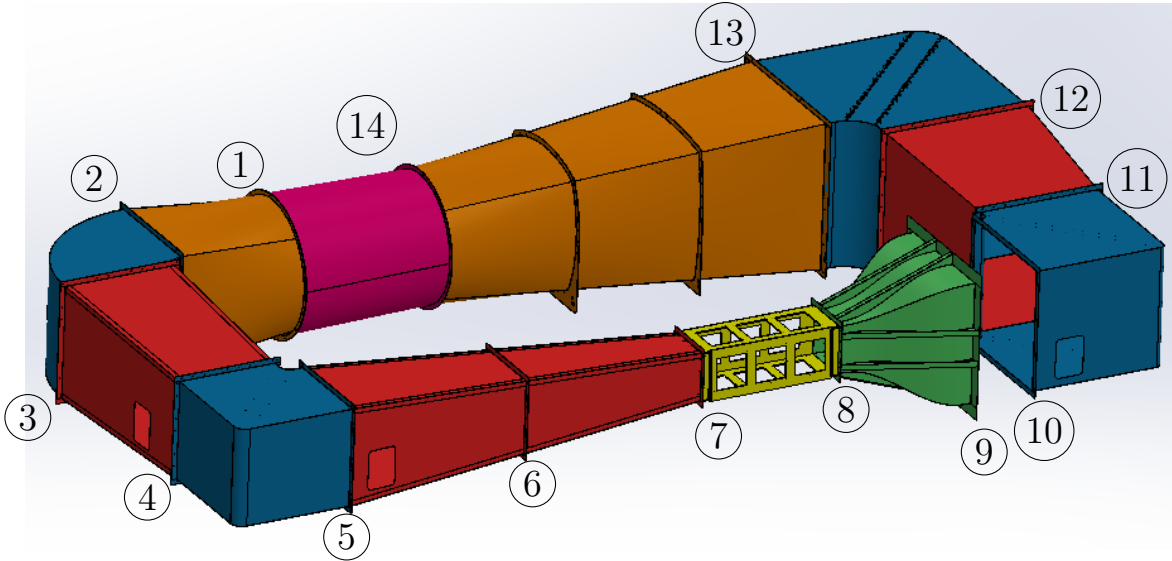


Figure 3.10. CAD model of the University of Notre Dame Whitefield wind-tunnel. The specifications of the tunnel at the numbered cross-sections are shown in Table 3.3.

some duct modes only being present at certain orientations of the fan blades, the initial acoustic pressure disturbance was rotated by replacing ωt in the temporal portion of Equation 2.41 with a phase offset that varied from 0 to 2π .

Cross-sectional slices of the acoustic field as the waves march upstream from the fan through the circle to square transition are shown in Figure 3.12. The plots on the left side are at an initial phase angle of 0 radians and the right side are at a phase angle of $\pi/2$ radians. The top plots are the cross-sectional slices of the acoustic field directly upstream of the fan, the middle plots are halfway through the transition, and the bottom plots are just into the square duct. As an acoustic wave propagates upstream, a phase shift can be observed with the halfway transitioned cross-sectional slices having an opposite local phase. As the acoustic wave enters the square duct the 0 radian phase, left side, bears little resemblance to the original acoustic wave while the $\pi/2$ radian phase shows some significant similarities.

The acoustic field cross-section at the center of the test-section is shown in Figure 3.13 for a variety of initial phase angles. As the fan blades rotate so too does the acoustic field within the test-section. The real component of the duct modes are shown in Figure 3.14 as a function of the initial phase angle. The primary duct mode in the test-section is the $m = 2, n = 2$ mode with contributions from pairs of modes $m = 0, 2, n = 2, 0$ which are in phase with one another and out of phase mode pairs $m = 1, 3, n = 3, 1$. Note that for Figures 3.14 and 3.15 the $m = 0, 2, n = 2, 0$

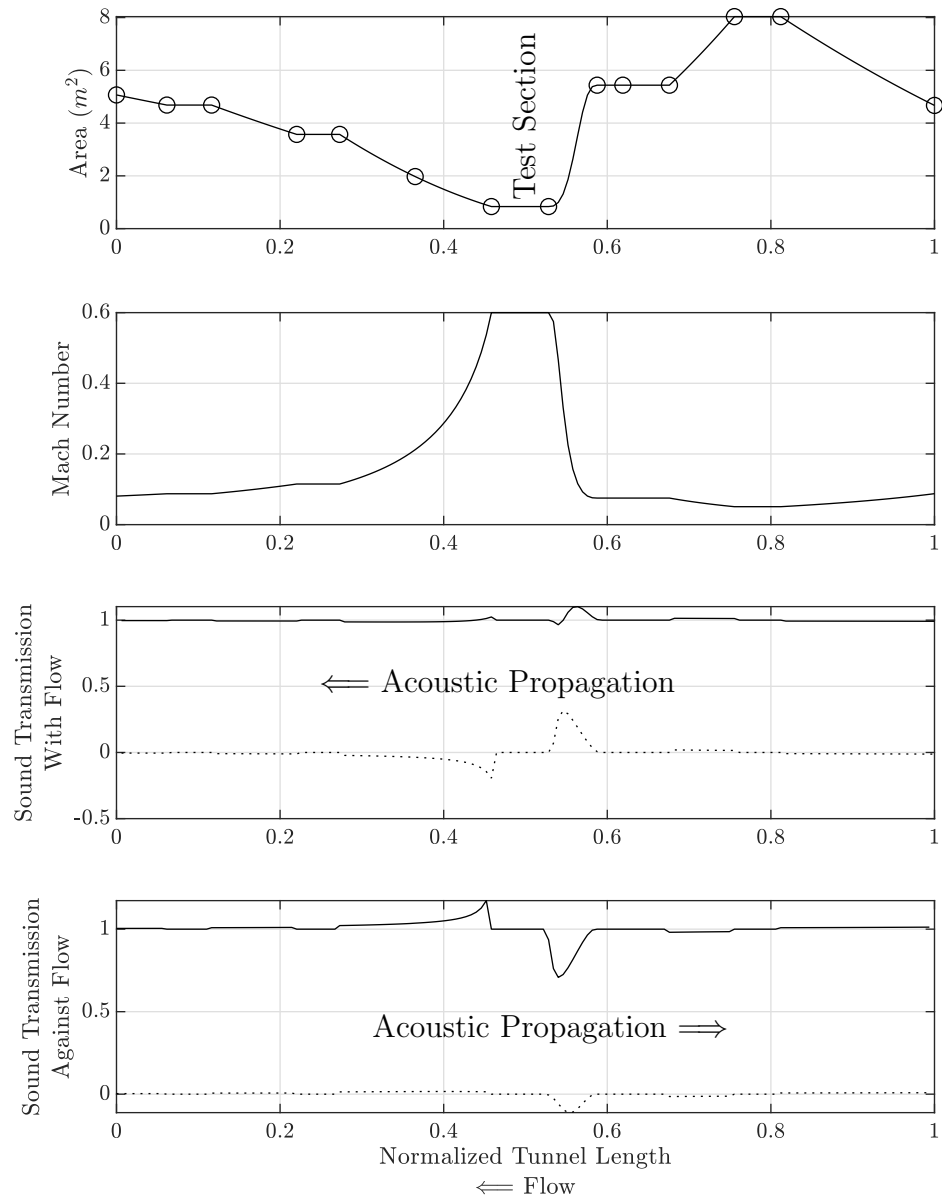


Figure 3.11. Wind-tunnel discretization at a Mach number of 0.6. The solid lines in the sound transmission plots represent the transmitted pressure ratio while the dotted lines represent the reflected pressure ratio.

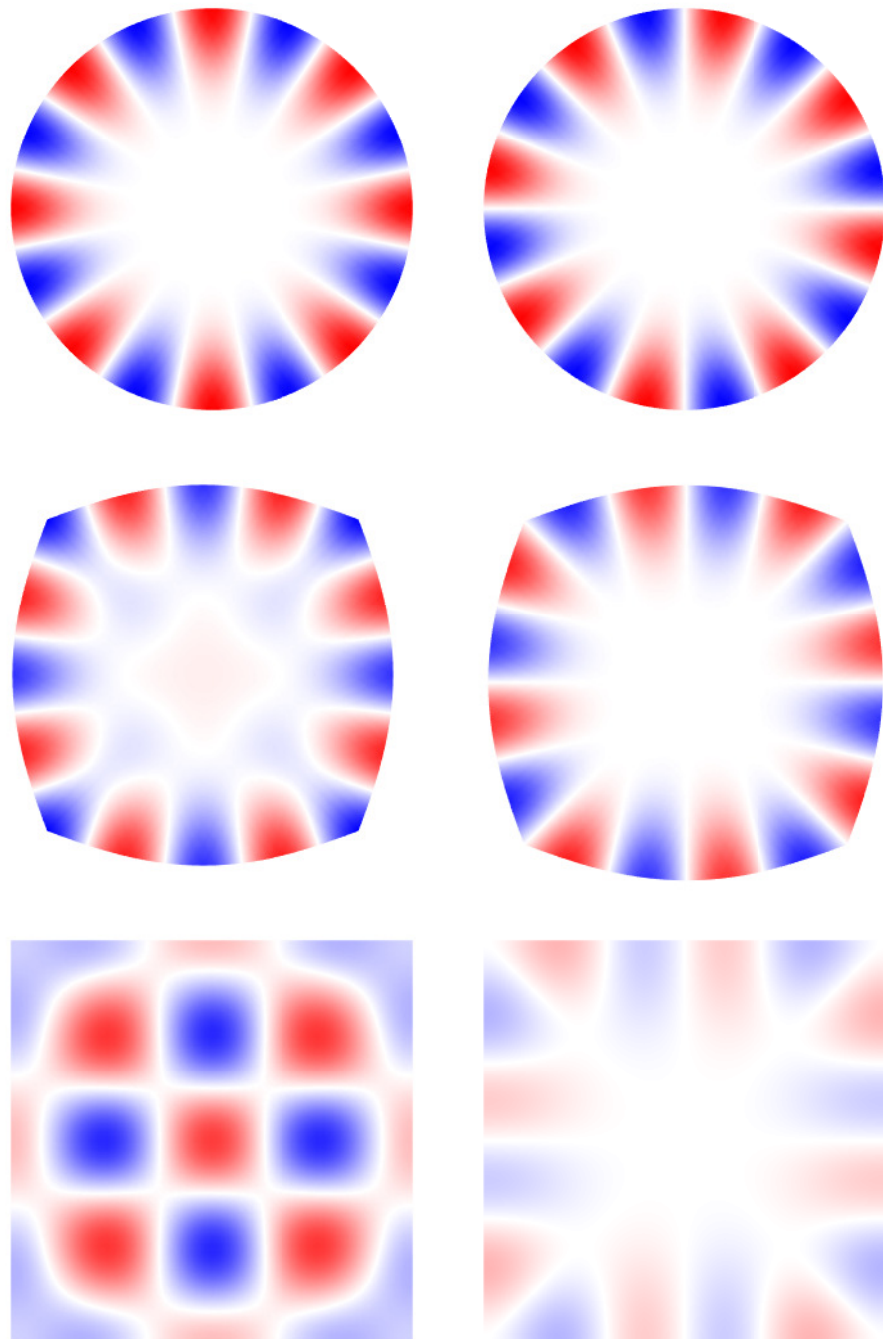


Figure 3.12. Cross-sectional slices of the acoustic field through the circle to square transition for the acoustic waves traveling upstream. Left side are the waves traveling from the fan at a phase of 0 radians and the right side at a phase of $\pi/2$ radians. The top plots are the fan acoustic field, the middle plots are halfway through the transition, and the bottom plots are just into the square duct.

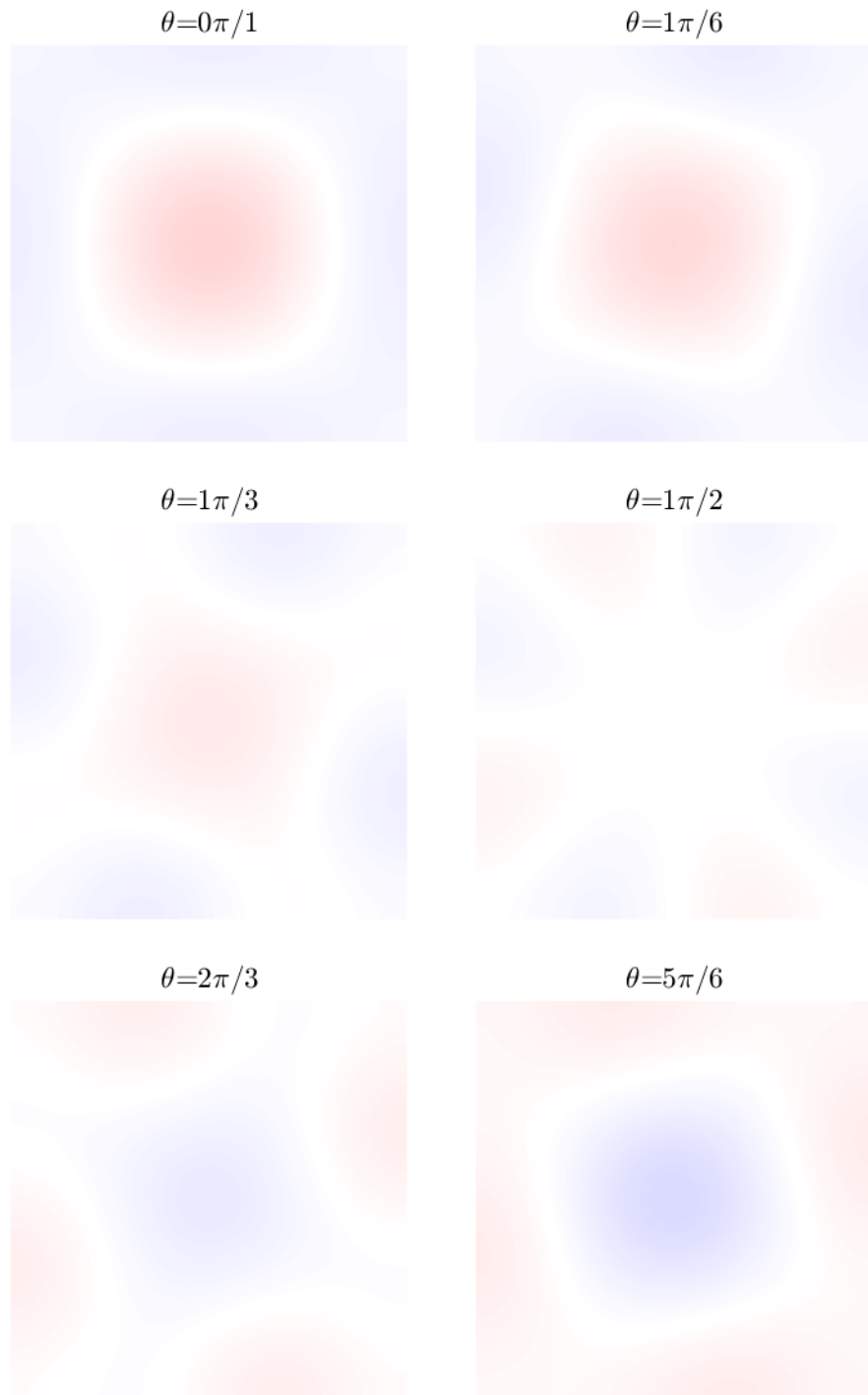


Figure 3.13. Cross-sectional acoustic field slices in the center of the test-section at various initial phase angles.

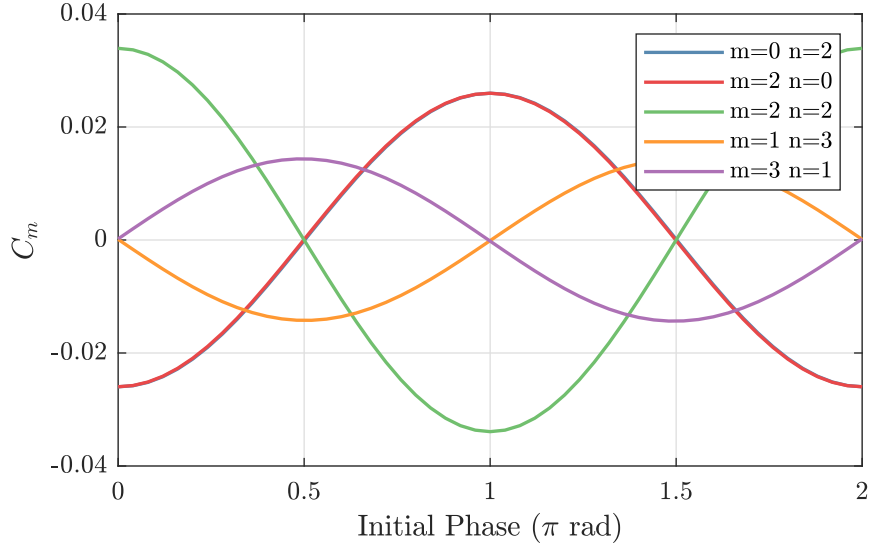


Figure 3.14. The real component of the acoustic mode coefficients making up the upstream-traveling acoustic field in the middle of the test-section as a function of the initial phase angle.

modes overlap one another in the plots. These five modes can be used to simulate the optical response of the fan driven acoustics inside of the test section by using the maximum value of the modal coefficient and a relative phase angle between the different modes by using Equation 2.41 and

$$\widehat{\text{OPD}}(x, y) = \frac{K_{GD}}{c_0^2} \int_{z_1}^{z_2} \hat{p}(x, y, z) A_p dz, \quad (3.24)$$

where $\widehat{\text{OPD}}$ is the complex optical path difference and K_{GD} is the Gladstone-Dale constant. The temporal portion of Equation 2.41 can be applied after the integration process in Equation 3.24 and just before taking the real component to simulate a measured value at a particular instant in time.

The acoustic duct modes in the center of the test-section for the acoustic waves traveling in the direction of the flow are shown in Figure 3.15. The downstream-traveling acoustic field inside of the test-section is comprised of the same duct modes as the upstream-traveling acoustic field but the mode coefficient are approximately an order-of-magnitude lower. All of the phase offsets for the modes remain the same except for the $m = 2, n = 2$ mode which is now different by π radians compared to the upstream-traveling modes in Figure 3.14. When the downstream-traveling acoustic field enters the cruciform after the test-section a portion of it is reflected, see Figure 3.11. When the maximum reflected pressure ratio, approximately -0.2, is combined with the strength of the downstream-traveling acoustic field, the acoustic field reflected back into the test-section is 1-2

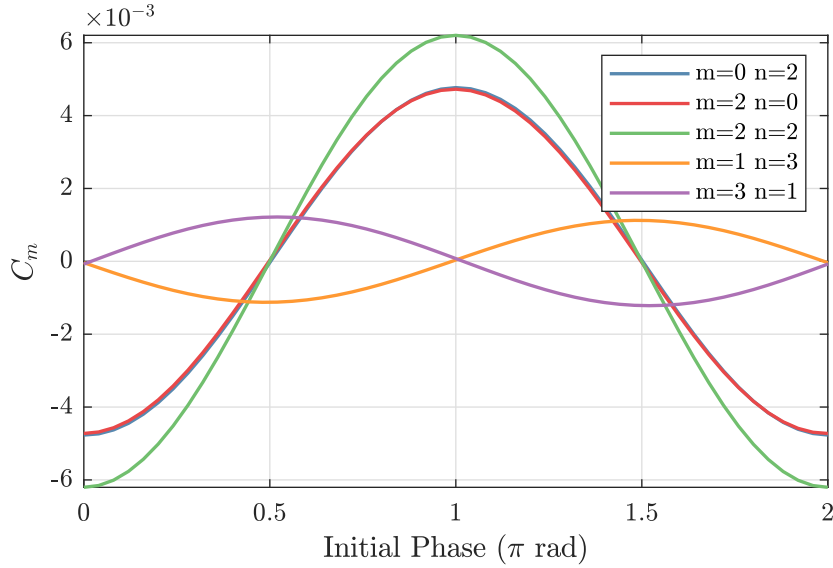


Figure 3.15. The real component of the acoustic mode coefficients making up the downstream-traveling acoustic field in the middle of the test-section as a function of the initial phase angle.

orders-of-magnitude lower than the upstream-traveling acoustic field from the fan. On the other hand, the reflected field from the upstream-traveling acoustic field after it leaves the test-section is on the same order-of-magnitude as the downstream-traveling acoustic field.

A comparison between a measured optical wavefront that has been band-pass filtered at the blade-passing frequency and a simulated optical wavefront that has been shot through the estimated acoustic field computed by the mode-marching method is shown in Figure 3.16. Qualitatively, there is significant agreement between the two wavefronts. Since there was no microphones installed in either the test-section or around the wind-tunnel fan, there cannot be a quantitative comparison made.

3.4 Summary

Acoustic waves affect the transmission of light by causing the local index-of-refraction to change with the pressure fluctuations. When the acoustic field is well modeled, as was the case with the spherical wave measurements, an optical wavefront measurement can provide an accurate measurement of the acoustic field strength non-intrusively.

The mode-marching method provides a computationally rapid way of estimating an acoustic signal as it travels through a duct system like a wind-tunnel. This method assumes that the

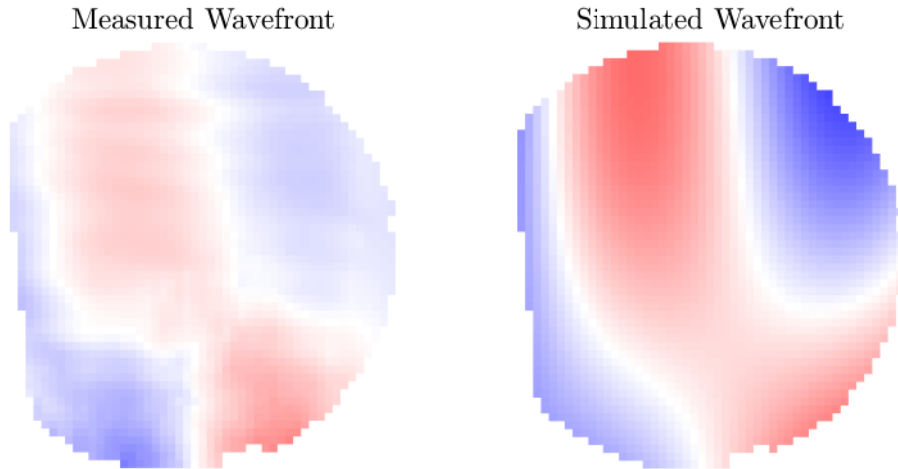


Figure 3.16. Comparison of a measured optical wavefront and a simulated one passing through the estimated acoustic field.

reflected component will be minimal and can be ignored. A significant contribution of this work to the computational procedure of this method is computing the eigen-functions for the wind-tunnel fan transition geometries that are neither circular nor rectangular. These computations would become even more costly if the cross-section cannot be assumed to have a uniform flow speed [64]. Finally, note that the mode-marching method used here has neglected the effect that the corners would have on the signal or other internal geometry such as the turning vanes or the turbulence screens.

The main benefit to using a mode-marching method is to simulate narrow-band signals that appear in the optical wavefront spectra and to have some level of confidence that the source of that signal is the wind-tunnel fan. If the narrow-band signal does not match up with the simulated signal, it could have a source that may not be due to the testing environment and would likely need to be investigated further. If there is significant agreement between the measured and simulated signals, a simple stop-band filter could be used to eliminate the contamination.

CHAPTER 4

MULTIDIMENSIONAL SPECTRAL ESTIMATION OF OPTICAL WAVEFRONTS

As described in Chapter 1, the objective of this research is to develop methods to evaluate and, if possible, eliminate the effect of facility-related acoustic noise on aero-optical measurements. As such, the first goal of the research is to establish analytical methods to identify and isolate acoustic sources of optical signals within a given data sample. This is a significant challenge since, as will be shown later, acoustic sources of optical aberrations typically have a magnitude and frequency content that is in the same range as the signal that is the objective of the measurement. This chapter will begin with a brief overview of some of the benefits to analyzing multidimensional data in this way, followed by a short discussion on how these spectra are calculated, and conclude with a more in depth discussion of the analysis of multidimensional spectral estimates.

The multi-dimensional spectral approach that is employed throughout this research helps identify and characterize acoustic sources of optical noise as well as aero-optical signals. The spectral approach is also used as the basis for methods to filter the acoustic sources. For measurements in multiple dimensions, such as a line of sensors that are recorded over time, a multidimensional spectral estimation not only produces temporal frequency content but can also be used to identify the direction and speed of travel of a particular wave.

The benefits of using multidimensional spectral estimation are shown in Figure 4.1. The spectra shown in the figure were computed using the OPD measured by a single row of sub-apertures from a Shack-Hartmann optical wavefront measurement in which a 5 inch diameter beam was propagated normally through a wind-tunnel test section with a free-stream Mach number of 0.5. This measurement was performed in the University of Notre Dame White Field Wind Tunnel in a test section that contained a model representing the fuselage of the AAOL aircraft [33] with window that was flat and flush to the outer mold line of the fuselage. The top plot shows a traditional power spectrum ensemble-averaged over the row of data. Both the blade-passing frequency (517 Hz) and its sub-harmonic had similar amplitudes with an additional five harmonics showing significant peaks. There are three additional strong peaks at approximately 3100, 4850, and 5850 Hz that are likely due to fan vibration that limited the top speed of the tunnel for the test.

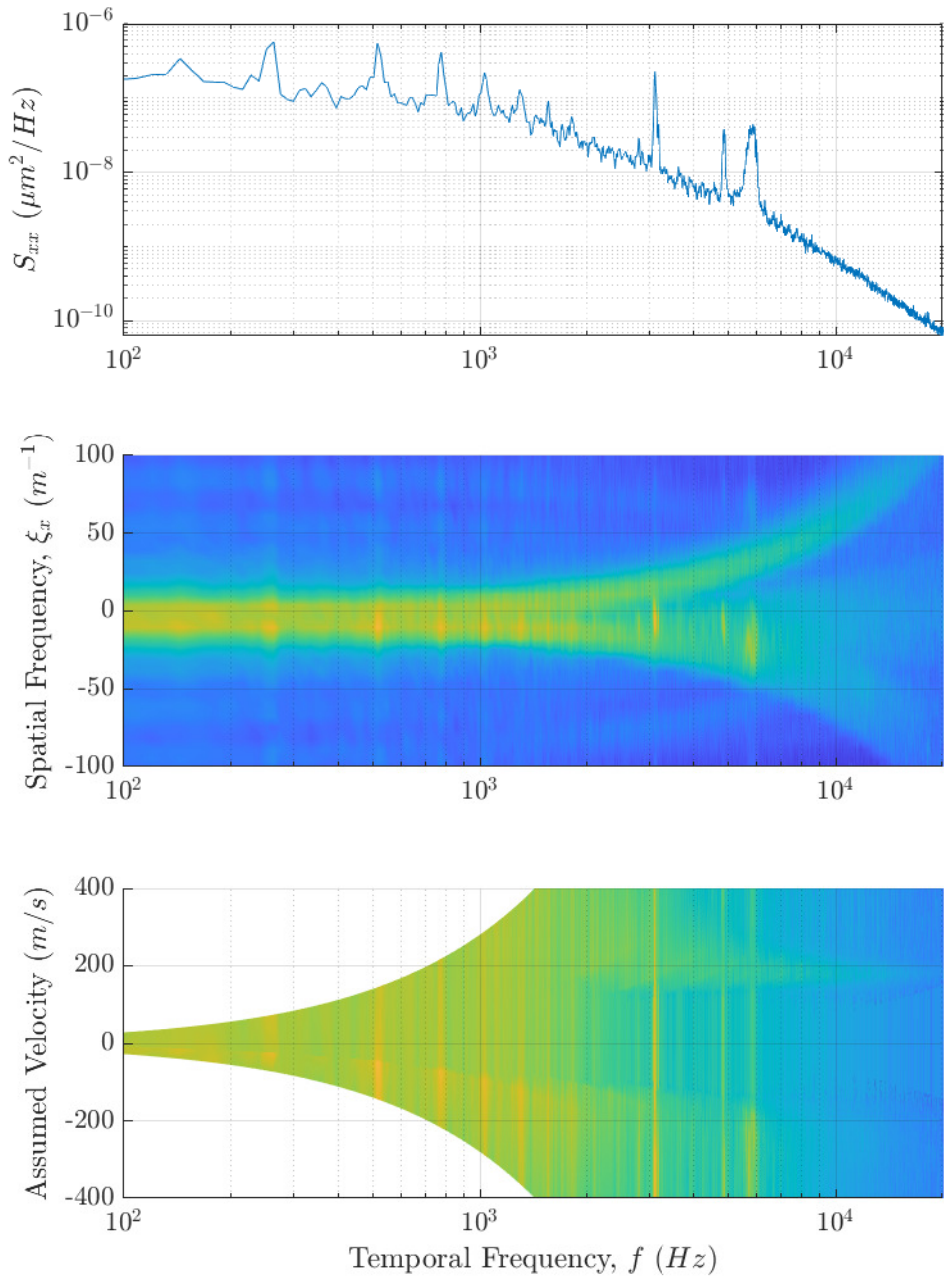


Figure 4.1. Multidimensional spectral estimation plot example and comparison to traditional power spectrum measurements. A single row of an optical wavefront measurement was used in this example. The top plot shows the typical power spectrum averaged over the entire row of data. Both the middle and bottom plots show the multidimensional spectrum plot with the y-axis as spatial frequency in the middle and velocity in the bottom assuming $u = f/\xi_x$.

Both the middle and bottom plots show the multidimensional spectral estimation of the two-dimensional data, $\text{OPD}(x, t)$. Since the figure is for illustrative purposes, colorbars were not shown; however, the color is representative of the logarithm of the power or variance in the wavefront signal (i.e. $\text{OPD}_{\text{RMS}}^2$) with yellow representing more power and blue representing less. The colorbar range in this figure is the same for the middle and bottom plots and is consistent with the other plots throughout this chapter. In the middle plot the y-axis represents the stream-wise spatial frequency, ξ_x with the units of inverse meters. It is important to note that, unlike temporal frequencies, spatial frequencies can have positive or negative values depending on the direction of travel of the disturbance, in Figure 4.1, waves with positive spatial frequencies are moving in the direction of flow. In the middle plot of Figure 4.1, there is a strong signal that roughly lies on the zero spatial frequency ($\xi_x \approx 0$) axis up to a frequency of 2000 Hz, after which the signal in the spectrum can be clearly seen to branch off into upstream- and downstream-moving disturbances. The cause of the branching in the signal will be discussed later, however note that the reason why the signal appears to lie on $\xi_x \approx 0$ at low frequencies is simply an artifact of plotting the spectrum on semilog axes (which was done to better resolve the peaks in the power spectrum in the top plot of the figure); as shown later in plots with linear axes, the signal actually branches off into upstream- and downstream-moving disturbances even at low frequencies. The blade-passing frequency and its various harmonics can also be discerned in the center plot, by the vertical “streaks” that line up with the peaks in the standard spectrum shown in the top plot; the center spectral plot shows that these fan blade-passing signals have significant broadband spatial frequency content. All of these narrow-band signals have a majority of their signal traveling upstream. In addition to optical disturbances branching off in the upstream and downstream moving directions there are significant disturbances along zero spatial frequency representing a collection of standing waves. As already mentioned, the data in Figure 4.1 were plotted logarithmically along the temporal-frequency axis to better show the low frequency content around the fan blade-passing frequency, and how the peaks in the power spectrum in the top plot still appear in the multidimensional spectrum in the middle plot. As shown later, when the multidimensional spectrum is plotted linearly, the two primary upstream and downstream traveling signals lay in a straight line.

A dispersion analysis can be performed on these multidimensional spectral estimates. In order to obtain the velocity of a given wave we can start with the most basic forms of the wave equation,

$$\hat{y} = a \exp\{j\theta\}, \quad (4.1)$$

where θ is the phase of the wave and equal to $kx - \omega t$. From here we can take the partial of θ with respect to time and set it equal to zero,

$$\frac{\partial\theta}{\partial t} = 0 = \frac{\partial k}{\partial t} \frac{\partial x}{\partial t} - \frac{\partial\omega}{\partial t} \frac{\partial t}{\partial t}, \quad (4.2)$$

which can be rearranged to

$$u = \frac{\partial\omega}{\partial k} = \frac{\partial f}{\partial\xi}. \quad (4.3)$$

If we are to assume that a wave packet intercepts the origin ($f = \xi = 0$) then every point on the spectral plot can be assumed to have a disturbance velocity,

$$u_d = \frac{f}{\xi_x}. \quad (4.4)$$

This relationship shows that, for a nondispersive medium such as air, the spatial frequency of a disturbance is related linearly to the temporal frequency as $1/u_d$. The bottom plot shows the same multidimensional spectral estimation plot as the middle one but with the y-axis showing disturbance velocity u_d . The bottom plot shows that the primary optical disturbance moving in the direction of flow is moving at the free-stream velocity of approximately 175 m/s. The upstream traveling disturbance is traveling at the same speed but due to the signal being broader is more difficult to measure this way. Note that the stationary modes along $\xi_x \approx 0$ in the middle plot are nowhere to be found on the bottom plot; this is because when the disturbance velocity for these waves is calculated their speed approaches infinity.

4.1 One-Dimensional Power Spectrum Calculation

Power spectral analysis is typically performed on one-dimensional data sets, for example, a single sensor measurement over time. On the other hand, as shown in Figure 4.1, if a sensor array were used, a multi-dimensional power spectrum could be computed that would also show spatial frequency information. For a single-point measurement that varies in time, $x(t)$, the power spectrum calculation is

$$S_{xx} = \frac{|\text{FFT}\{x(t)\}|^2}{Nf_s}, \quad (4.5)$$

where FFT is the Fast Fourier Transform, N is the number of samples, and f_s is the sample rate [4]. For data that has only a real component the Fast Fourier Transform function produces magnitude and phase relations at each frequency step, f_s/N , over the range from zero-frequency up to but

not including the Nyquist frequency, f_s/w , with a mirrored set of data that can be represented either below (starting at $-f_s/2$) or above (ending just below f_s) this range. The Nyquist frequency not being included and the mirrored data is due to an assumption that is integral to the Fourier Transform, which is that the signal is assumed to be periodic.

The total energy, σ^2 , of the signal must be preserved through the transform from physical space-time to frequency space

$$\sigma^2 = \frac{\sum x^2(t)}{N} = \Delta f \sum S_{xx}(f). \quad (4.6)$$

Additionally, because of the periodic nature of the Fourier Transform and a finite sample length of discrete data, spectral leakage can cause the power in one frequency bin to leak into adjacent frequency bins. To minimize this spectral leakage, windowing functions are employed which typically force the end points of the signal to zero. The Hann window,

$$w(t) = 1/2 \left[1 - \cos \left(\frac{2\pi t}{T} \right) \right], \quad (4.7)$$

is one of the more commonly used windowing functions [6] where $w(t)$ is the window function, t is the time at a given sample, and T is the total sample time. Since the windowing of a data set changes the signal energy some correction is needed to be applied. For an arbitrary windowing function the correction factor, c_w , can be obtained by substituting the windowing function in place of $x(t)$ in Equation 4.6,

$$c_w = \frac{1}{\sqrt{\sum w^2(t)/N}}. \quad (4.8)$$

For a Hann window this correction factor approaches $\sqrt{8/3}$ as N goes to infinity. When Equation 4.5 is combined with a windowing function and associated correction the double sided power spectra equation in one dimension becomes

$$S_{xx} = \frac{|c_w \text{FFT}\{x(t)w(t)\}|^2}{Nf_s}. \quad (4.9)$$

4.2 N-Dimensional Power Spectra Calculation

For measurements with multiple spatial and temporal dimensions the Fast Fourier Transform is applied n -times where n is the total number of dimensions, with each application in a different

dimension,

$$\text{FFT}_n(x) = \text{FFT}(\text{FFT}(\cdots \text{FFT}(\text{FFT}(x, 1), 2) \cdots, n-1), n), \quad (4.10)$$

where $\text{FFT}(x, n)$ is the Fast Fourier Transform of x in the n^{th} dimension [3]. For a n -dimensional array the operation becomes [43]

$$\mathbf{S}_{\mathbf{xx}} = \frac{|c_w \text{FFT}_n\{f(\mathbf{x})w(\mathbf{x})\}|^2}{\prod \vec{N} \vec{f_s}}, \quad (4.11)$$

where $\mathbf{S}_{\mathbf{xx}}$ is the n -dimensional power spectra array or dispersion array, $f(\mathbf{x})$ is an n -dimensional set of data, $w(\mathbf{x})$ is an n -dimensional windowing function, \vec{N} is a vector denoting the number of elements in each dimension, $\vec{f_s}$ is a vector denoting the sample rate in each dimension, and

$$c_w = \frac{1}{\sqrt{\sum w^2(\mathbf{x}) / \prod \vec{N}}}. \quad (4.12)$$

The signal energy conservation relationship becomes

$$\sigma^2 = \frac{\sum \mathbf{x}}{\prod \vec{N}} = \prod \vec{\Delta f_s} \sum \mathbf{S}_{\mathbf{xx}}, \quad (4.13)$$

where $\vec{\Delta f_s}$ is a vector representing the frequency step sizes in each dimension.

4.3 Non-Rectangular Spatial Windows

For n -dimensional data sets that fill a rectangular array, a windowing function can be created by multiplying together a series of one-dimensional windowing functions in the direction of each dimension. For non-rectangular data sets, such as is often the case with optical wavefront measurements, a windowing function can take some additional steps in its construction. In cases when the spatial measurement locations are constant throughout time, the windowing function can be split into two separate components,

$$w(\mathbf{x}) = w_t(t) \cdot w_s(x, y), \quad (4.14)$$

the temporal windowing function, $w_t(t)$, and the spatial windowing function, $w_s(x, y)$. This study uses a Hann window for the temporal windowing function and a modified Hann window for the spatial windowing function. For the case of a perfectly circular aperture, the Hann window can be

reformulated to be based on the normalized radius, ρ_N , of the aperture,

$$w_s(\rho_N) = \begin{cases} \frac{1+\cos(\pi \cdot \rho_N)}{2} & \text{if } \rho_N < 1 \\ 0 & \text{otherwise.} \end{cases} \quad (4.15)$$

This modified Hann window is two-dimensional with a value of one at the center of the aperture and decreases to zero at the edge of the aperture in the same manner as a Hann windows decreases from the center to either end.

Because the wavefronts measurements often had a clipped edge or some other obscuration, a different method was employed in this study. For an arbitrary shaped aperture, the minimum distance from any given measurement location to the edge of the aperture was used to create the spatial windows. The minimum distance can be computed given the a set of points (x and y) that spans the measurement range and the set of points outside of the aperture (x_O and y_O),

$$d_{min}(x, y) = \min \left\{ \sqrt{(x - x_O)^2 + (y - y_O)^2} \right\}. \quad (4.16)$$

This distance is then normalized by the maximum value and the resulting spatial window given a modified Hann window,

$$w_s(x, y) = \frac{1 + \cos \{ \pi \cdot (1 - d_{min}^{norm}(x, y)) \}}{2}. \quad (4.17)$$

This same basic idea can be extended to data sets where the locations of measurements in space vary with time.

4.4 Wavefront Multidimensional Spectrum

At the beginning of this chapter a multidimensional spectral plot for data resolved in time and one spatial dimension was shown along with a typical power spectrum plot in Figure 4.1. This was shown to facilitate a simple discussion of some of the benefits of using multidimensional spectrum analysis on optical wavefronts. That simple analysis was performed on only a single row of a wavefront data set and provided an insight into the disturbances that were moving in the horizontal (stream wise) direction only. When multidimensional spectral estimation is performed over all dimensions of a wavefront (i.e. time and both spatial dimensions), as will be done for the remainder of this chapter, additional detail is available, that also enables the determination of optical disturbances

moving vertically (i.e. cross-stream to the flow) or in any direction in between. Figure 4.2 shows a comparison between the two-dimensional single row spectrum (bottom plot) with two different representations of the same two-dimensional spectrum extracted from a three-dimensional spectral calculation. Specifically, the top plot in Figure 4.2 shows the “slice” of the three-dimensional spectral estimation plot taken at $\xi_y = 0 \text{ m}^{-1}$; because this slice does not contain any information on vertically-moving disturbance, it shows planar waves traveling in the horizontal direction. The middle plot shows the same three-dimensional spectrum integrated through the vertical spatial frequency axis to create an estimate of the two-dimensional spectrum. The bottom plots shows the two-dimensional spectral plot that was previously shown in Figure 4.1 but this time with a linear temporal frequency axis. Both of the two-dimensional spectra in the top two plots of Figure 4.2, whether directly computed or integrated show a significant increase in the signal content between the acoustic lines ($u \pm c$).

The three-dimensional spectral slice (top plot) shows significant signal energy at the same characteristic velocities of the free-stream velocity, u , and the acoustic lines, $u \pm c$, as the two-dimensional spectrum (bottom plot), along with some additional signal laying along the temporal-frequency axis at $\xi_y = 0 \text{ m}^{-1}$. This signal represents a collection of stationary modes at each temporal frequency. If this were a flow-related phenomenon the velocity of the disturbance according to Equation 4.4 would be near infinity; as such, it is more likely caused by mechanical vibration of the wind tunnel and components of the optical measurement system. On the three-dimensional spectrum plot there are signals that run parallel to u and $u - c$ that do not emanate from the origin but from $\xi_x \approx \pm 80 \text{ m}^{-1}$; at present an explanation for these signals cannot be given; however, it is possible that this effect is caused by an optical ghost image. There is also an aliased signal that runs parallel to $u + c$ starting on the right side of Figure 4.2 top at $\xi_x \approx -50 \text{ m}^{-1}$ and decaying towards the left. Aliased signals are due to the sample rate, either spatial or temporal, being to low.

The middle plot of Figure 4.2 shows the integrated spectrum through the vertical spatial frequency axis. This integration captures the energy in all vertical disturbances which effectively recreates the two-dimensional spectrum plot on the bottom of Figure 4.2. A reduced order spectrum like this is calculated by

$$S_{xx}^{n-1} = \int S_{xx}^n df_s^m, \quad (4.18)$$

where S_{xx}^n is the n-dimensional spectrum and df_s^m is the differential frequency in the m -th dimension. This is also shown in Figure 4.3. While the integrated signal over estimated the spectrum going from three-dimensions to two in Figure 4.2, it under estimates the spectrum going from two to

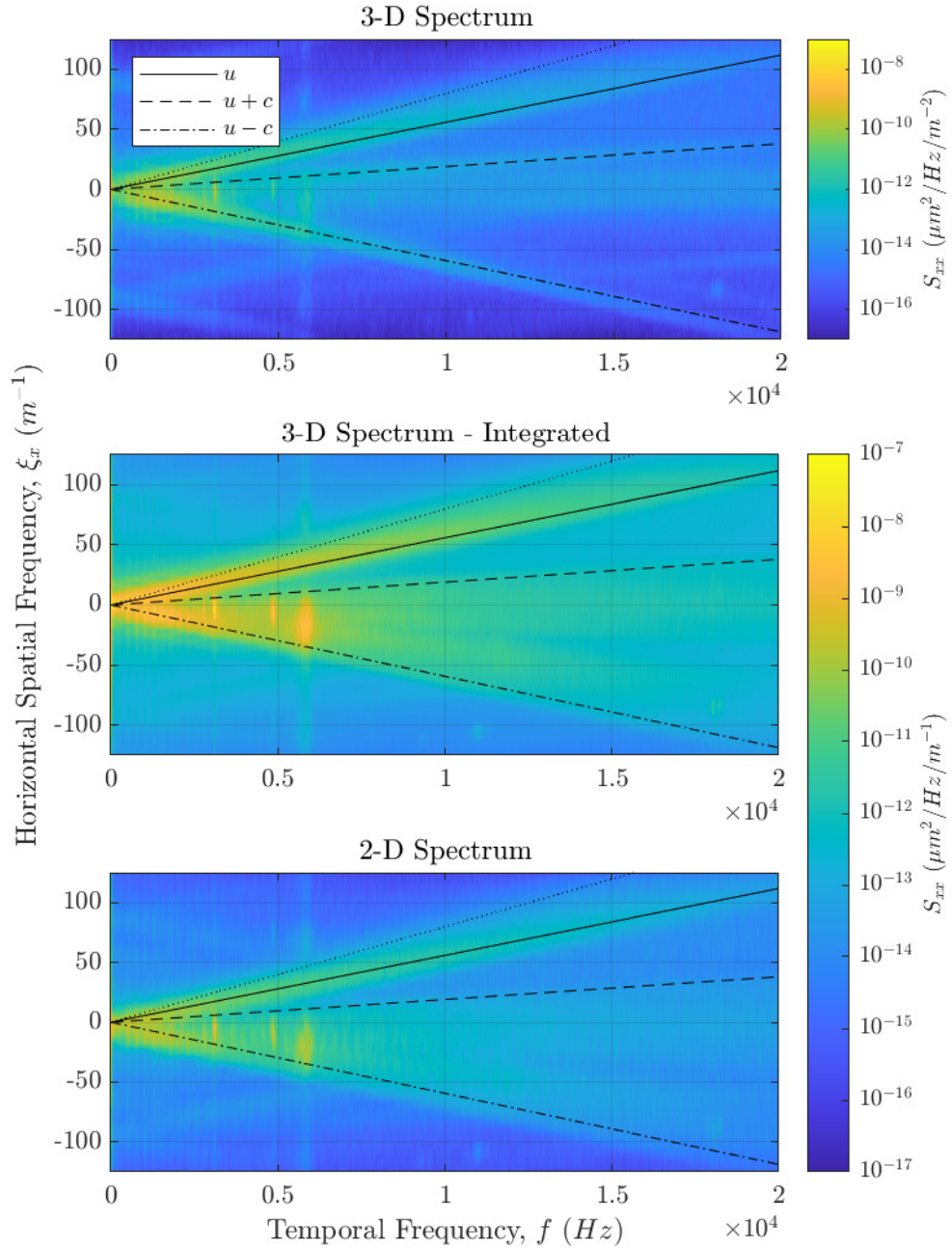


Figure 4.2. Horizontal moving optical disturbances comparison. The top plot shows a slice of the three-dimensional spectrum focusing on the plane waves that are traveling in the horizontal direction. The middle plot is a recreation of the two-dimensional spectrum by integrating through the the vertical spatial frequencies. The bottom plot is the two-dimensional spectrum.

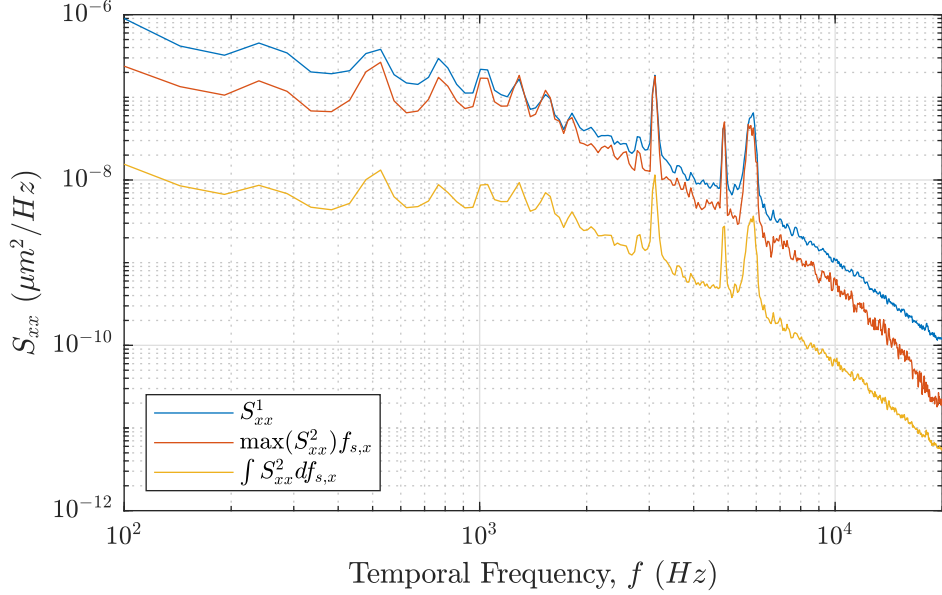


Figure 4.3. Recovery of time-based power spectrum from two-dimensional spectral estimate.

one dimensions. Unfortunately, due to the limited number of spatial sample points and the large dynamic range of the signal, this integrated value can contain a significant amount of error.

Due to the the signal containing a majority of the power in a limited number of spatial frequency bins, a reduced order spectrum can be estimated by

$$S_{xx}^{n-1} \approx \max(S_{xx}^n, m) f_s^m, \quad (4.19)$$

where $\max(S_{xx}^n, m)$ is the maximum value of the spectrum along dimension m and f_s^m is the sample rate for that dimension. The calculated temporal power spectrum from the two-dimensional spectrum using the maximum value is a good estimation at the center of the frequency range but has some additional decay at both low and high frequencies. The calculated reduced order spectrum in Figure 4.3 (red curve) appears to follow the functional form of the actual one-dimensional spectrum (blue curve) but with a small offset.

4.4.1 2-D Slices of the Multidimensional Spectral Estimation

The full multidimensional spectrum contains information of flow features that are not only moving in the horizontal (stream-wise) direction as the two-dimensional dispersion showed but also

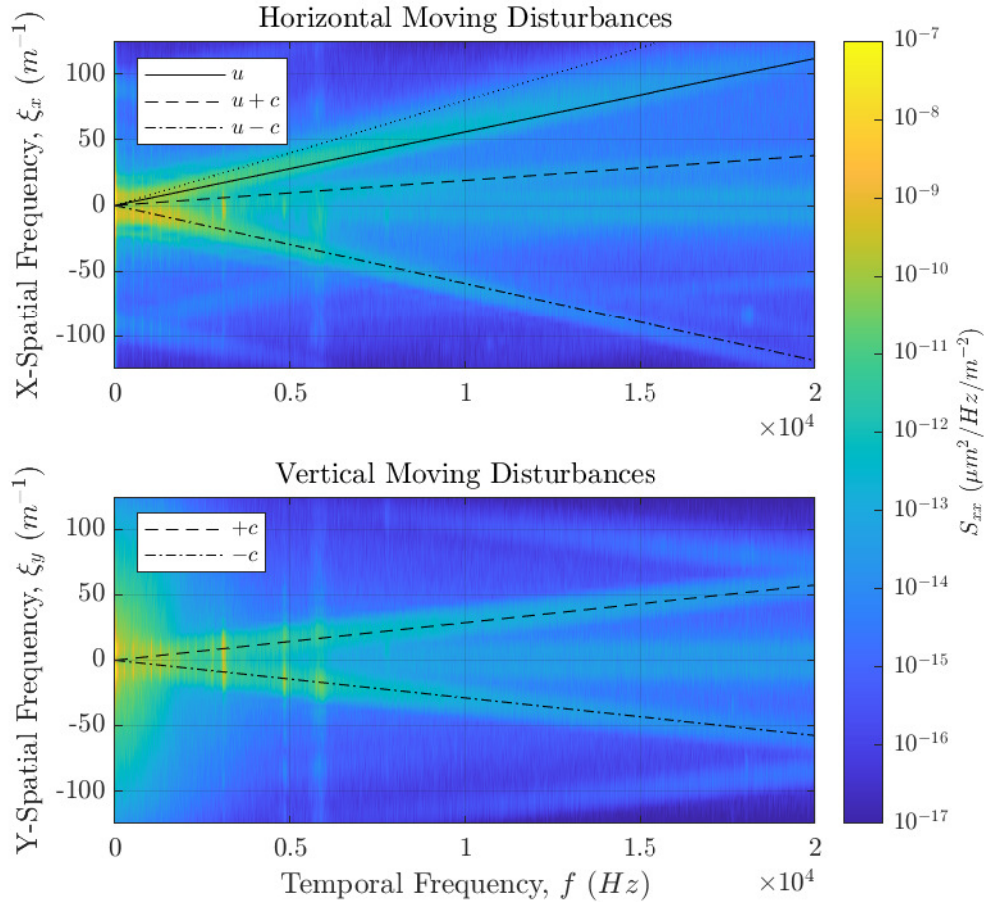


Figure 4.4. Horizontal and vertical moving optical disturbances. This is the same data as presented in Figure 4.1 but after calculating the full three-dimensional spectral estimate. These optical disturbances are plane waves that are traveling solely in their respective directions.

in every direction of the two-dimensional optical wavefront. Figure 4.4 shows two-dimensional slices of the full spectrum that on the top show the horizontal (stream-wise) moving disturbances for a vertical spatial frequency of $\xi_y = 0 \text{ m}^{-1}$ and on the bottom show the vertical (cross-stream) moving disturbances for a horizontal spatial frequency of $\xi_x = 0 \text{ m}^{-1}$. Since the wavelength is $\lambda = 1/\xi$, the waves that make up the disturbances shown in these slices are plane waves that are traveling solely in the horizontal or vertical directions.

The top plot of Figure 4.4 shows the two-dimensional spectrum for horizontally moving optical disturbances that was shown previously. There are three major flow-related structures that can be observed. The large signal that lays along u (solid line in Figure 4.4) is the aero-optical effect of the

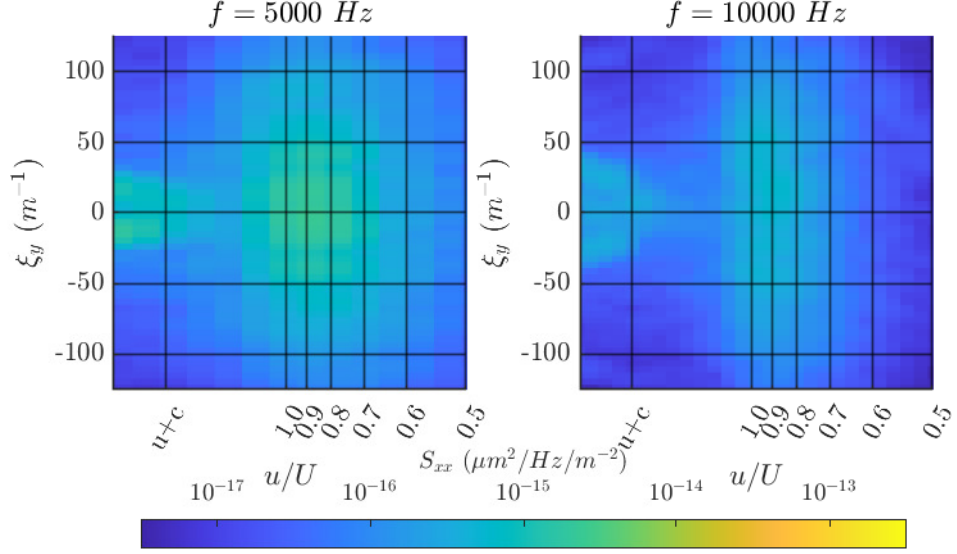


Figure 4.5. Temporal-frequency slices at 5 and 10 kHz with the various horizontal velocities labeled.

boundary layers on both walls of the wind tunnel. It can be seen that the boundary-layer signal has a peak slightly less than the free-stream velocity, u , and has a slight decay as the velocity decreases away from the peak and a sharp decay as the velocity increases. For reference, the dotted line at the top of Figure 4.4 denotes a velocity of $0.7u$. The velocity of the strongest aberrating structures in the boundary layer has typically been reported as approximately $0.83u$ [23], however, this data shows the boundary layer velocity has a range of velocities at each given frequency in which the peak velocity component has some dependence on the temporal frequency. This can be more clearly seen in two temporal frequency slices in Figure 4.5 which shows vertical spatial frequency plotted against the normalized horizontal (stream-wise) velocity. Again, the figure shows strong decay of the signal as the speed increases above the free-stream velocity and gradual decay as the speed decreases. There is also additional signal decay as the absolute value of the vertical spatial frequency increases. The velocity of this boundary layer optical disturbance will be measured in Chapter 6 using a velocity filter to show a mean velocity of $0.85u$, which is near the generally accepted value of $0.83u$ [23].

The other two major flow-related structures in Figure 4.4 are related to acoustic signals traveling in both directions through the wind-tunnel, denoted by the dashed and dot-dash lines in the figure. The downstream-traveling acoustic wave, $u + c$, has a low signal power than the upstream-traveling

acoustic wave, $u - c$. The likely explanation for this difference in signal power is that most of the acoustic energy in the wind tunnel is generated by the fan which propagates upstream and downstream within the wind-tunnel ducting. However, sound waves that move in the flow direction have their wavelength stretched as the flow is accelerated into the test-section contraction, while sound waves moving against the flow have their wavelength contracted. Hence the downstream-traveling waves have a longer wavelength as they pass through the measurement beam and thus more of the optical signal from the downstream-travelling waves is filtered out due to aperture filtering [56]. At low temporal frequencies, the blade-passing frequency (520 Hz) and its associated harmonics appear as vertical lines with regular spacing in Figure 4.4.

The two main features on the vertical spectral slice plot on the bottom of Figure 4.4 are the signals moving at the speed of sound ($\pm c$) including some significant aliasing of these signals. These two lines represent acoustic waves that are traveling either straight up or down through the measurement beam. The blade-passing frequency and its harmonics are also visible in the vertical moving wave plots in both directions and have much less broadband spatial content in the vertical direction. There are also high temporal frequency narrow-band signals ($\sim 3, 5$, and 6 kHz) that contain most of their signal power at the speed of sound lines. These signals have some dependence on the free-stream Mach number (see Figure 4.7). These maybe vibrations originating from the tunnel fan that are currently limiting the top speed of the tunnel; some older optical wavefronts collected in this tunnel under similar measurement conditions do not show these narrow-band signals. Because the portion of these signals with the most power is traveling vertically through the test section instead of stream wise, the tunnel walls maybe excited by the fan and resonating.

The stationary modes that have been discussed previously that appear as a broad horizontal band along the temporal frequency axis in the horizontal spectral slice plot also appear in the same location in the vertical spectral slice plot. These stationary modes appear to be constant when viewed from either direction and through out time. As stated by Blackman and Tukey, this kind of white-noise is generally not physical unless it is bandwidth limited with a falloff of at least $1/f^2$ [4]. Some of these stationary modes are likely cause by vibrations of various optical elements, especially at low temporal frequencies. At higher temporal frequencies, the stationary modes maybe related to electronic noise from the high-speed camera, higher order optical noise from the laser, or even numerical error from the processing code.

4.4.2 3-D Representations of Multidimensional Spectral Estimation

While the two-dimensional slices are fairly informative, particularly when it comes to signal strength of various flow structures and their velocities, a three-dimensional plot allows better visualization of the overall flow structures although some details are lost because typically only one power level can be plotted at a time. The same data that has been previously shown in two-dimensional form, is depicted in Figure 4.6 as an isosurface with a power of $10^{-14} \mu\text{m}^2/\text{Hz}/\text{m}^{-2}$ and shown from four different views. The largest feature is the boundary layer signal which resembles an ellipsoidal plane that is tilted in the $f - \xi_s$ plane. The other main feature is the acoustic signal which appears as a cone which is slightly tilted in the direction of upstream-moving disturbances. The acoustic signal separates into several spikes at high temporal frequencies some of which are constructive interference from aliased signal ($\xi_x \approx 25 \text{ m}^{-1}$, $\xi_y \approx \pm 60 \text{ m}^{-1}$, and $f \approx 20 \text{ kHz}$) which is better visualized in the 20 kHz temporal frequency spectral slice in Figure 4.5. There may also be a small number of dominant duct modes at these high temporal frequencies. The last feature is the stationary modes which appears as the cylindrical structure along the center of the plot (near zero spatial frequency in x and y), which have a near constant shape and magnitude through all temporal frequency ranges.

Figure 4.7 shows two views of an isosurface of the multidimensional spectrum over a range of Mach numbers. All of these plots are of an isosurface with the same power as used in Figure 4.6. The stationary modes seem to be constant throughout the range of Mach numbers indicating that they are most likely not flow related. The boundary layer signal increases in power significantly as the Mach number is increased while also the slope and thus the velocity is significantly increased as well. As shown in and discussed in Chapter 2, the aero-optical OPD_{RMS} of the flat-plate boundary layer on the walls of the wind tunnel is expected to vary according to Equation 2.23. Hence the significant increase in the power of the boundary-layer spectrum with Mach number that can be observed in Figure 4.7 is expected based on the M^2 dependence in Equation ???. The increase in slope of the boundary-layer signal is also expected, and is caused by the increase in the convection speed of the boundary-layer aero-optical disturbances as the free-stream Mach number increases. The acoustic signal sees some interesting evolution as well. Along with the strength greatly increasing with Mach number, the slope of the upstream traveling disturbances decreases significantly while the downstream moving acoustic disturbances do not see much change other than an increase in signal strength.

As the angle of the optical beam changes as it passes through the test section the horizontal

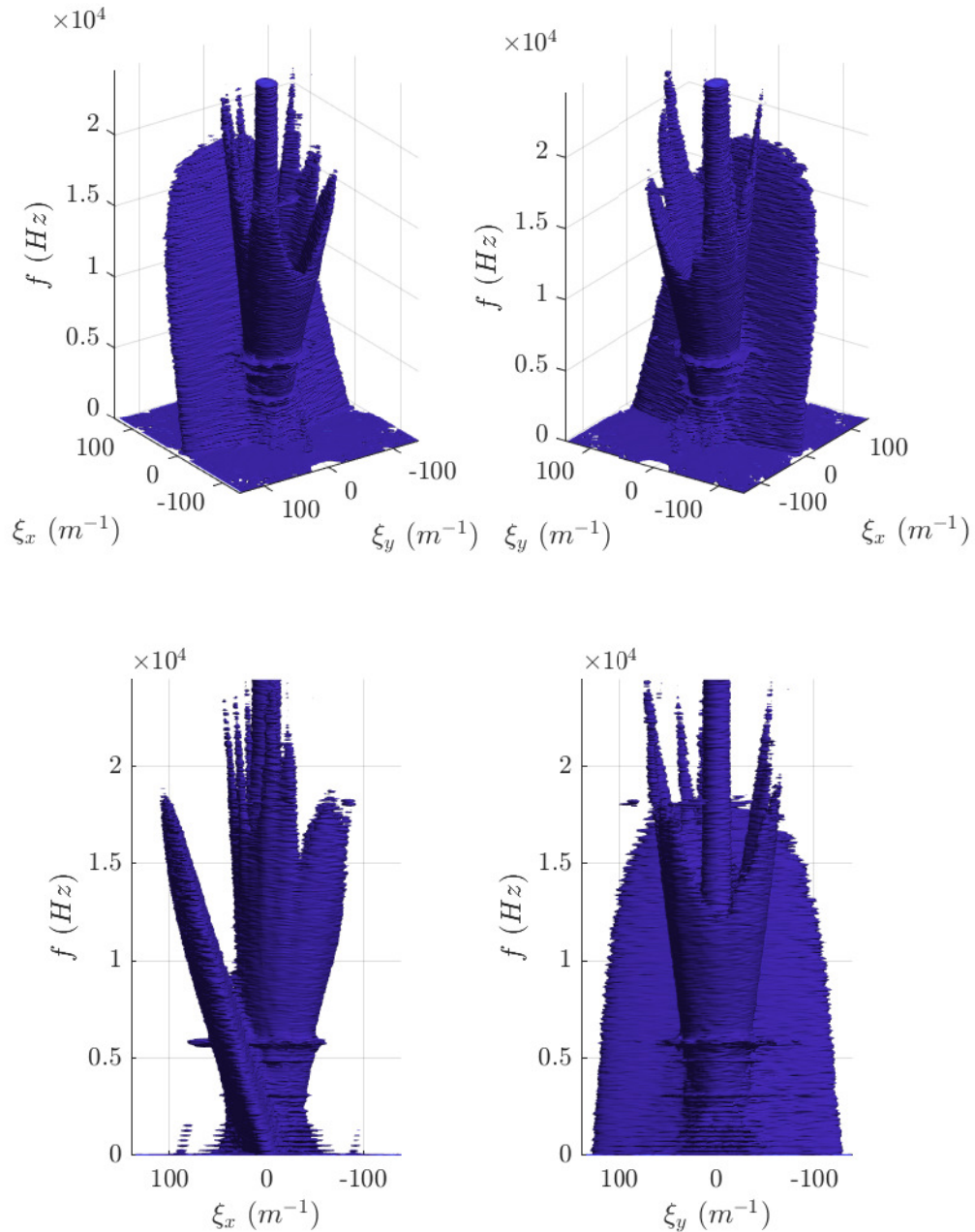


Figure 4.6. Three-dimensional view of the multidimensional spectral plot showing an isosurface at a power of $10^{-14} \mu\text{m}^2/\text{Hz}/\text{m}^{-2}$.

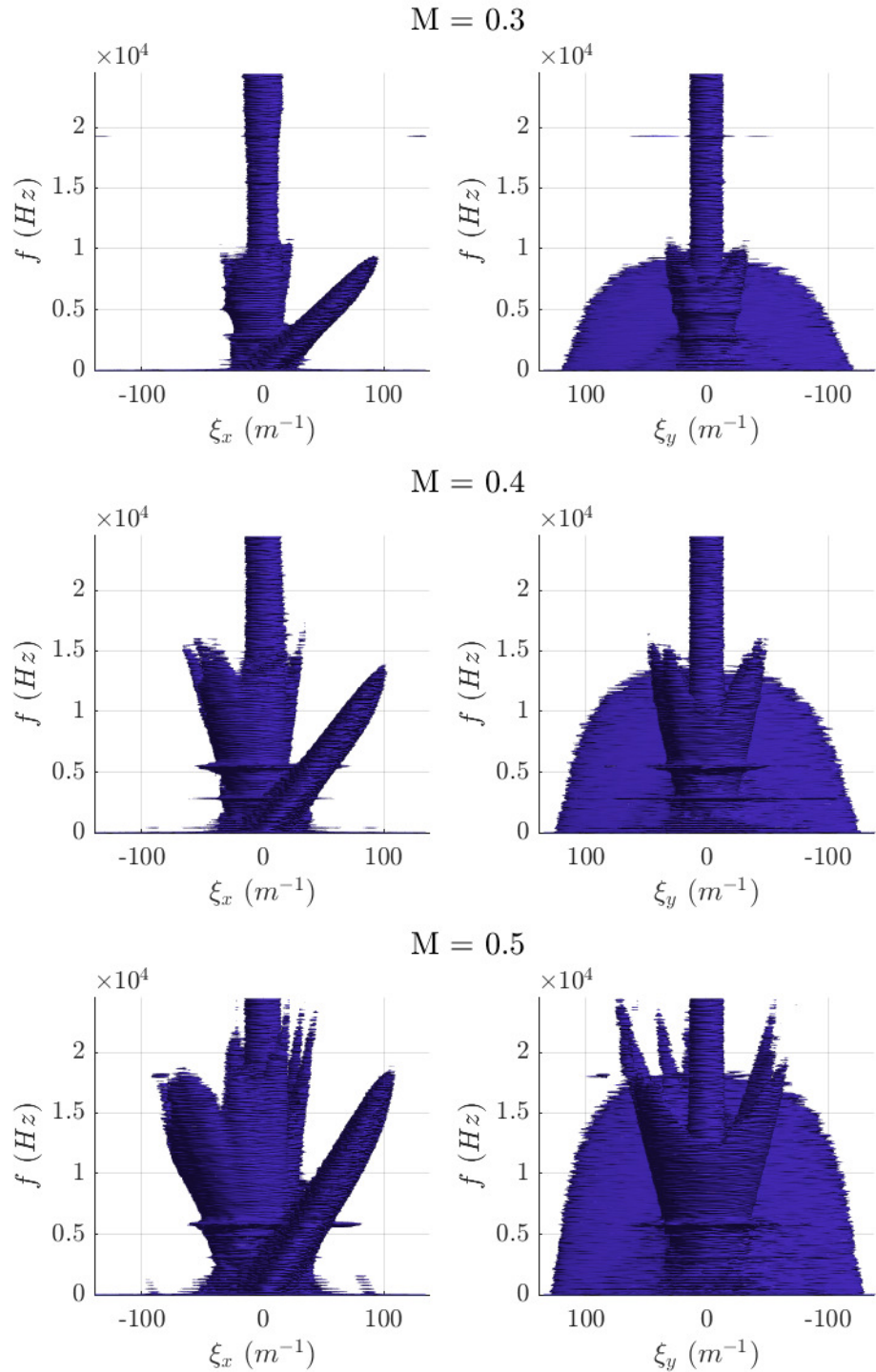


Figure 4.7. Multidimensional spectral estimate isosurfaces as the Mach number increased from 0.3 to 0.5. The isosurfaces are all shown at a power of $10^{-14} \mu m^2/Hz/m^{-2}$.

spatial frequency goes from measuring only the axial component of the optical disturbance to measuring a combination of the axial and span-wise component. This can be seen in Figure 4.8 with the same isosurface value as shown in previous figures and at a Mach number of 0.5. The 90° beam case at the top of Figure 4.8 has been shown previously and the vertical component of the optical disturbance sees little change as the viewing angle is increased except a small reduction in the boundary layer signal and some additional signal at the high temporal frequencies in the acoustic cone. As the angle is increased the side of the acoustic cone traveling in the direction of flow is significantly increased in power, with a large amount of the signal being aliased into the upstream-traveling side appearing as ‘stalactites’ at odd angles. The upstream-traveling acoustic signal is also increased in power but to a lesser extent. The stationary mode pillar experiences some change as well as the viewing angle hits 120° and is stretched in the horizontal direction. As the beam angle increases, the acoustic duct modes begin to overlap one another in spectral space causing significant constructive interference. This will be shown and discussed more fully later in Section 4.4.3. The effective velocity of the optical disturbances is reduced for the disturbances traveling in the same direction as the flow and increased for the disturbances traveling in the opposite direction.

While these three-dimensional isosurfaces offer some significant insight into the overall structure of the various optical disturbances they do not fully show the spectral details. Plots of spatial vs temporal frequencies for the horizontal and vertical plane waves were shown in Figure 4.4 while Figure 4.9 shows slices at various temporal frequencies. The temporal frequencies spectral slices shown are at: 0 Hz, the blade-passing frequency at 517 Hz, the second harmonic of the blade-passing frequency at 1551 Hz, and additional slices at 5, 10, and 20 kHz. The slice at 0 Hz temporal frequency shows the spatial frequencies of the wavefront disturbance that does not change with time. This temporally constant wavefront disturbance is typically called the “mean lensing” component of the wavefront measurement, since it has an effect similar to a lens placed in the beam. The mean lensing slice at 0 Hz shows a mostly axisymmetric pattern with most of its power concentrated at low spatial frequencies. There appear to be the occasional spike radiating out from the center, most noticeably in line with the boundary layer signal.

The next four slices, for $f=517.1$ Hz to 10 kHz, show a vertical line associated with the boundary layers aero-optical disturbance, which progressively moves towards positive x-spatial frequencies with increasing frequency. The boundary-layer disturbance appears to be rotated slightly counter-clockwise indicating that the interrogation beam is slightly rotated between the test section and the wavefront sensor. The boundary layer signals at the lower temporal frequencies appear to have

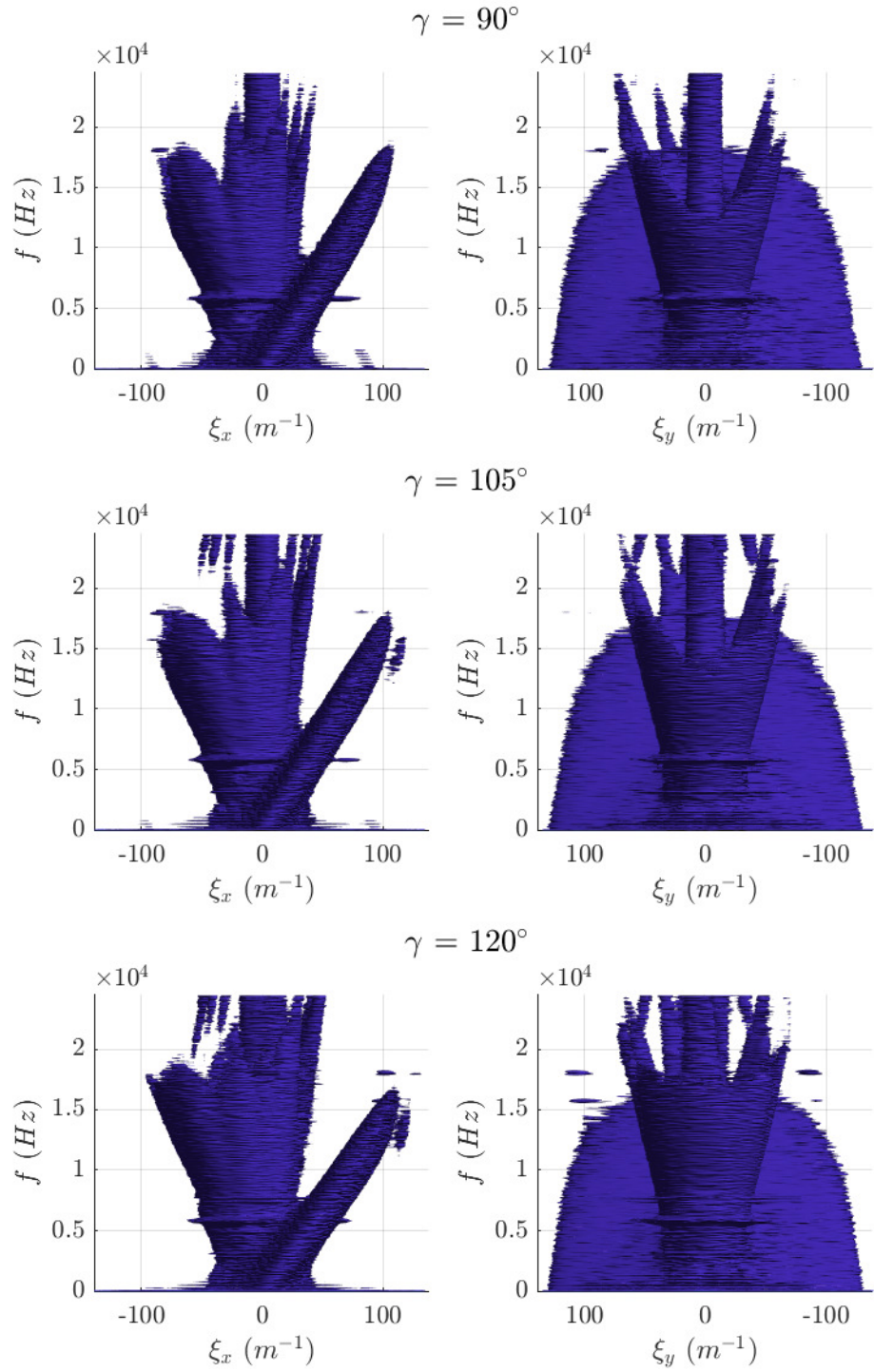


Figure 4.8. Multidimensional spectral estimate isosurfaces of different viewing angles through the test section at a Mach number of 0.5. The isosurfaces are all shown at a power of $10^{-14} \mu\text{m}^2/\text{Hz}/\text{m}^{-2}$.

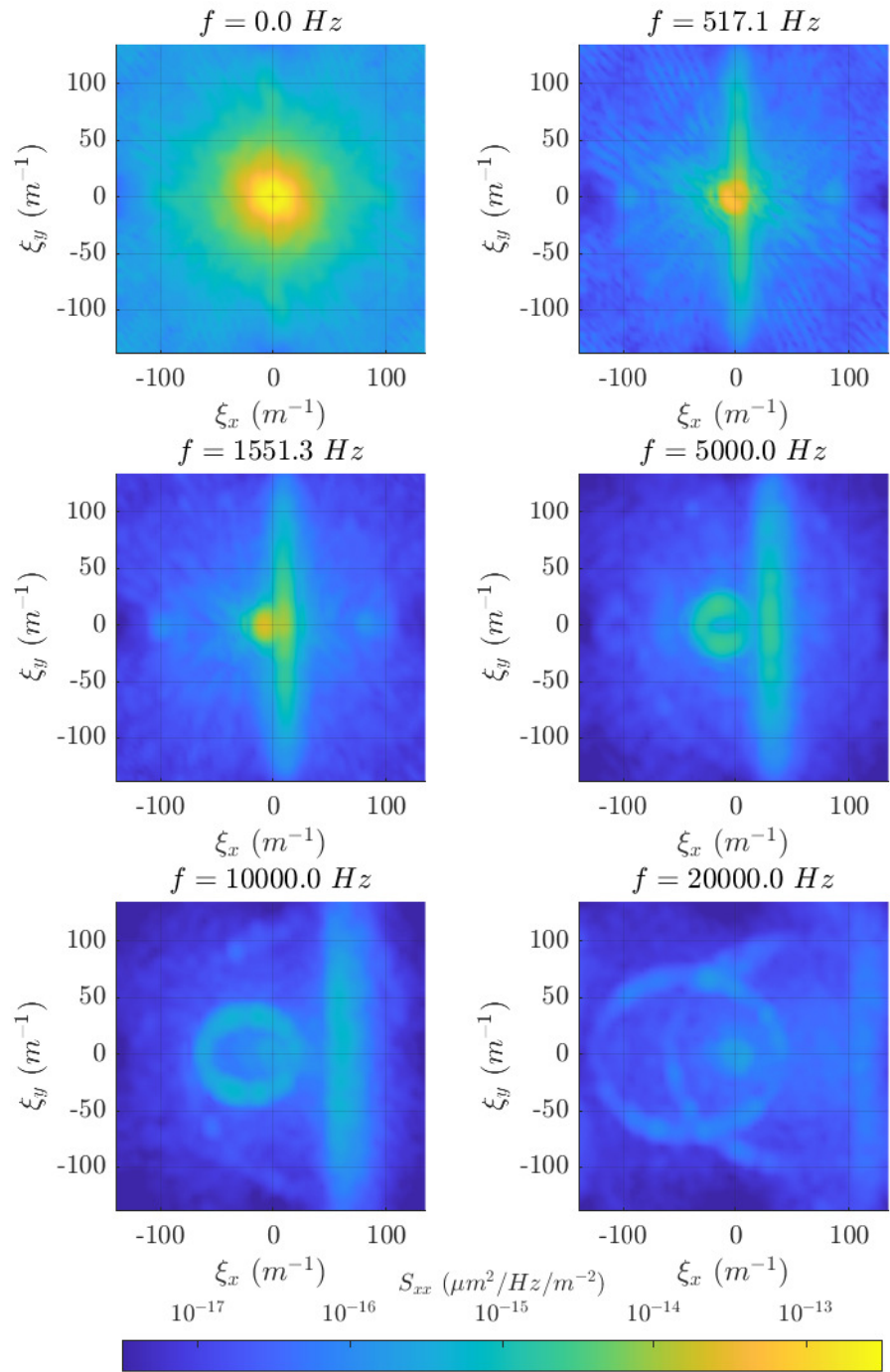


Figure 4.9. Multidimensional spectral estimate slices at various temporal frequencies.

equal decay in both the positive and negative ξ_x directions while at the higher frequencies, the decay is much more gradual in the positive ξ_x direction. This could be indicative of the lower temporal frequency disturbances in the boundary layer typically traveling at a more uniform speed very near the free-stream velocity likely being either in the outer boundary layer or free-stream tunnel turbulence. The higher temporal frequency disturbances seem to have a much wider range of velocities that approach the free-stream velocity and are likely small structures that reside in different parts of the boundary layer and hence travel with a wide range of convection velocities.

The acoustic disturbances show an interesting evolution as the temporal frequency increases. At low temporal frequencies, the acoustic disturbances are concentrated near zero spatial frequency and with strong power. At high temporal frequencies the acoustic disturbances appear as elliptically shaped rings. At 20 kHz, there are two elliptical shapes that are easily identifiable, the smaller one is the signal that is actually present at that frequency while the other one is aliased data due to the limited temporal sample rate. There is constructive interference where the two acoustic rings intersect. The 10 kHz slice also shows a small amount of acoustic aliasing. Both the 10 and 20 kHz acoustic rings show some non-uniform signal power throughout the circumference which are also visible in the three-dimensional views as the spikes at the high temporal frequencies.

4.4.3 Acoustic Cone

The shape of the acoustic cone can be visualized by plotting the relationship between the temporal frequency and the vertical (i.e. cross-stream) and axial (i.e. stream-wise) wavenumbers for a series of acoustic duct modes . Figure 4.10 shows the acoustic cone mode lines for a small set of duct modes at various Mach numbers for a duct that is 1 meter square and a beam passing through the duct at 90° to the flow. The lines here represent the solutions to Equation 2.40 for a series of cross-sectional acoustic modes; essentially, these are $f - \xi_x$ planar “slices” of the cone-shaped acoustic part of the spectrum, at various discrete values of xi_y . The cross-sectional wavenumbers are $k_x = m\pi/l_x$ and $k_y = n\pi/l_y$ with the vertical spatial frequency, $\xi_y = \pm k_y/2\pi$. The horizontal spatial frequency is related to the axial wavenumbers, Equation 2.40, for sound traveling upstream or downstream. Note that there is a 90° rotation between the duct and beam coordinate systems (Equation 3.5).

The plot on the left of Figure 4.10 shows the acoustic cone when $m = 0$ and $n \in [0, 3]$ at Mach numbers of 0, 0.3, and 0.6. Only shown is the positive vertical spatial frequency. As the vertical spatial frequency of a duct-mode varies only with the mode number n each set occupies a distinct

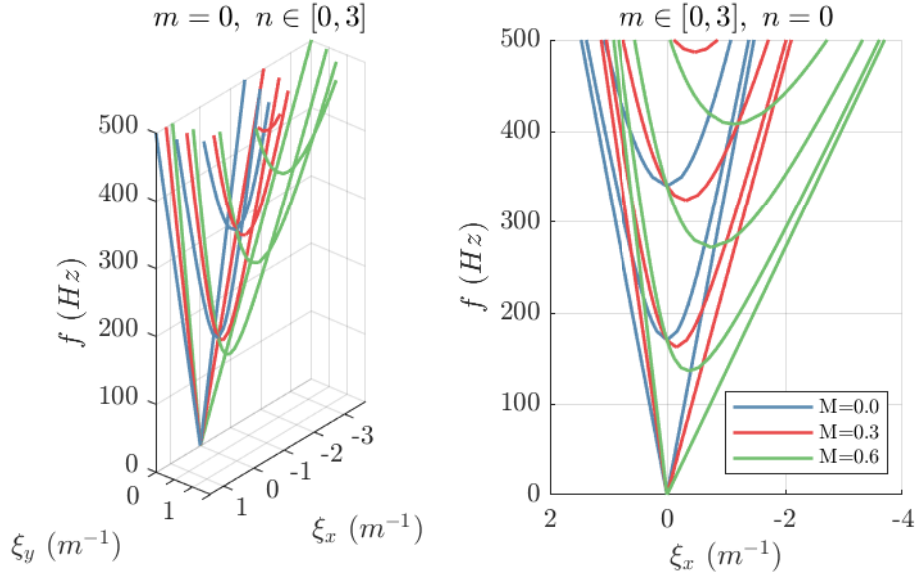


Figure 4.10. Acoustic duct mode lines showing the spatial frequency location as a function of temporal frequency, Mach number, and mode number.

plane, $\xi_y = \pm n/2l_y$. Only acoustic cone modal lines representing the cut-on duct modes are shown.

The plot on the right of Figure 4.10 shows the acoustic modal lines at $\xi_y = 0$ for $n = 0$ which fill the inside of the acoustic cone. The Mach number has a far greater impact on the acoustic cone for the waves traveling upstream. As the Mach number increases, the cut-on frequency (minimum value in f) decreases and the horizontal spatial frequency at the cut-on frequency also decreases. This effect is more pronounced at higher mode numbers. The phase velocity of a downstream-traveling acoustic wave can travel upstream.

It may be possible to individually resolve the separate acoustic duct modes using optical wavefronts if the spatial frequency resolution were high enough. To measure of the vertical mode number, n , the spatial frequency resolution would need to be $\Delta\xi_y \geq 1/2l_y$ for a square duct. With a single beam going through the duct perpendicularly, the axial wave number is directly measurable but its sensitivity is diminished as the temporal frequency is increased. It would be most sensitive to measuring modes that have just been cut-on.

When the optical beam is passing through a duct at an angle other than $\gamma = 90^\circ$ (parallel to the x-axis of the duct), it will measure a combination of the axial wavenumber and the wavenumber

along the x-axis (assuming beam is rotating in the $x - z$ plane of the duct),

$$k_{hm}^+ = k_{zm}^+ \sin(\gamma) - k_x \cos(\gamma) \quad (4.20)$$

and

$$k_{hm}^- = -k_{zm}^- \sin(\gamma) + k_x \cos(\gamma). \quad (4.21)$$

The effective horizontal wavenumber, is related to the spatial frequency via $\xi_x = k_{hm}^\pm / 2\pi$. Figure 4.11 shows the acoustic duct mode lines at Mach number of 0.6 over a range of beam angles. As the beam angle is changed from 90° the node lines for $m \neq 0$ begin to be split at the cut-on frequency with the lines moving outward along ξ_x for angles greater than 90° , while for angles less than 90° , the node lines cross and travel in the opposite direction. This causes some of the node lines to begin to overlap near the sonic lines causing constructive interference among the signals which explains the increase in signal observed on the downstream-traveling acoustic waves as the angle increased in Figure 4.8. As the angle continues to either 0 or 180° the beam is only capable of measuring k_x and k_y with the node lines being parallel to the temporal frequency axis and starting at the cut-on frequency.

4.4.4 Signal Aliasing

In the spectral slices shown in Figure 4.4, when a signal crosses a plane represented by one of the temporal or spatial Nyquist frequencies (positive or negative) it is transposed to the conjugate Nyquist frequency plane and continues on with the same gradient as before. This behavior is illustrated in Figure 4.12 by tiling the base (measured) spectrum, which is shown as the slices of the horizontal moving (stream-wise) disturbances. The thick outline represents the base spectrum, while the thick dashed outline represent the base spectrum in the tiled positions. The tiling process for the spectral slices,

$$S_{xx,T}^{\xi_y=0} = \begin{bmatrix} S_{xx}^{\xi_y=0} & S_{xx}^{\xi_y=0} & S_{xx}^{\xi_y=0} \\ S_{xx}^{\xi_y=0} & S_{xx}^{\xi_y=0} & S_{xx}^{\xi_y=0} \\ S_{xx}^{\xi_y=0} & S_{xx}^{\xi_y=0} & S_{xx}^{\xi_y=0} \end{bmatrix}, \quad (4.22)$$

where $S_{xx}^{\xi_y=0}$ is the base spectral slice showing the horizontal moving disturbances at $\xi_y = 0$ and $S_{xx,T}^{\xi_y=0}$ is the tiled variant. The temporal frequency is tiled,

$$f|_{tiled} = \begin{bmatrix} f - f_s & f & f + f_s \end{bmatrix}, \quad (4.23)$$

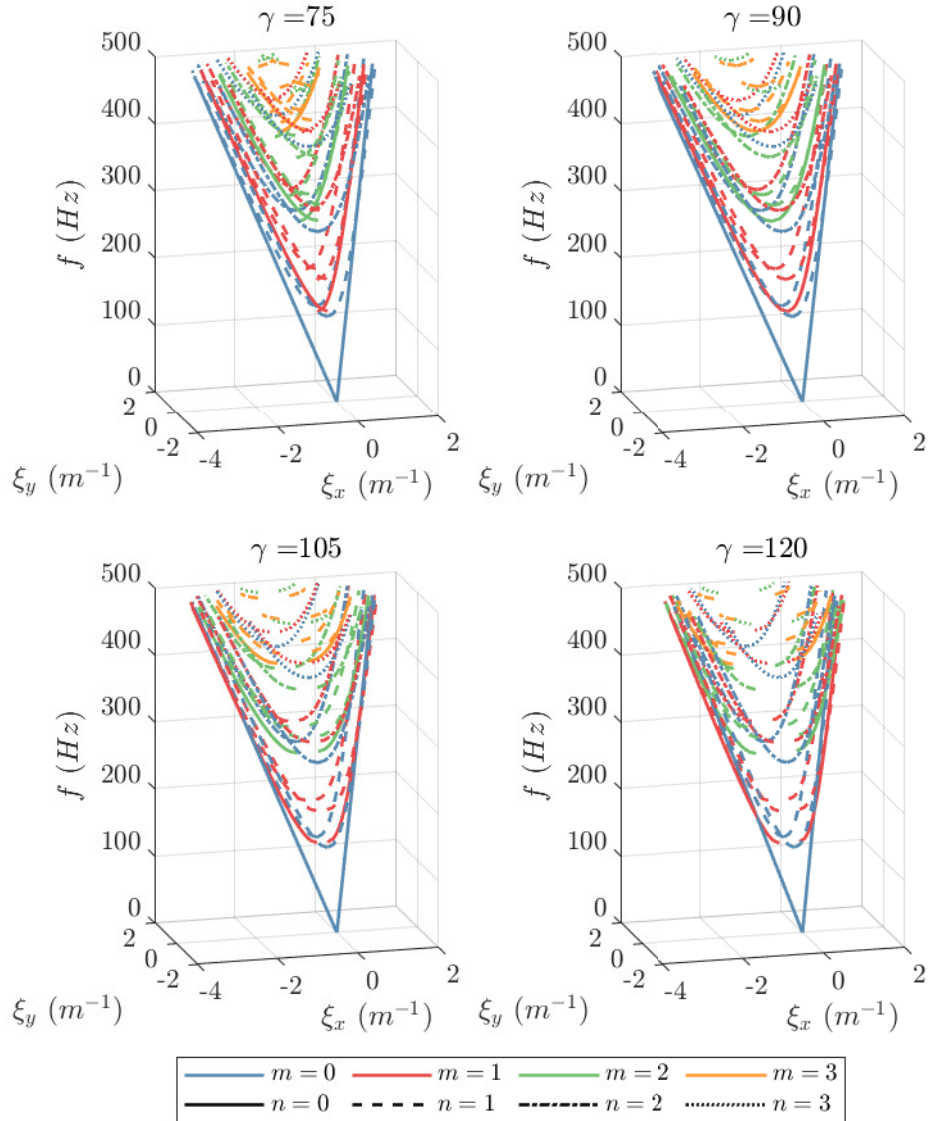


Figure 4.11. Acoustic duct mode lines as a function of viewing angle, γ , at a Mach number of 0.6.

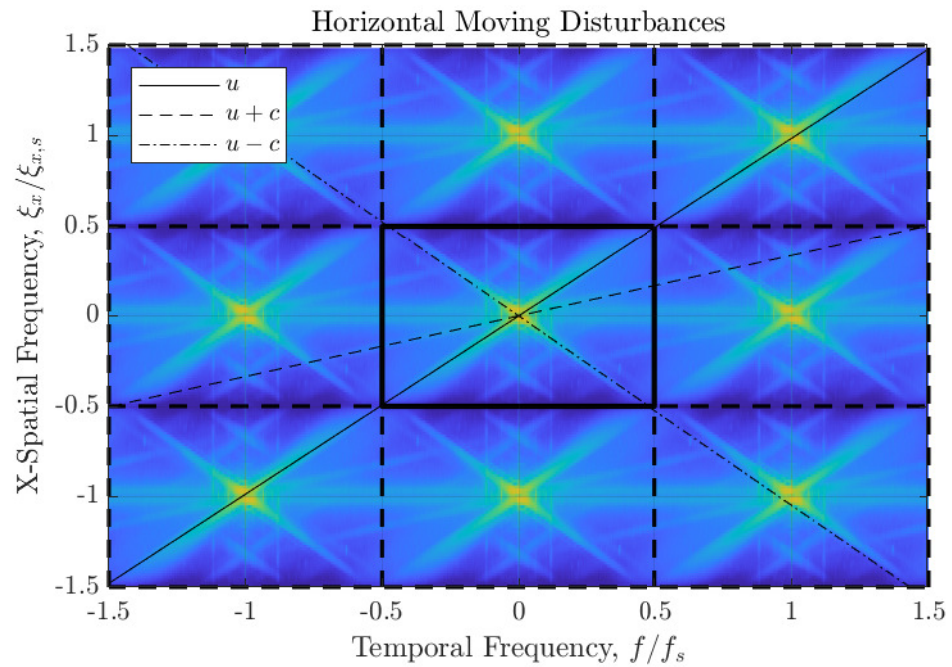


Figure 4.12. Spectrum tiling method to identify aliased data. Shown here as the horizontal moving (stream-wise) disturbance slices, along with lines representing the various characteristic velocities. The thick outline shows the extent of the base spectrum with the thick dashed outlines representing the various tiles of that base spectrum.

where the other frequencies are similarly tiled. This tiling process works because the negative half ($f < 0$) of the spectrum is a duplication of the positive half ($f \geq 0$) of the spectrum. In this research, the spectrum is typically only shown for positive temporal frequencies. The spectral power at any point in frequency space ($\pm f, \pm \xi_x, \pm \xi_y$) will be equal to the conjugate of that point ($\mp f, \mp \xi_x, \mp \xi_y$). This tiling process could be used on the full multidimensional spectrum with the tiling occurring on each axis. While only a three-by-three tiling process was shown, the tiling process in theory needs to be extended to infinity but in practice, with real signals being bandwidth limited, only a finite number of tiles are required. This process has the effect of artificially increasing the sampling rate [38], especially for spectra that are primarily two-dimensional with structures traveling in only one direction (i.e. supersonic boundary-layers).

Figure 4.13 shows a zoomed in portion of the Figure 4.12. The black box again represents the base spectrum along with lines representing the free-stream velocity and the sonic lines. When these characteristic lines are extended past the original sample rate, aliased information becomes more apparent. On the upstream moving disturbance side there is some noticeable aliasing that is present including a significant spike at 18 kHz (-80 m^{-1}) while aliased and about 31 kHz (-200 m^{-1}) when it has been unaliased. As that upstream moving acoustic disturbance crosses the spatial Nyquist frequency, the signal strength drops significantly to local background levels. The boundary layer signal is unfortunately too well aligned with its tiled self for any aliased data to be noticeable. The vertically moving disturbances have some significant temporal aliasing but little to no spatial aliasing.

There maybe some circumstances when aliased data cannot even be identified, such is likely the case for the boundary layer signal shown in the horizontal moving disturbances plot because the signal is directly inline with its aliased self. This may also cause an issue when trying to analyze the original spectrum, particularly at the higher frequencies where the aliased data is sufficiently strong and overlapping the true signal. To avoid this the sample rate velocity,

$$V_s = f/\xi, \quad (4.24)$$

should sufficiently different enough from the disturbance's characteristic velocity. This difference will vary for the depending on the spectral width of the signal. The sample rate velocity of the spectrum in Figure 4.13 is 176.4 m/s, the free-stream velocity is 174.3 m/s and the boundary layer has a significant spectral width to the signal such that it would be difficult to separate the real and aliased signals. The upstream-traveling acoustic wave however is a fairly thin signal that is

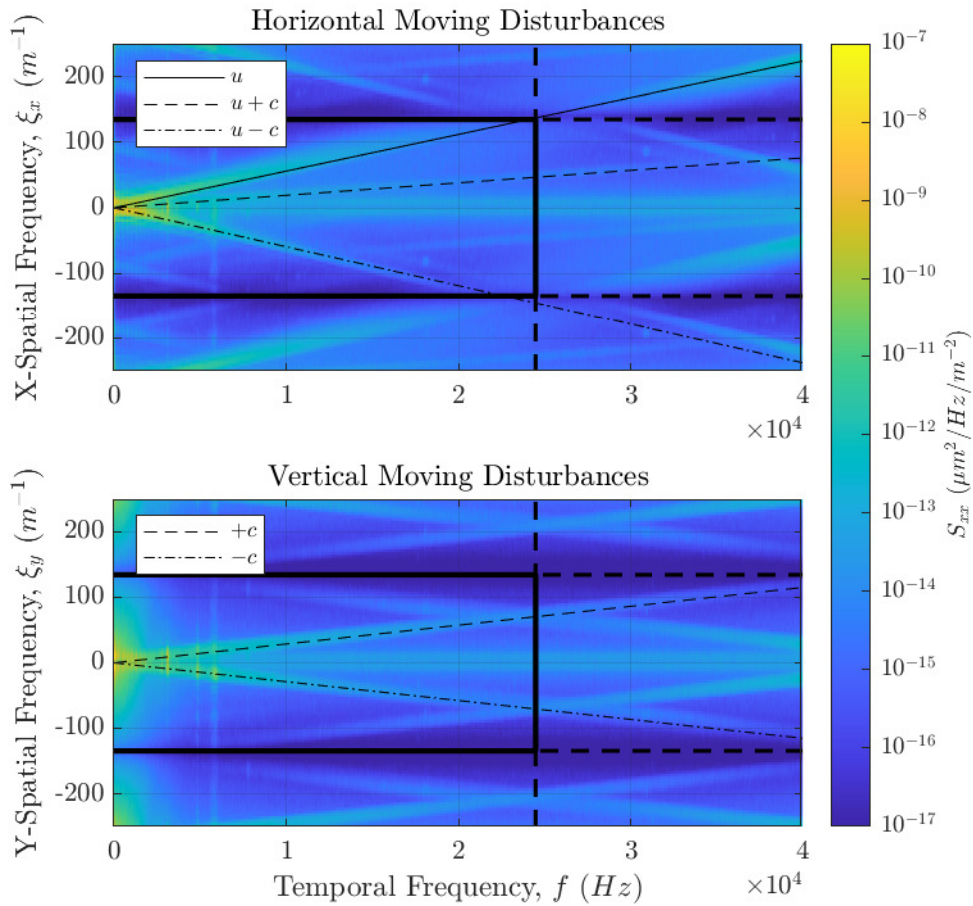


Figure 4.13. Artificially increased temporal sample rate using a dispersion analysis. The black box represents original dispersion plot.

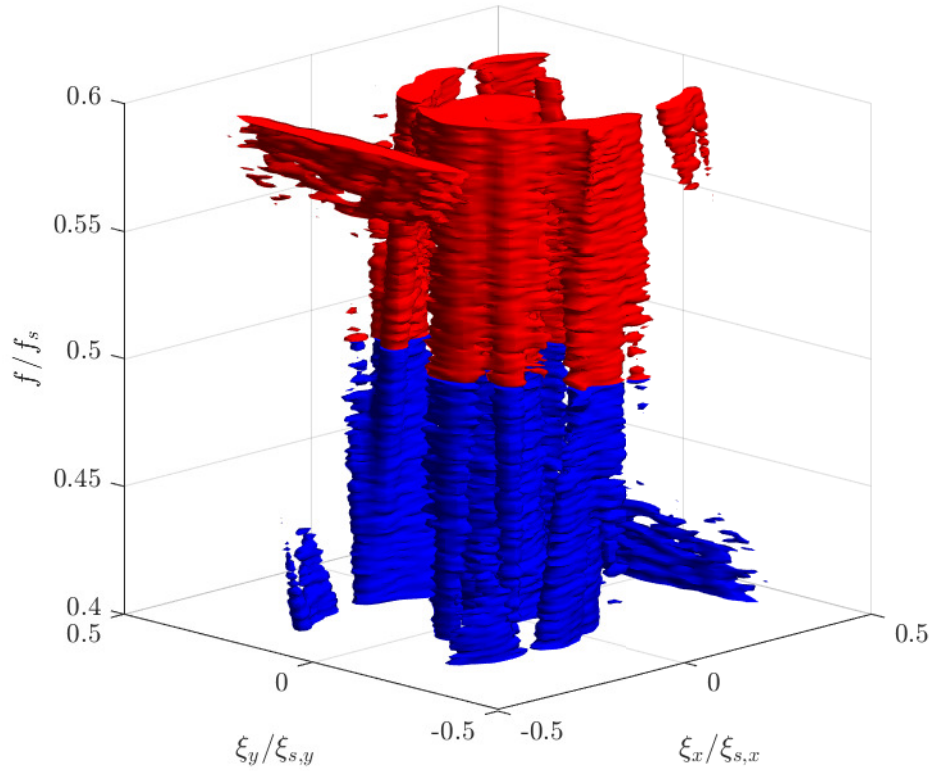


Figure 4.14. Three-dimensional tiling of an isosurface of the spectrum at a power of $10^{-14.5} \mu\text{m}^2/\text{Hz}/\text{m}^{-2}$.

distinguishable from the aliased signal and it has a characteristic velocity of -173.0 m/s.

Figure 4.14 shows a portion of the spectrum that has been tiled three-dimensionally. The power level of the isosurface in this plot is different from those previously shown ($10^{-14.5} \mu\text{m}^2/\text{Hz}/\text{m}^{-2}$). The level for the previous isosurface plots was chosen because it showed minimal signal aliasing. In Figure 4.14 the base spectrum is colored in blue and the tiled portion is shown in red. This plot shows only the portion of the spectrum between 40 and 60% of the temporal sample rate. The acoustic cone is the primary structure in this plot that can be seen to having aliasing present. The ‘stalactites’ that became apparent at higher beam angles are also apparent at this power level and are a continuation from the tiled spectrum above. With spectra that have significant three-dimensional content, this process is most useful for identifying portions of the signal that are aliased. There is future work that can be done in both filtering the aliased data and artificially increasing the sample rate of the wavefront measurement.

4.5 Summary

The use of multidimensional spectral estimation on optical wavefronts can provide significant additional insight to the various components that are being measured, including the desired aero-optical signal but also various forms of noise including sound and vibration. The process of filtering these multidimensional spectra will be discussed in Chapters 6 and 7.

CHAPTER 5

SYNTHETIC WAVEFRONT

In the preceding chapter, the way that wavefront data appears in multidimensional spectra was shown using data acquired in Notre Dame's White Field wind tunnel, for a representative wind-tunnel aero-optical test setup shown in Figure 2.4. The spectra and accompanying discussion showed how individual sources of optical aberration can be identified in the spectra, such as boundary-layer aero-optical signals, acoustic noise sources, mechanical vibration, etc. In following chapters of this dissertation, filtering techniques will be presented for extracting or removing signals or noise sources from wavefront data such as shown in Chapter 3. As a first step towards this objective of developing and examining filtering approaches, this chapter presents methods used to construct a "synthetic" wavefront that contains typical optical and aero-optical signals, which will be used to test and examine different filtering techniques described in Chapter 6.

In order to best understand how some basic filters perform on a set of data, a fully known synthetic wavefront was generated such that all of the various components could be generated separately with the combined product filtered and compared to the synthetic wavefront containing only relevant aero-optical data. This was done by constructing a multidimensional spectrum where each source component was separately generated with parameters that can be modified to alter the output signal as necessary. The resulting multidimensional spectrum could then be used to create the equivalent spatial- and temporally-resolved wavefront signal in the physical domain by inverse Fourier transforming the spectrum.

This synthetic wavefront generation technique produces a qualitative representation that closely matches the measured wavefront but leaves room for improvement in producing a more physically accurate synthetic wavefront. It should be stressed that, although physical models for the spectral behavior are presented for some of the signal components, the shape of the spectrum for each signal component was largely constructed to qualitatively match details observed in the spectra for experimental data such as shown in Chapter 3. This qualitative character to the constructed spectrum for some components should not influence the ability to use the synthesized spectral and wavefront data for examination of filtering approaches, since the constructed data still have the

important behaviors exhibited by measured data.

The synthetic wavefront was generated to approximate the same sampling conditions used to acquire the data first presented in Section 3.4; these sampling conditions are reasonably typical for Shack-Hartmann wavefront measurements at the time of writing. The sample rate was 200 m⁻¹ (i.e. 200 lenslets/m equivalent in the measurement beam) with 64 (2⁶) samples in the spatial dimensions and 30,000 Hz with 8192 (2¹³) samples in the temporal dimension. Figure 5.1 shows the multidimensional spectra estimation of the measured wavefront that was used for the model. The optical wavefront was measured in the University of Notre Dame Whitefield wind tunnel at a Mach number of 0.6 with a 10-inch diameter beam. The beam angle through the test section was 90°.

The signals that were assumed to be statistically independent from one another, such as the boundary layer signal, were converted into dimensional space separately and then summed together, while signals that were assumed to be related to one another, such as the sound and vibration components, were first summed together in frequency space. Figure 5.2 shows the input dispersion plot with each signal component separately colored. The aero-optical signal is shown in red, the stationary modes in blue, duct acoustics in magenta, blade-passing frequency related noise in green, slowly varying mean-lensing in yellow, and background noise in cyan.

5.1 General Spectrum Construction

The general process of developing most of the component signals was to determine an approximate shape, normalize it in the appropriate dimensions, and scale the result by using a function derived from a hyperbola,

$$\frac{\log_{10}(WF) - b}{b^2} - \frac{\xi_{\rho_N}^2}{a^2} = 1, \quad (5.1)$$

such that the signal strength at unity of the normalized radial frequency, $\log_{10}(WF(\xi_{\rho_N} = 1))$, and the limiting slope, a/b , are inputs. This results in the signal strength of the wavefront being

$$\log_{10}(WF) = b - \sqrt{\frac{\xi_{\rho_N}^2}{m^2} + b^2}, \quad (5.2)$$

where

$$b = \frac{1}{2 \log_{10}(WF(\xi_{\rho_N} = 1))} \cdot \left(\log_{10}(WF(\xi_{\rho_N} = 1))^2 - \frac{1}{m^2} \right). \quad (5.3)$$

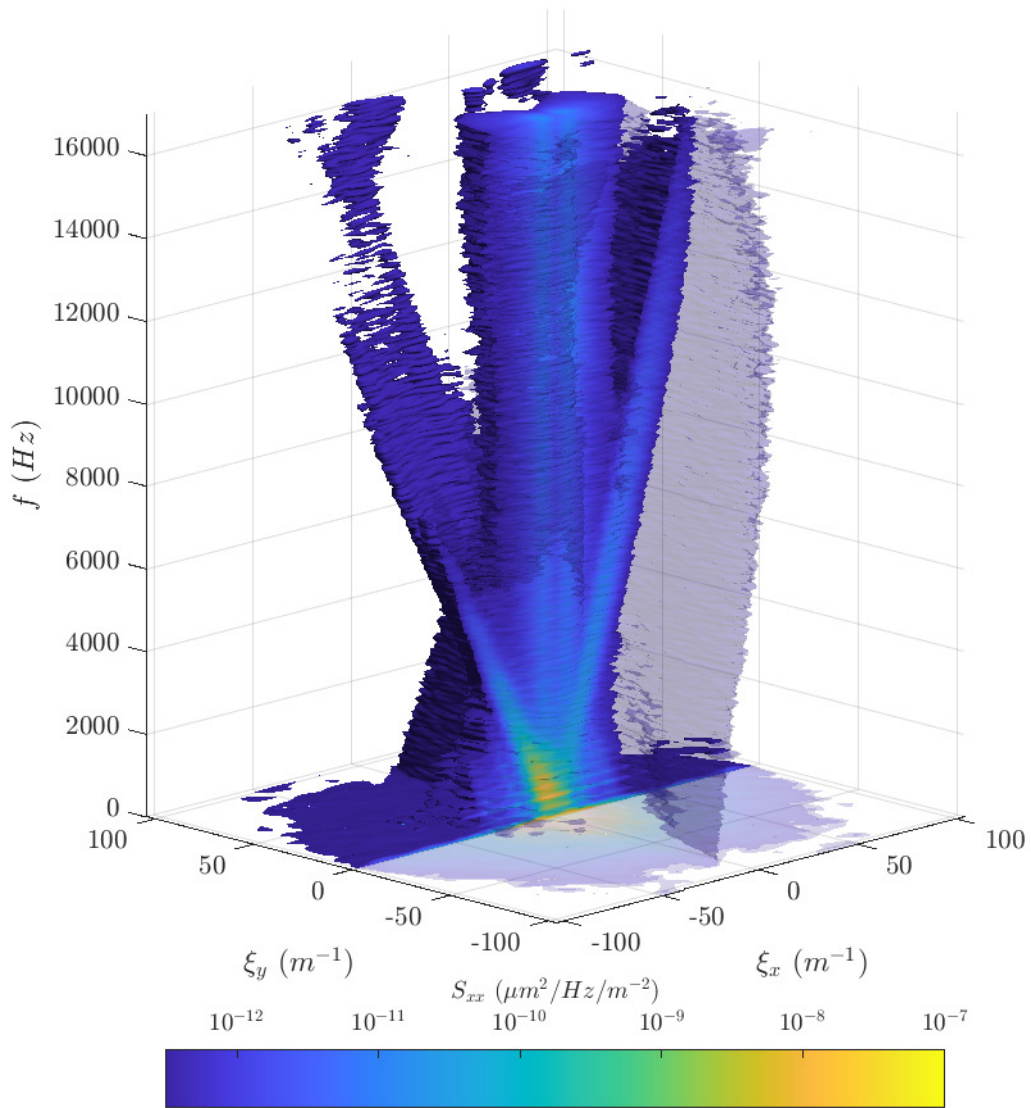


Figure 5.1. Multidimensional spectral estimation that the synthetic wavefront is based on.

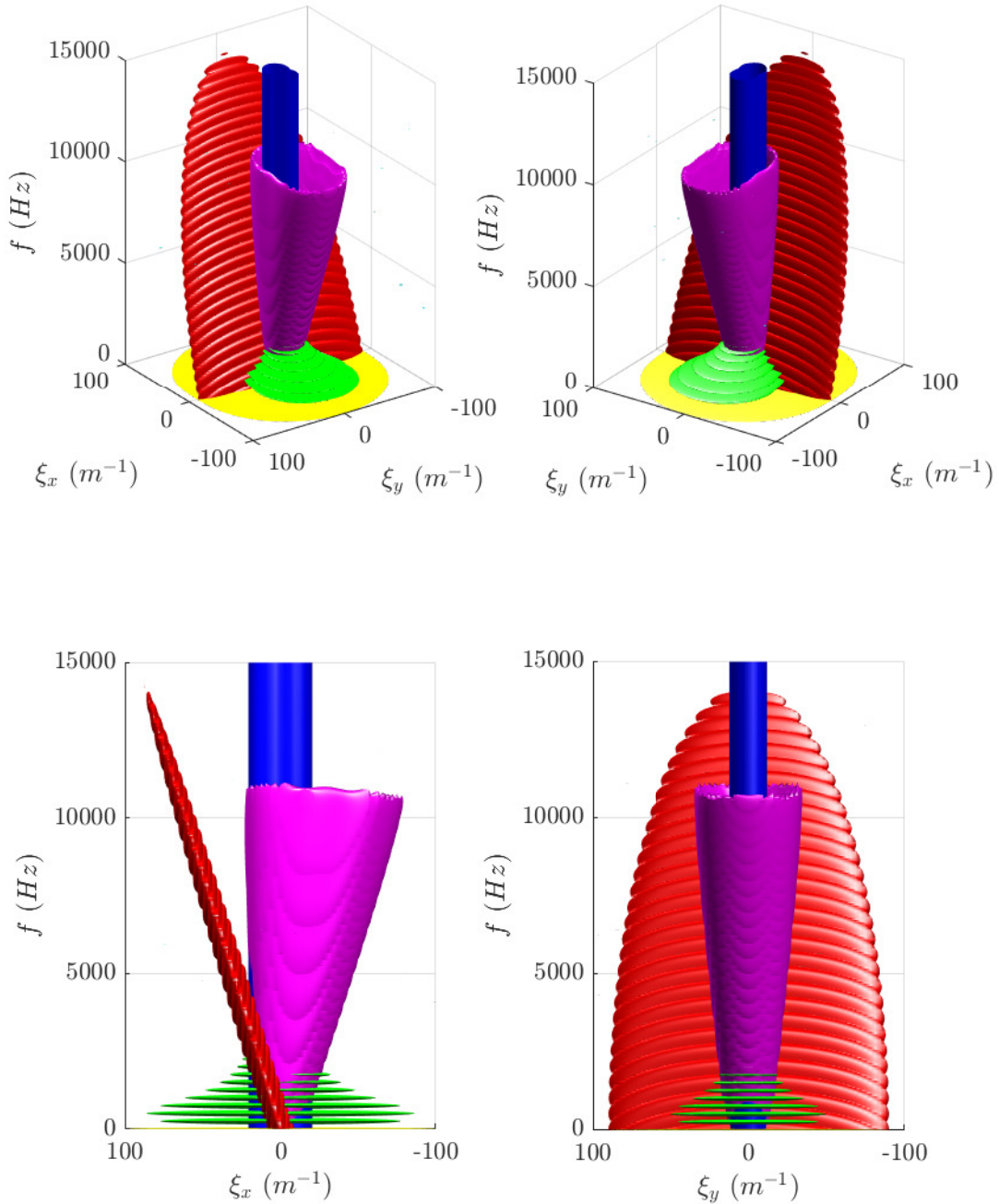


Figure 5.2. Synthetic wavefront input dispersion plot of an aero-optical signal and various signal corruption components. The aero-optical signal is shown in red, the stationary modes in blue, duct acoustics in magenta, blade-passing frequency related corruption in green, slowly varying mean-lensing in yellow, and background in cyan.

TABLE 5.1

VALUES USED IN THE CONSTRUCTION OF THE MULTIDIMENSIONAL
SPECTRUM FOR THE BOUNDARY LAYER SIGNAL

Variable	Value
a_x	8
a_y	90
a_t	175
m	-0.13
u_{BL}	163.2 m/s
$\log_{10}(WF(\xi_{\rho_N} = 1))$	-14.5

5.2 Aero-Optical Signal

The aero-optical signal was generated to approximate an optical beam passing perpendicularly through a test section with boundary layers on each of the test section walls. An ellipsoid was chosen to approximate the boundary-layer signal because it is the simplest shape that best resembles the aero-optical signal in Figure 5.1. This signal was approximated by creating an ellipsoid,

$$\xi_{\rho_N}^2 = (\xi_{x,R}/a_x)^2 + (\xi_{y,R}/a_y)^2 + (f_R/a_t)^2 \quad (5.4)$$

which had been rotated into the plane representing the boundary-layer's dispersion velocity,

$$\begin{bmatrix} \xi_{x,R} \\ \xi_{y,R} \\ f_R \end{bmatrix} = \begin{bmatrix} \cos \theta_u & 0 & \sin \theta_u \\ 0 & 1 & 0 \\ -\sin \theta_u & 0 & \cos \theta_u \end{bmatrix} \begin{bmatrix} \xi_x \\ \xi_y \\ f \end{bmatrix} \quad (5.5)$$

where $\theta_u = \tan^{-1}(-1/u_{BL})$. Equations 5.2 and 5.3 were then used to calculate the multidimensional spectrum of the boundary layer signal. The values used are shown in Table 5.1. In Figure 5.2 the aero-optical signal is shown in red.

TABLE 5.2

VALUES USED IN THE CONSTRUCTION OF THE MULTIDIMENSIONAL
SPECTRUM FOR THE SIGNAL OF THE STATIONARY MODES

Variable	Value
m	-0.175
ξ_{ρ_0}	5
$\log_{10}(WF(\xi_{\rho_N} = 1))$	-14.5

5.3 Stationary Mode Signals

The collection of stationary modes is a temporally constant signal at low spatial frequencies that is often has a cross-section in the plane of spatial-frequencies that is circular. In the particular case that is being modeled, the stationary modes have a cross-section of two circular regions offset along the ξ_x -axis that just overlap one another. A smooth function was chosen to approximate this overlapping circle type stationary mode,

$$\xi_{\rho_N} = \frac{\xi_\rho}{\xi_{\rho_0} \sqrt{10 - 6 \cos(2\xi_\theta + \pi)}}. \quad (5.6)$$

This spectrum for the stationary modes component is shown in blue in Figure 5.2. Table 5.2 shows the values used in generating the spectrum.

5.4 Sound and Vibration Signals

The sound and vibrating component signals are comprised of two parts. The first of these is the blade-passing frequency and its harmonic disturbances (shown in green in Figure 5.2) and the second is the acoustic duct modes (shown in magenta).

5.4.1 Blade-Passing Frequency Disturbance

Like the stationary modes, the blade-passing frequency disturbances were modeled with the same cross-sectional shape as the stationary mode, Equation 5.6, but as narrow-band discs,

$$\xi_{\rho_N}^2 = \frac{\sqrt{\xi_x^2 + (AR\xi_y)^2}}{\xi_{\rho,BPF} \sqrt{10 - 6 \cos(2\xi_\theta + \pi)}} + \left(\frac{f \pm BPFn}{f_T} \right)^2 \quad (5.7)$$

TABLE 5.3

VALUES USED IN THE CONSTRUCTION OF THE MULTIDIMENSIONAL
SPECTRUM FOR THE BLADE-PASSING FREQUENCY DISTURBANCE

Variable	Value
AR	1
BPF	500 Hz
f_c	500 Hz
f_T	100 Hz
m	-0.13
ξ_{ρ_0}	20
$\log_{10}(WF(\xi_{\rho_N} = 1))$	-14

where AR is the aspect ratio of the cross-sectional shape, n is the harmonic number, f_T is the disc thickness, and $\xi_{rho,BPF}$ is

$$\xi_{rho,BPF} = \frac{\xi_{\rho_0}}{\sqrt{1 + \frac{BPFn - BPF}{f_c}}} \quad (5.8)$$

where f_c is the effectively cutoff frequency for modulating the strength of each disc as the harmonic number increased from $n = 0.5$ to $n = 5$ in steps of 0.5. A list of values is shown in Table 5.3.

5.4.2 Acoustic Cone

The acoustic duct mode disturbances form a cone which in the $f - \xi_x$ plane is defined by the lines $u \pm c$, while in the $f - \xi_y$ plane is defined by the speed of sound. At each temporal frequency step an ellipse was defined based on the constraining lines and the distance to that ellipse used to calculate a normalized radial frequency,

$$\xi_{\rho_N}^2 = \frac{\sqrt{(\xi_x - \xi_{x_0})^2 + (\xi_y - \xi_{y_0})^2}}{\sqrt{\xi_{x_a}^2 \cos^2 \xi_\theta + \xi_{y_a}^2 \sin^2 \xi_\theta - 1}} \frac{\sqrt{\xi_{x_a}^2 \cos^2 \xi_\theta + \xi_{y_a}^2 \sin^2 \xi_\theta}}{\xi_{\rho_T}}, \quad (5.9)$$

where ξ_{x_0} and ξ_{y_0} are the midpoint between the sonic lines in the x and y directions as a function of f , ξ_{x_a} and ξ_{y_a} are the distances from the midpoint to the sonic lines as a function of f , and ξ_{ρ_T} is the thickness of the ellipse. The strength of the disturbance was decreased logarithmically as a

TABLE 5.4

VALUES USED IN THE CONSTRUCTION OF THE MULTIDIMENSIONAL
SPECTRUM FOR THE ACOUSTIC CONE DISTURBANCE

Variable	Value
m	-0.3
ξ_{c_x}	115 m^{-1}
ξ_{c_ρ}	200 m^{-1}
ξ_{ρ_T}	8 m^{-1}
$\log_{10}(WF(\xi_{\rho_N} = 1, f = 0))$	-13
$\log_{10}(WF(\xi_{\rho_N} = 1, f = f_s/2))$	-16

function of $|f|$ from $f = 0$ to $f = f_s/2$ with Equation 5.3 becoming,

$$b(f) = \frac{1}{2b_0(f)} \left(b_0^2(f) - \frac{1}{m^2} \right), \quad (5.10)$$

where

$$\begin{aligned} b_0(f) = & \frac{\log_{10}(WF(\xi_{\rho_N} = 1, f = f_s/2)) - \log_{10}(WF(\xi_{\rho_N} = 1, f = 0))}{f_s/2} |f| \\ & + \log_{10}(WF(\xi_{\rho_N} = 1, f = f_0)). \end{aligned} \quad (5.11)$$

Two low-pass spatial filters (more discussion in Chapter 6) were used to replicate some of the signal attenuation that happens at the low spatial frequencies in the x-direction. First a low-pass filter in ρ was used,

$$WF = WF \sqrt{\frac{1}{1 + \left(\frac{\xi_\rho}{\xi_{c_\rho}}\right)^2}}, \quad (5.12)$$

followed by a low-pass filter in the x-direction,

$$WF = WF \sqrt{\frac{1}{1 + \left(\frac{\xi_x}{\xi_{c_x}}\right)^2}}. \quad (5.13)$$

The values used in creating the spectrum are shown in Table 5.4.

TABLE 5.5

VALUES USED IN THE CONSTRUCTION OF THE MULTIDIMENSIONAL
SPECTRUM FOR THE MEAN-LENSING DISTURBANCE

Variable	Value
AR	0.55
f_T	50 Hz
m	-0.5
ξ_{ρ_0}	25
$\log_{10}(WF(\xi_{\rho_N} = 1))$	-14.5

5.5 Mean-Lensing Signal

The mean lensing part of the optical signal is the integrated effect of steady optical aberrations added by lenses, mirror, windows, etc, in the beam path. The aberrations are effectively random and a physical model cannot be developed for them. The mean-lensing signal (shown in yellow in Figure 5.2) uses same cross-sectional as the blade-passing frequency disturbances and represents the slowly varying spatial disturbance,

$$\xi_{\rho_N}^2 = \frac{\sqrt{\xi_x^2 + (AR\xi_y)^2}}{\xi_{\rho_0} \sqrt{10 - 6 \cos(2\xi_\theta + \pi)}} + \left(\frac{f}{f_T}\right)^2. \quad (5.14)$$

Table 5.5 shows a list of the values used in creating this component of the wavefront signal.

5.6 Background Noise Signal

Background noise in the wavefront data originates from sources which are random in nature. The background noise disturbance (with a few small spots shown in cyan in Figure 5.2) was simulated using normally distributed random noise with a mean noise level, $\mu(\log_{10}(WF)) = -18$, and deviation, $\sigma(\log_{10}(WF)) = 0.75$.

5.7 Synthetic Wavefront Creation

A synthetic signal can be created from a power spectrum by solving for x in Equation 4.5 and using the Inverse Fast Fourier Transform,

$$x(t) = \text{REAL} \left[\text{IFFT} \left\{ \sqrt{S_{xx} \cdot N \cdot f_{samp}} \cdot \exp i\phi \right\} \right], \quad (5.15)$$

where **REAL** is the real component and ϕ is a random set of phases for each point in the measurement space. As shown previously this relation can be extended into n -dimensions,

$$f(\mathbf{x}) = \text{REAL} \left[\text{IFFT}_n \left\{ \sqrt{\mathbf{S}_{\mathbf{xx}} \cdot \prod \vec{N} \cdot \vec{f}_{samp}} \cdot \exp i\phi \right\} \right]. \quad (5.16)$$

Care should be taken when constructing the random set of phases, as the zero-frequency component has zero phase, $\phi(0,0,0) = 0$, and the phases on either side of it are conjugates of one another, $\phi(\pm\xi_x, \pm\xi_y, \pm f) = -\phi(\mp\xi_x, \mp\xi_y, \mp f)$.

It was assumed that the aero-optical signal, the stationary modes, the background noise, and the sound and vibration combination of modes were statistically independent of one another and, as such, could be separately transformed into physical space. The components of the sound and vibration sources, the blade-passing frequency, the acoustic cone, and the mean-lensing, were assumed to be related to one another and thus were summed together in frequency space prior to being transformed into physical space. Once the separate components were in physical space the total wavefront was obtained by summing up the separate components with the aero-optical signal saved along side the total wavefront. Some frames from the synthetic wavefront are shown in Figure 5.3 with the total wavefront shown on top and the aero-optical only signal shown on the bottom. Flow is from right to left. The aero-optical signal is noticeable to some degree in the total wavefront signal, but can be overpowered by the various noise sources.

5.8 Comparison to Measured Data

A multidimensional spectral plot of the total synthetic wavefront is shown in Figure 5.4. In this view the aero-optical signal is more noticeable but there still remains some significant overlap with the various noise sources. While the mean-lensing component is not as visible in this isosurface, the rest of the dispersion plot in a good representation of the input dispersion plot shown in Figure 5.2. The blade-passing frequency was depicted as symmetric in the synthetic wavefront while measured

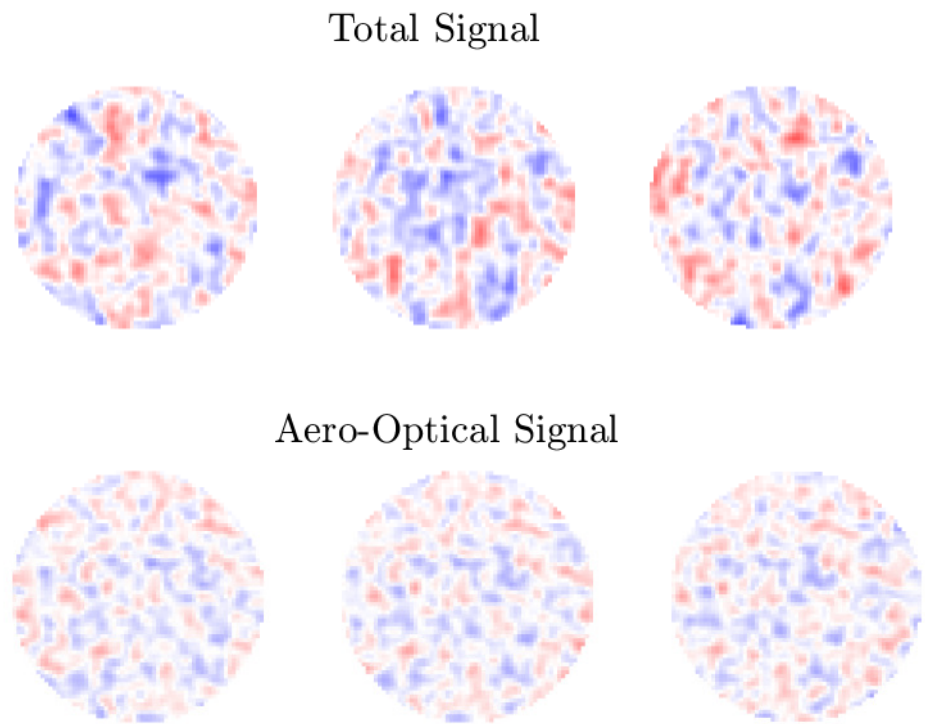


Figure 5.3. Sample frames from the synthetic wavefront with the total wavefront signal on top and the aero-optical only signal bottom. Flow is from right to left.

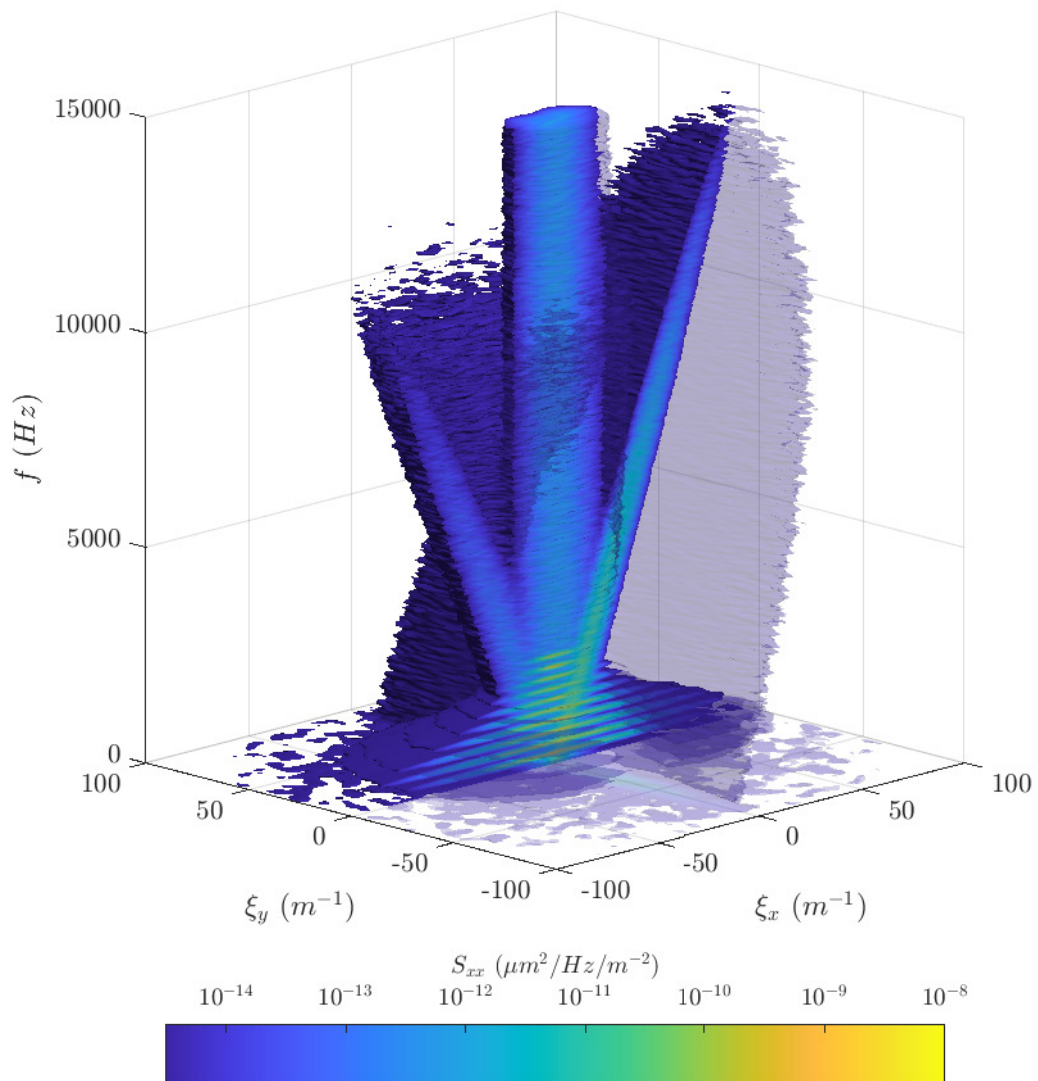


Figure 5.4. Synthetic wavefront output dispersion plot of an aero-optical signal and various signal corruption components.

data (shown in Figure 4.6) shows more signal on the side traveling in the direction of flow. The harmonics of the BPF are more on the upstream traveling side of the dispersion and are a little less pronounced in the measured data. The total synthetic wavefront has a OPD_{RMS} of $0.0112 \pm 0.0006 \mu\text{m}$ with the aero-optical only signal having a OPD_{RMS} of $0.0073 \pm 0.0003 \mu\text{m}$. The measured wavefront presented in Figure 4.6 had a OPD_{RMS} of $0.0874 \pm 0.0263 \mu\text{m}$. The overall OPD_{RMS} of the synthetic wavefront was 12.8% when compared to the measured wavefront indicating that the algorithms used to generate the wavefront are not representative of reality and can provide a future path of research in order to produce more realistic synthetic wavefronts.

CHAPTER 6

WAVEFRONT MULTIDIMENSIONAL SPECTRAL FILTERING TECHNIQUES

This chapter will examine a variety of filtering techniques used on multidimensional spectra of optical wavefronts. While none of the filters presented here are novel, many are based on well known digital filters, their application to filtering optical wavefronts is something that needs to be studied. This chapter will start out by examining some filters that are applied to just the wavefront data itself and will then examine a filtering technique that incorporates additional sensors data in the filtering process.

By using multidimensional spectral estimates on wavefronts, as shown in Chapter 4, differences in source disturbances become clearly evident. When just the wavefront measurement itself is available, digital filters can be used to separate or isolate a single disturbance source or at least minimize the impact from other sources. The digital filters used in this dissertation, use a transfer function, $H(j\omega)$, and are applied in Fourier space. The transfer functions themselves are typically derived in Laplace space, $H(s)$, but because $s = j\omega$ they are valid in Fourier space as well [25]. The transfer function is composed of two components which attenuate the signal, gain and phase. The filter gain is the magnitude of the transfer function, $G(\omega) = |H(j\omega)|$, while the filter phase is the argument, $\Phi(\omega) = \arg(H(j\omega))$. In the simplest case, the filtered signal is the inverse Fourier transform of the gain multiplied by the Fourier transform of the signal,

$$f_F(\mathbf{x}) = \text{REAL}(\text{IFFT}_n[H(j\omega) \text{FFT}_n\{\mathbf{x}\}]), \quad (6.1)$$

where f is the signal function and f_F is the filtered signal.

6.1 Temporal Filter Methods

The methods presented in this section are based on Butterworth filters but could be extended to other types of filters. The square of the transfer function of a Butterworth filter is [9],

$$|H(j\omega)|^2 = G^2(\omega) = \frac{G_0^2}{1 + \left(\frac{j\omega}{j\omega_c}\right)^{\pm 2n}}, \quad (6.2)$$

where G_0 is the zero-frequency gain, ω_c is the cutoff angular frequency, n is the filter order (number of filters in a series), and \pm represents either a low-pass (+) or high-pass (-) filter. The gain of this filter is

$$G(\omega) = \frac{G_0}{\sqrt{1 + \left(\frac{\omega}{\omega_c}\right)^{\pm 2n}}}. \quad (6.3)$$

A band-pass filter can be constructed by placing a low-pass filter in series with a high-pass filter and a band-stop by placing the two types in parallel.

In many tests, a large portion of the wavefront noise is at low frequencies primarily caused by mechanical vibration. In general, a high-pass filter is useful in temporal space for removing this noise, since in many cases most of the power in the aero-optical signal occurs at higher frequency than the low-frequency mechanical vibration, as shown in Figure 6.1. The top plot in this figure shows the high-pass filtered OPD_{RMS} of both the total and aero-optical only wavefronts normalized by the unfiltered OPD_{RMS} of the aero-optical only wavefront, for high-pass filters with various cutoff frequencies. The results in Figure 6.1 were computed using wavefronts that were simulated using the methods described in Chapter 5. For reference, the bottom plot of Figure 6.1 shows the power spectra of just the aero-optical portion of the wavefront (red curve) and the total wavefront (blue curve) which includes vibration-related peaks associated with the blade-passing frequency and its harmonics. The figure shows how a high-pass filter decreases the energy in the total wavefront and in the actual aero-optical wavefront, as the filter cutoff frequency increases. As shown in the top plot, at low cutoff frequency, the filter primarily removes vibration effects from the total signal; however, as the cutoff frequency increases, the filter also removes actual aero-optical signal. At around 1200 Hz, the OPD_{RMS} of the total signal is equal to the OPD_{RMS} of the actual aero-optical signal; at this cutoff frequency 75% of the aero-optical signal remains and the remaining signal is made up by the remaining contamination. This approach can provide a computationally inexpensive way of estimating the aero-optical portion of the wavefront for calculations that rely on the OPD_{RMS} of a wavefront. While it is more straightforward to determine a cutoff frequency for this synthetic

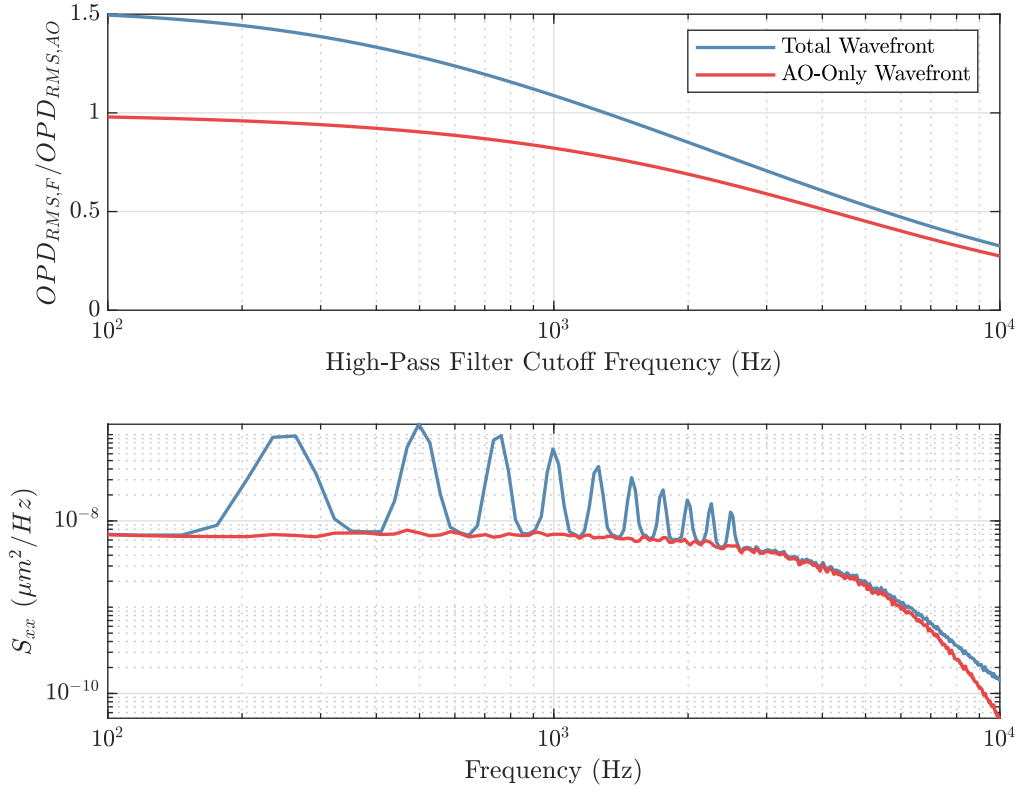


Figure 6.1. The *opdrms* of high-pass temporal filtered wavefronts relative to the *opdrms* of the aero-optical only unfiltered wavefront (top). Power spectra of both of the simulated wavefront versions (bottom).

wavefront since all of the signal components are fully known, a measured wavefront will likely take some knowledge or expectation of the contamination that is present in the measurement in order to select a high-pass filter cutoff frequency.

An example of wavefronts that result from band-pass and band-stop filtering is shown in Figure 6.2. The figure shows several wavefront frames of measured data acquired in the Notre Dame White Field wind tunnel and presented previously in Chapter 3 (see Figure 3.16) that are band-stop filtered in the left column and band-pass filtered in the right column. The flow is from right-to-left and the band-pass filtered wavefront clearly shows upstream-moving optical disturbances (moving left-to-right against the flow direction) associated with acoustic duct modes traveling upstream from the fan. On the other hand, the band-stop filtered wavefronts on the left of Figure 6.2 show much slower-moving optical disturbances that are in general moving in the direction of the flow. In particular, the downstream-moving disturbances on the left side of Figure 6.2 have the appearance of boundary-layer aero-optical disturbances, with a scale on the order of the boundary-layer thickness.

Note that for filters that operate in one dimension, the filters were applied over both positive and negative frequencies to the n-dimensional Fourier transform in order to preserve the direction of travel of the signal. This also allowed several filters to be applied in series without having to perform a Fourier and inverse Fourier transform for each successive filter. Temporal filters are also used in sizing and/or designing adaptive optics systems [24] for example. A low-pass filter with a cutoff at the bandwidth of either a fast-steering or deformable mirror is often used to define the signal that the system needs to reject [63]. A control system may need to have the bandwidth reduced in order to keep a mirror's travel within limits [39], while a high-pass filter would inform designers of the remaining optical aberrations that cannot be corrected.

6.2 Upstream/Downstream Moving

In the preceding section, filters based on temporal frequency only were discussed. In this section, another filtering approach is presented in which signals are identified based on their dispersion velocity. For the filtering of upstream and downstream moving optical disturbances a logistic function was chosen,

$$f(x) = \frac{1}{1 + \exp\{-kx\}}. \quad (6.4)$$

This function was then expanded into two-dimensions (x and t). For a filter that removes disturbances moving against the direction of flow, the filter should ideally return a value of one in both the first and third quadrants and zero otherwise when plotted in a graph of temporal versus spatial

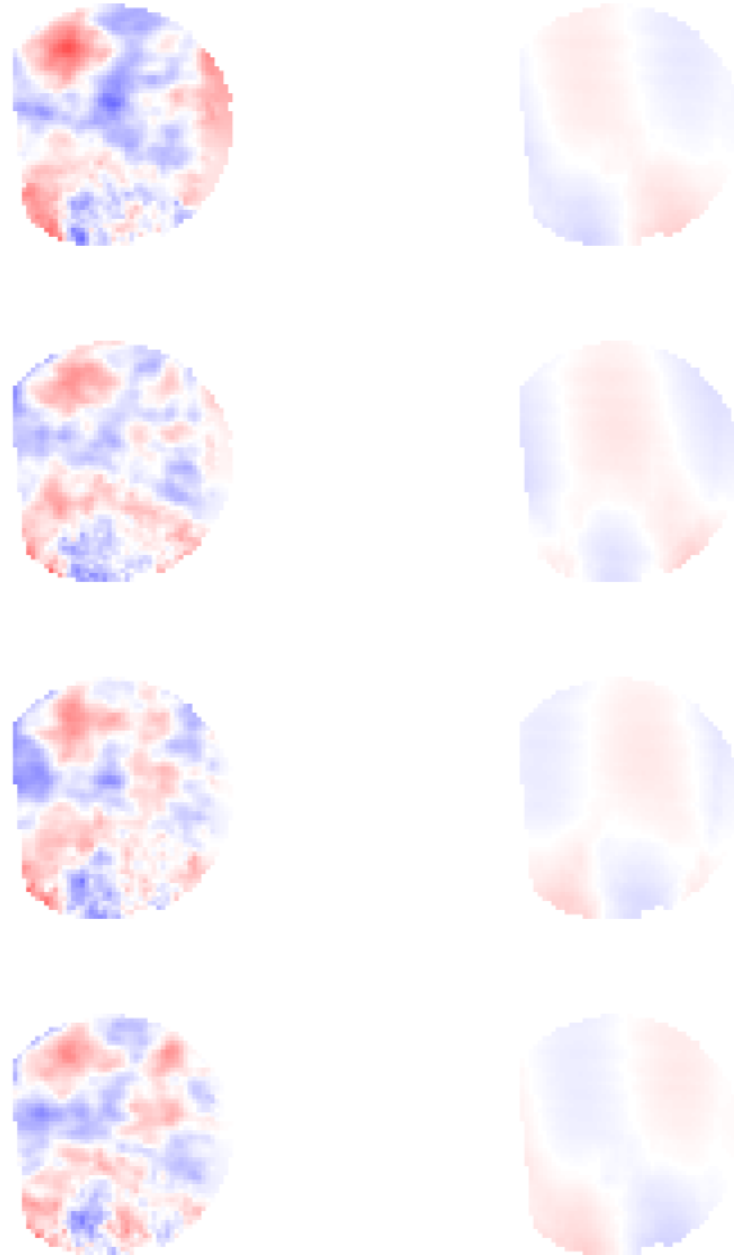


Figure 6.2. Measured wavefronts filtered at the blade-passing frequency (532 ± 10 Hz).
The left column is band-stop filtered while the right is band-pass filtered.

frequency. To accomplish this, the logistic curve in each dimension was scaled and offset to output values between negative one and positive one,

$$G_t(f) = \frac{2}{1 + \exp\{-k_t f\}} - 1 \quad (6.5)$$

and

$$G_x(\xi_x) = \frac{2}{1 + \exp\{\pm k_x \xi_x\}} - 1, \quad (6.6)$$

where \pm determines whether the filter is designed to act on upstream-traveling disturbances (+) or downstream-traveling (-). These two gain functions are then multiplied together and scaled to output values between zero and one,

$$G(\xi_x, f) = \frac{(G_t \cdot G_x) + 1}{2}. \quad (6.7)$$

As the values of k_x and k_t go to infinity an ideal filter is obtained. In a plot of the gain with the horizontal spatial frequency on the x-axis and the temporal frequency on the y-axis, an ideal filter for obtaining only the downstream traveling disturbances would have a gain of one in the first and third quadrants, zero in the second and fourth quadrants, and a value of 1/2 when either frequency is zero. The value of 1/2 would equally split the component of a disturbance that is neither traveling upstream or downstream between the two directions.

The multidimensional spectrum using an ideal upstream-moving moving filter on the synthetic wavefront is shown in Figure 6.3 alongside the spectrum of the unfiltered wavefront. All of the upstream traveling disturbances are removed and the disturbances at the stream-wise spatial frequency $\xi_x = 0 \text{ m}^{-1}$ are significantly reduced. Some of the stationary modes (the vertical cylinder along $\xi_x = 0$ and $\xi_y = 0$) remain while only the acoustic and vibration signals that are propagating in the direction of flow remain. The aero-optical signal from the boundary layer is clipped slightly at $\xi_x = 0$ due to the spatial width of the signal. The ratio of the time-averaged spatial-RMS of the filtered signal when compared to the aero-optical only signal was 1.24 while the unfiltered ratio was 1.53. When the filter was applied to the wavefront with only the aero-optical boundary layer signal present the OPD_{RMS} was reduced to 96% that of the unfiltered wavefront, showing that the filter does not reduce the energy of aero-optical signals convecting with the flow. Hence, this filter method will retain any disturbance that is traveling in the direction of flow. Even with an ideal filter there is some slight attenuation of the aero-optical signal due to signal having some spectral width that crosses into upstream-moving portion of the dispersion plot.

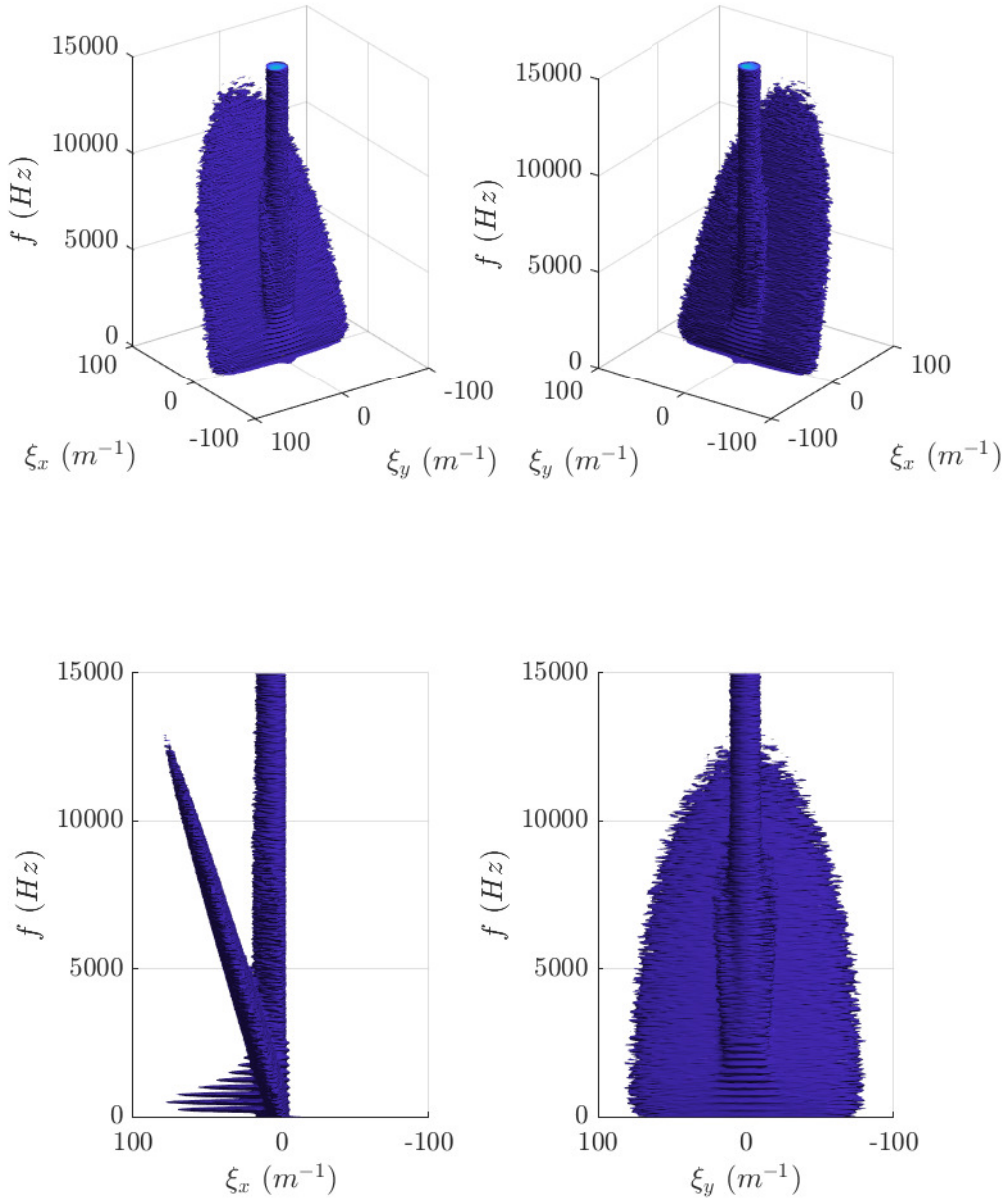


Figure 6.3. Multidimensional spectral isosurface of the synthetic wavefront with a downstream filter in place.

6.3 Velocity Filtering

For a nondispersive medium such as air, flow structures traveling at a given speed have a constant slope on a multidimensional spectral plot. A plane in the multidimensional spectral plot can therefore be used to measure a flow structure's velocity in both x and y -directions. The distance from any given point in the multidimensional spectral space to a plane described by the velocities u_x and u_y can be computed by

$$d = \frac{|u_x \xi_x + u_y \xi_y - f|}{\sqrt{u_x^2 + u_y^2 + 1}}. \quad (6.8)$$

Equation 6.8 above can therefore be used to construct a low-pass or high-pass filter that retains only disturbances that are traveling at that velocity, or to exclude those disturbances,

$$G(d) = \frac{1}{\sqrt{1 + \left(\frac{d}{d_c}\right)^{\pm 2n}}}. \quad (6.9)$$

where d_c is the cutoff distance from the plane defined by the velocities u_x and u_y . Because of differences in the temporal and spatial sample rates of several orders of magnitude, the filter function employed in this research used frequencies that have been normalized by the sample rate.

An example of a low-pass velocity-filter applied to the synthetic wavefront generated in Chapter 5 is shown in Figure 6.4. The filter was constructed for a u_x set at the mean boundary-layer velocity, and u_y set to zero. The values of the other two filter parameters were selected as $d_c = 1/80$, and $n = 1$, which were chosen in a trial-and-error process in which values were chosen, the filtered multidimensional spectrum was computed, and refinements to the parameter values were made based on how well the filtered spectrum captured just the boundary-layer signal. Figure 6.4 shows that, using these filter parameters, the velocity-filtered multidimensional spectrum successfully retains primarily only the aero-optical signal with some additional low-frequency content from the blade-passing frequency and harmonic disturbances as well as some stationary and acoustic disturbances. The ratio of the OPD_{RMS} relative to that of the aero-optical-only signal went from 1.53 in the unfiltered case to 1.01 in the filtered case, showing that the velocity filter has filtered out a substantial amount of noise and other unrelated signals from the aero-optical signal of the boundary layer, which is presumed to be the objective of the measurement. As such, this method can provide a very effective way to quickly estimate the OPD_{RMS} of a convecting aero-optical disturbance in a noise-contaminated wavefront.

Another use of the velocity filter is measuring the speed of a broadband convecting disturbance

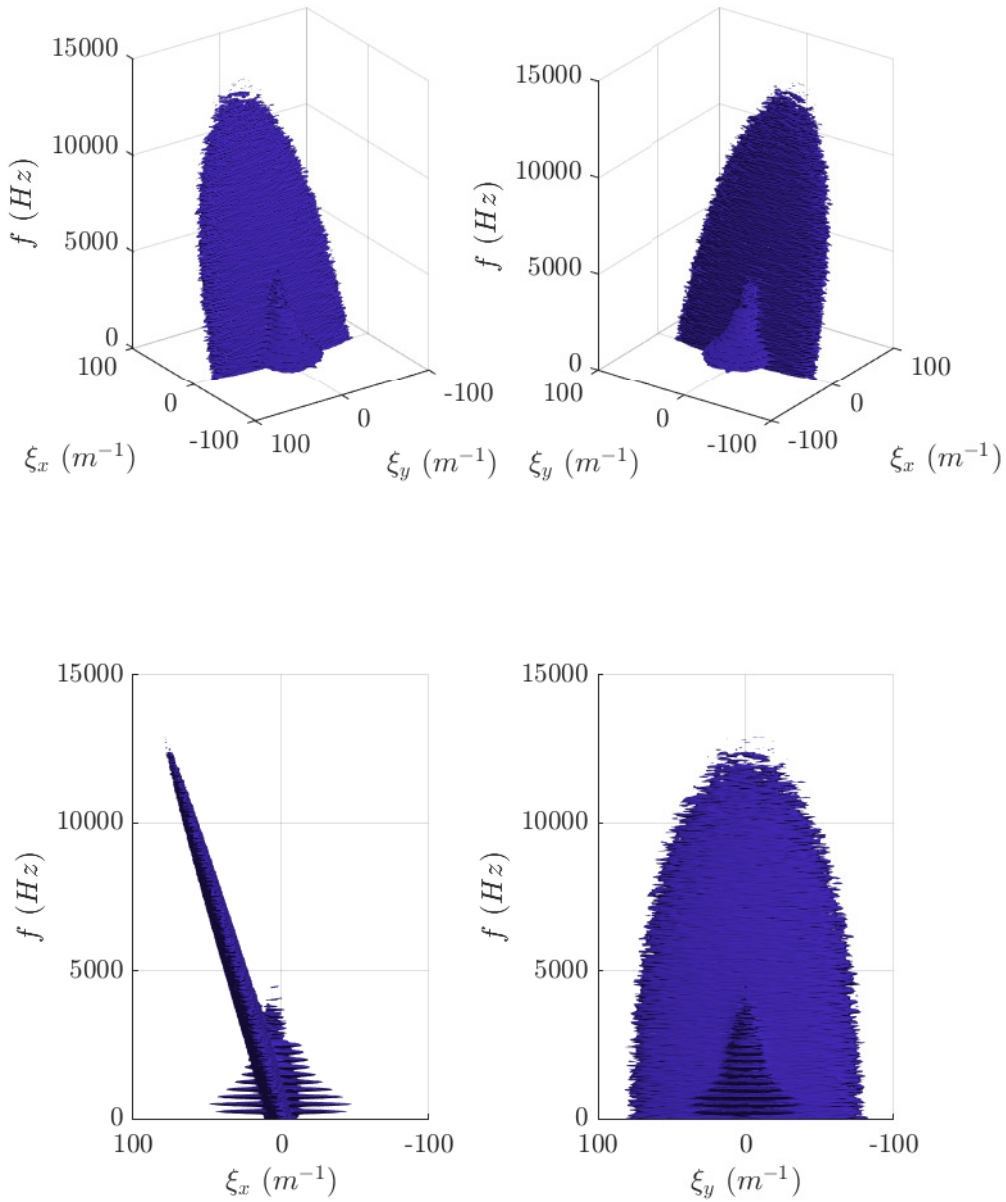


Figure 6.4. Multidimensional spectral isosurface of the synthetic wavefront with a low-pass velocity-filter in place.

such as the aero-optical signal of a boundary layer. This can be accomplished by applying a series of low-pass velocity filters to the multidimensional spectrum of the wavefront along with a high-pass radial frequency filter to remove a significant portion of the stationary modes and acoustic cone,

$$S_{xx,f}(\xi_x, \xi_y, f) = S_{xx}(\xi_x, \xi_y, f) G_v^2 G_\rho^2, \quad (6.10)$$

where G_v is the velocity filter and G_ρ is the radial frequency ($\xi_r h o^2 = \xi_x^2 + \xi_y^2$) filter. Once the wavefront has been filtered in multidimensional spectral space, the total power remaining in the filtered spectrum can be calculated,

$$P = \sum (S_{xx,f} \prod \vec{f}_s). \quad (6.11)$$

The average convective velocity of the structure is then given by the filter parameters that produce the maximum power in the filtered signal.

This velocity finding procedure described in the preceding paragraph was tested on the synthetic wavefront generated in Chapter 5, which had a known boundary-layer mean velocity. The results of the velocity finding analysis are shown in Figure 6.5, which shows the power in the filtered signal as a function of the u_x parameter using in the velocity filter component of Equation 6.10. The low-pass velocity filter used the same parameters as used previously except that u_x was varied and the high-pass radial frequency filter used a cutoff value of 0.1 with an order of $n = 2$. The radial frequency, ξ_ρ , was normalized by the spatial sampling rate. In this case, the boundary layer speed was determined to be 163 m/s which corresponds to the design velocity of the synthetic signal of $0.8U$. For signals where the mean-velocity component of the aero-optical signal is not aligned with either the horizontal or vertical axis, both velocity components can be varied in the velocity filter. This produces a three-dimensional surface of filtered signal power as a function of u_x and u_y in the velocity filter, where the velocity components of the moving signal are given by the maximum power of the surface. An example of this method is shown in Figure 6.6, which was computed using experimental wavefront data acquired in the White Field wind tunnel at $M=0.5$. In this case the same filtering parameters were used as the synthetic case except the distance cutoff was $d_c = 1/40$ and both u_x and u_y were variables. The velocity components of the boundary-layer optical disturbances determined from Figure 6.6 are 152 m/s in the x-direction and 3 m/s in the y-direction. This boundary-layer velocity is approximately 0.85 times the freestream velocity when compared to the pitot probe measurement of the free-stream velocity, which is very close to the

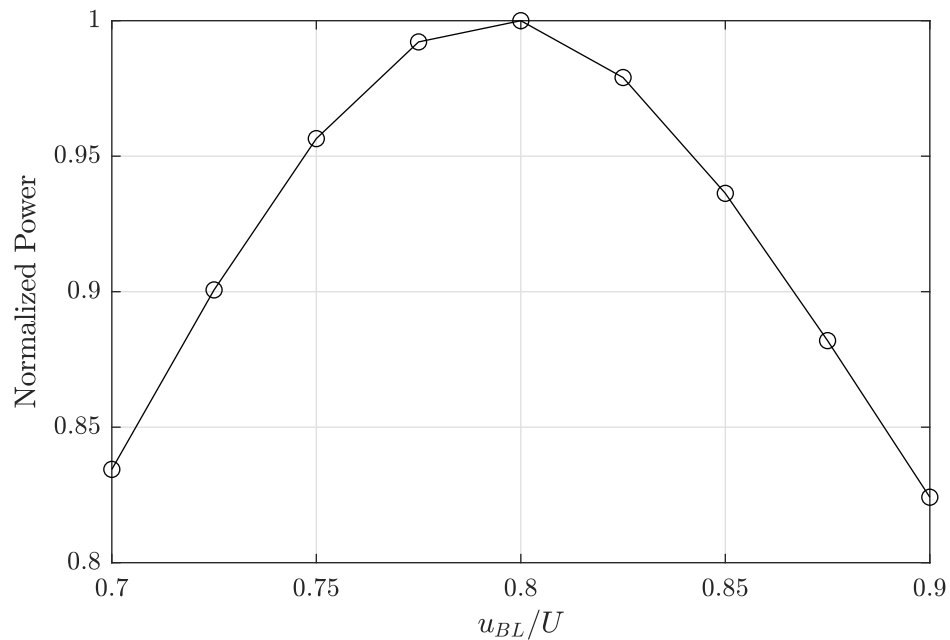


Figure 6.5. Boundary layer velocity measurement of the synthetic wavefront using a combination of a low-pass velocity filter and a high-pass radial frequency filter. The maximum value at $u_{BL}/U = 0.8$ corresponds with the actual value used in the creation of the synthetic wavefront.

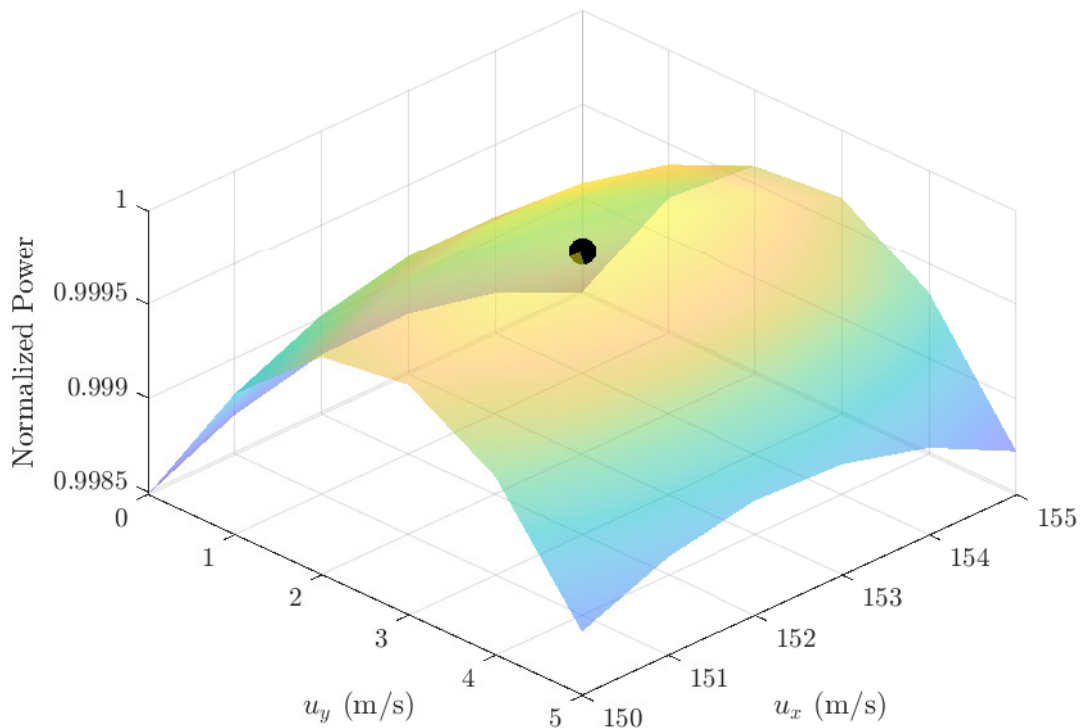


Figure 6.6. Velocity low-pass filter used to determine the mean disturbance velocity of measured data presented in Figure 4.6. The velocity in the x-direction was measured to be 152 m/s and 3 m/s in the y-direction.

accepted speed of the optically-aberrating structures in a boundary-layer flow [23]. The overall flow angle of the boundary-layer with respect to the orientation of the measurement beam was approximately 1.1°.

6.4 Baseline Spectrum

If all of the narrow-band temporal signals in a data set can be assumed to be measurement contamination that needs to be filtered out, a method for calculating the baseline of the spectrum provides a simple way of filtering a portion of the signal contamination. For example, during analysis of Raman spectra, the baseline spectra must often be removed [55]. This task is often performed manually which has resulted in a number of attempts to create automated techniques to estimate the baseline spectra [44, 54, 55, 65]. One of those techniques [55], a small-window moving-average based, fully automated baseline estimation method was used in this research. For this method, at each spatial frequency location, the baseline spectrum was computed along the temporal axis. This process estimates the baseline spectrum, \mathbf{b} , from the measured spectrum, \mathbf{m} ,

$$\mathbf{m} = (\mathbf{b} + \mathbf{x}) * \mathbf{p} + \mathbf{n} = \mathbf{b} * \mathbf{p} + \mathbf{x} * \mathbf{p} + \mathbf{n}, \quad (6.12)$$

where \mathbf{x} is a pure or underlying signal vector, \mathbf{p} is an instrumental blurring function, \mathbf{n} is measurement noise, and $*$ is convolution operator.

Figure 6.7, shows the multidimensional spectrum of an unfiltered measurement (top left) and its estimated baseline spectrum (top right). The bottom plot of the figure shows the unfiltered and baseline spectra along the green line in the two multidimensional spectral plots. The total power of the signal has been reduced by 71% with all of the narrow-band signals removed. A large portion of this signal removal is the very low temporal frequency components. The blade-passing frequency and harmonics are completely removed but the broadband acoustic duct-modes remain intact. The peak of the boundary-layer signal is reduced slightly as well as the high frequency fluctuations.

6.5 Basic Filter Summary

Three different basic wavefront filters were shown and discussed in this chapter. The temporal filter is most useful when filtering out a frequency band of optical noise. Besides filtering out optical noise, band-pass filters can be used to analyze a wavefront over a narrow-band to examine the optical aberrations at specific frequencies that significantly contribute to the overall optical disturbance; for

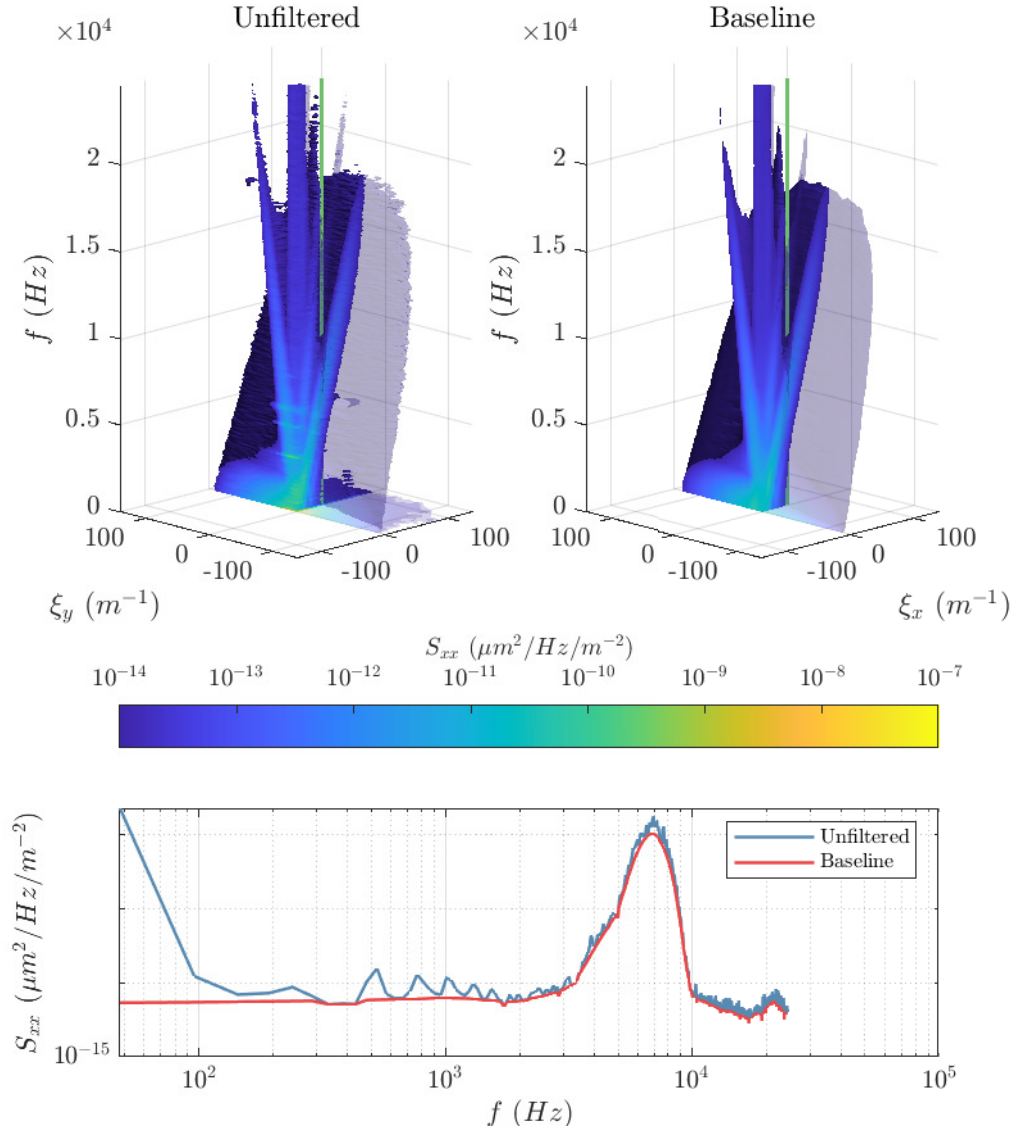


Figure 6.7. Baseline spectrum estimation. The top left plot shows the unfiltered multidimensional spectrum and the baseline spectrum on the top right. The green line in each of these plots represents the location at which the spectra in the bottom plot is shown.

example, as was shown in Chapter 3, band-pass filters along with an implementation of an acoustic mode-marching method can help determine with some confidence that a narrow-band signal is likely to have been created by the wind-tunnel fan and can be removed.

Filters that separate upstream and downstream-moving disturbances are useful to filter out the optical contamination that comes from acoustic signals that are traveling upstream from a wind-tunnel fan. These filters would also be useful for separating out an aero-optical signal that has a broad range of velocities that can occur in a span wise measurement of a boundary layer. The velocity filter is the most useful for isolating the aero-optical portion of a wavefront measurement given the aero-optical signal has a fairly narrow and constant velocity range. This filter also can be used to measure the speed associated with an optical disturbance in both x and y-directions.

The spectral baseline provides an simple way of removing all of the narrow-band signals with slight attenuation to the broadband signals. The broadband acoustic and stationary modes remain but could be filtered with via other techniques such as using a velocity filter. Narrow-band features that are not likely to be environmental contamination could be easily added back in.

6.6 Multiple Sensor Filtering of Optical Wavefronts

In the previous sections, methods of filtering optical wavefront corruption by applying a variety of filters to the wavefront in the multidimensional spectral domain were investigated. These techniques involve only data from the optical wavefront itself and user knowledge and experience to obtain filtered data. When additional data are available, such as from microphones or accelerometers, a targeted filter approach becomes possible.

This kind of approach is described in a previous study [37] in which a combination of linear stochastic estimation (LSE) and spectral proper orthogonal decomposition (SPOD) was used to remove vibration related contamination from aero-optical wind-tunnel measurements. This process along with optical tip and tilt removal showed approximately an 85% removal of contamination in the measured OPD_{RMS} by using accelerometer measurements to remove vibration effects from optical wavefront measurements.

Finally, this chapter concludes by showing results produced by applying the LSE-SPOD filter to experimental wavefront data acquired in the White Field wind tunnel, both by itself and in combination with the filters described in Chapter 6. The objective of the filtering approaches shown was to filter out contamination from the aero-optical signal produced by the boundary layer on the measurement aperture. The performance of the various filtering methods are compared and

recommendations for the best filtering approach are given.

6.6.1 Optical Tip and Tilt

Although they are usually not employed in aero-optical investigations, Zernike polynomials have been traditionally used for modal decomposition of the optical aberrations of an optical system [5]. These polynomials are defined on the unit circle and form a set of orthogonal functions,

$$Z_n^m(\rho, \theta) = R_n^m(\rho) \cos(m\theta) \quad (6.13)$$

where $R_n^m(\rho)$ is the radial basis function and $\cos(m\theta)$ is the angular basis function. For values of $-m$ the angular basis function becomes $\sin(m\theta)$. The radial basis function are developed from Jacobi polynomials but for purposes of this study, only a few simple ones will be used. An optical wavefront can be represented by a summation of Zernike polynomials multiplied by their corresponding coefficients

$$WF = \sum Z_j a_j. \quad (6.14)$$

The Noll naming scheme is a method of organizing the Zernike polynomials into a single notation of Z_j , along with normalizing each polynomial to have a spatial RMS equal to one [47]. The first three of these using the Noll naming scheme are piston, tip, and tilt. Piston is simply the average OPD value of the wavefront

$$Z_1 = 1. \quad (6.15)$$

Tip and tilt are the best planar fit to the OPD along the x-axis and y-axis respectively where tip is

$$Z_2 = 2\rho \cos \theta, \quad (6.16)$$

and tilt is

$$Z_3 = 2\rho \sin \theta. \quad (6.17)$$

Once the coefficients for these modes are solved for they can be removed from the original wavefront, WF :

$$WF^F = WF - \sum Z_j a_j. \quad (6.18)$$

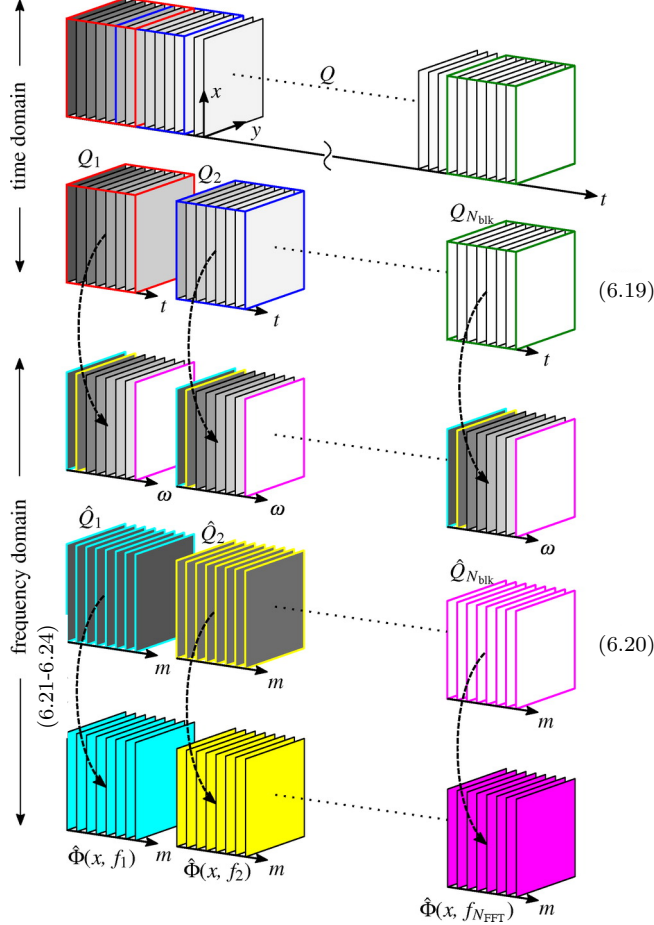


Figure 6.8. Schematic of the SPOD algorithm (taken from [53]). The numbers in parentheses denote the equations used.

6.6.2 LSE-SPOD

The LSE-SPOD technique starts with performing SPOD on the primary data set and then using the Fourier transforms of the additional sensor data to perform a filtering operation. The spectral proper orthogonal decomposition technique is described in detail by Schmidt and Colonius [53]. A schematic of the SPOD algorithm is shown in Figure 6.8. The algorithm begins by separating the original data set, Q , into a number of smaller blocks,

$$Q = \begin{bmatrix} | & | & & | \\ q^{(1)} & q^{(2)} & \dots & q^{(N)} \\ | & | & & | \end{bmatrix}, \quad Q \in \mathbb{C}^{M \times N} \quad (6.19)$$

where M is the total number of degrees of freedom (number of spatial points times the block length in time) and N is the number of blocks. Each block is then Fourier Transformed in the temporal dimension or through all dimensions. Once in the frequency domain the data blocks are then reorganized by creating new blocks of identical temporal-frequencies,

$$\hat{Q} = \begin{bmatrix} | & | & & | \\ \hat{q}^{(1)} & \hat{q}^{(2)} & \dots & \hat{q}^{(N)} \\ | & | & & | \end{bmatrix}, \quad \hat{Q} \in \mathbb{C}^{M \times N} \quad (6.20)$$

where M is now the number of spatial points times the number of blocks and N is block length in time. Proper orthogonal decomposition is then performed separately on each temporal-frequency block via either traditional POD

$$\hat{C} = \frac{1}{N-1} \hat{Q} \hat{Q}^H, \quad (6.21)$$

$$\hat{C} W \hat{\Phi} = \hat{\Phi} \hat{\Lambda}, \quad (6.22)$$

or the method of snapshots,

$$\hat{Q}^H W \hat{Q} \hat{\Psi} = \hat{\Psi} \hat{\Lambda}, \quad (6.23)$$

$$\hat{\Phi} = \hat{Q} \hat{\Psi}, \quad (6.24)$$

where H denotes the Hermitian transpose, W is a weighting matrix, Φ is the set of deterministic spatial functions, Λ is the eigen-values, and Ψ is the coefficient matrix.

The linear stochastic estimation portion of the technique is described by Adrian [2]. This process uses a linear sum, L_{ij} , of additional measurements, y_j , to approximate a measured signal, x_i ,

$$x_i^{LSE} = L_{ij} y_j, \quad (6.25)$$

where

$$L_{ij} = \langle x_i y_k \rangle \langle y_j y_k \rangle^{-1}. \quad (6.26)$$

When combined with SPOD, the estimation matrix, L , becomes

$$L = (\hat{\Psi} \hat{y}^H)(\hat{y} \hat{y}^H)^{-1}, \quad (6.27)$$

which allows for an estimated version of the coefficient matrix to be calculated

$$\hat{\Psi}^E = L\hat{y}. \quad (6.28)$$

The estimated coefficient matrix contains portions of the original signal that best resemble the additional sensor data. Assuming that the additional sensor data represents signal contamination of the original signal, a filtered coefficient matrix can be computed from the difference between the original and estimated coefficient matrices.

$$\hat{\Psi}^F = \hat{\Psi} - \hat{\Psi}^E. \quad (6.29)$$

A filtered signal, Q^F can be constructed by using the filtered coefficient matrix and the spatial functions,

$$\hat{Q} = \hat{\Psi}^F \hat{\Phi}^H. \quad (6.30)$$

6.6.3 Filtering Experimental Data

The filtering technique described in the preceding section was applied to the same data sets that were shown in Figure 4.7, either separately or in combination with the basic filtering methods described earlier in this chapter. Simultaneous accelerometer and microphone measurements were made alongside the optical wavefront measurements. The locations of some of the additional sensors are shown in Figure 6.9 with a CAD drawing of the test section in Figure 6.10. Table 6.1 shows a list of the additional sensors including the number designation used in Figures 6.9 and 6.10, the model of the sensor and preamplifier used as well as a sensor grouping designation. All of the test-section mounted sensors are shown in their approximate locations in Figure 6.10 in a view that is looking at the wind-tunnel model from inside of the test-section with the flow moving from left-to-right. The dashed box represent the optical window on the opposite side of the tunnel from the model which was moved up or downstream depending on the beam angle relative to the flow. Sensors 11-13 were attached to this optical window and moved with it. The picture in Figure 6.9 was taken from the opposite side of the test-section and model that is shown in Figure 6.10 and as such the flow goes from right-to-left.

Two microphones were used for ambient measurement (a ACO 7016B [13] and a Brüel & Kjær 4939 [8]), four microphones were used for test-section noise measurement (PCB 103B02 [48]), and ten accelerometers were located throughout the setup (PCB 352C33 [49]). One of the ambient

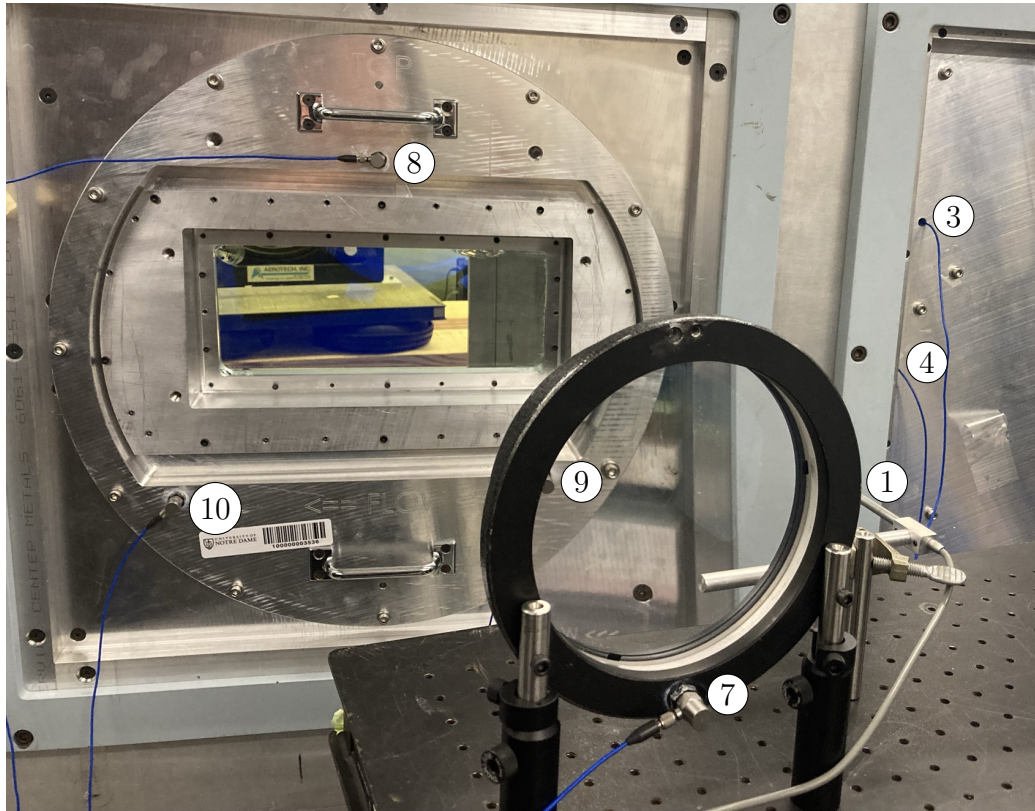


Figure 6.9. The locations of some of the additional sensors used in the LSE-SPOD filtering. The sensors are labeled with the sensor numbers, see Table 6.1.

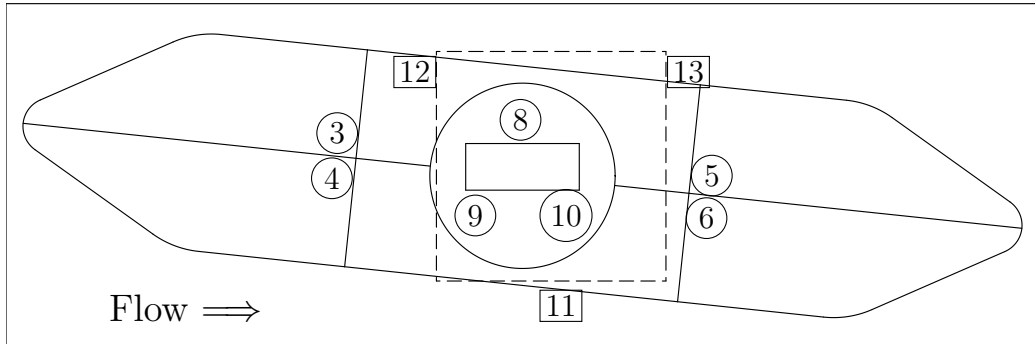


Figure 6.10. CAD drawing view of the inside of the test-section with some of the sensor locations labeled. Flow is from left to right. The numbers in the circles are the sensor numbers on the model side of the test-section. The numbers in the square are the sensor numbers opposite of the model side. The dashed line represents the optics window opposite of the model for the beam angle of 90° . The window was moved up and downstream depending on the beam angle.

TABLE 6.1

ADDITIONAL SENSORS USED THE THE LSE-SPOD FILTERING.

Channel	Sensor Type	Model	Preamp	Group
1	Microphone	ACO 7016B	B&K 2690	Ambient
2	Microphone	B&K 4939	B&K 2690	Ambient
3	Microphone	PCB 103B02	PCB 483C	Test Section
4	Microphone	PCB 103B02	PCB 483C	Test Section
5	Microphone	PCB 103B02	PCB 483C	Test Section
6	Microphone	PCB 103B02	PCB 483C	Test Section
7	Accelerometer	PCB 352C33	PCB 483C	Primary Lens
8	Accelerometer	PCB 352C33	PCB 483C	Test Section
9	Accelerometer	PCB 352C33	PCB 483C	Test Section
10	Accelerometer	PCB 352C33	PCB 483C	Test Section
11	Accelerometer	PCB 352C33	PCB 482A22	Test Section
12	Accelerometer	PCB 352C33	PCB 482A22	Test Section
13	Accelerometer	PCB 352C33	PCB 482A22	Test Section
14	Accelerometer	PCB 352C33	PCB 482A22	Optics Bench
15	Accelerometer	PCB 352C33	PCB 482A22	Return Mirror
16	Accelerometer	PCB 352C33	PCB 482A22	Return Mirror

microphones was mounted to the top of the optics bench facing the test-section and can be seen in Figure 6.9 just to the right of the primary lens and the other ambient microphone was hanging below the optics bench end towards the test-section.

The test-section microphones were in groups of two either upstream or downstream from the optical beam by about 20-inches, with the upstream microphone locations viewable in Figure 6.9 (sensors 3 and 4) and shown in Figure 6.10. The model installed in the test-section represents the outside of an aircraft fuselage with a 5-foot diameter and is angled to account for the aircraft's angle-of-attack (6°) for steady-level-flight at cruise. This results in the fuselage model being shifted approximately 2-inches higher from the test-section centerline upstream at the microphone location. The duct microphones were placed about 2.75-inches from the model centerline.

There were six accelerometers attached to the test-section windows, with three being on each side as shown in Figure 6.10. The locations of the three accelerometers (sensors 8-10) on the model side can be seen in Figure 6.9, the three accelerometers on the other window used the opposite pattern (two high and one low). The optical window on the far side of the test-section was moved laterally depending on the angle of the beam relative to the flow. One accelerometer was placed on the primary lens (also shown, sensor 7) and one was placed in the center of the optics bench. The last two accelerometers were located on the back of the return mirror with one on the top and the other on the side.

6.7 Results

The power-spectra of all of the sensors at the three Mach numbers are shown in Figure 6.11. These plots are presented as Strouhal number per unit characteristic length, since this puts the signals related to the fan blade-passing frequency at the same x-axis location for all three tested wind speeds. Figure 6.11 also shows the different groups of sensors shown together in separate plots. The blade-passing frequency for these data sets is at a St/l of approximately 3 m^{-1} with a clear and consistent narrow-band signal at that St/l for all but the $M = 0.3$ run, which has a slight increase in signal for some of the sensors. For the $M = 0.5$ case there is an additional strong narrow-band signal at 20 m^{-1} for all sensors and a slightly broader signal at 38 m^{-1} that is only present in the test-section mounted sensors that may be due to extra fan vibration which was limiting the top speed of the wind-tunnel. The test-section mounted microphones are picking up boundary layer acoustic noise above St/l of approximately 20 m^{-1} .

Two variants of the filtering technique were tried. The first was a standard LSE-SPOD technique

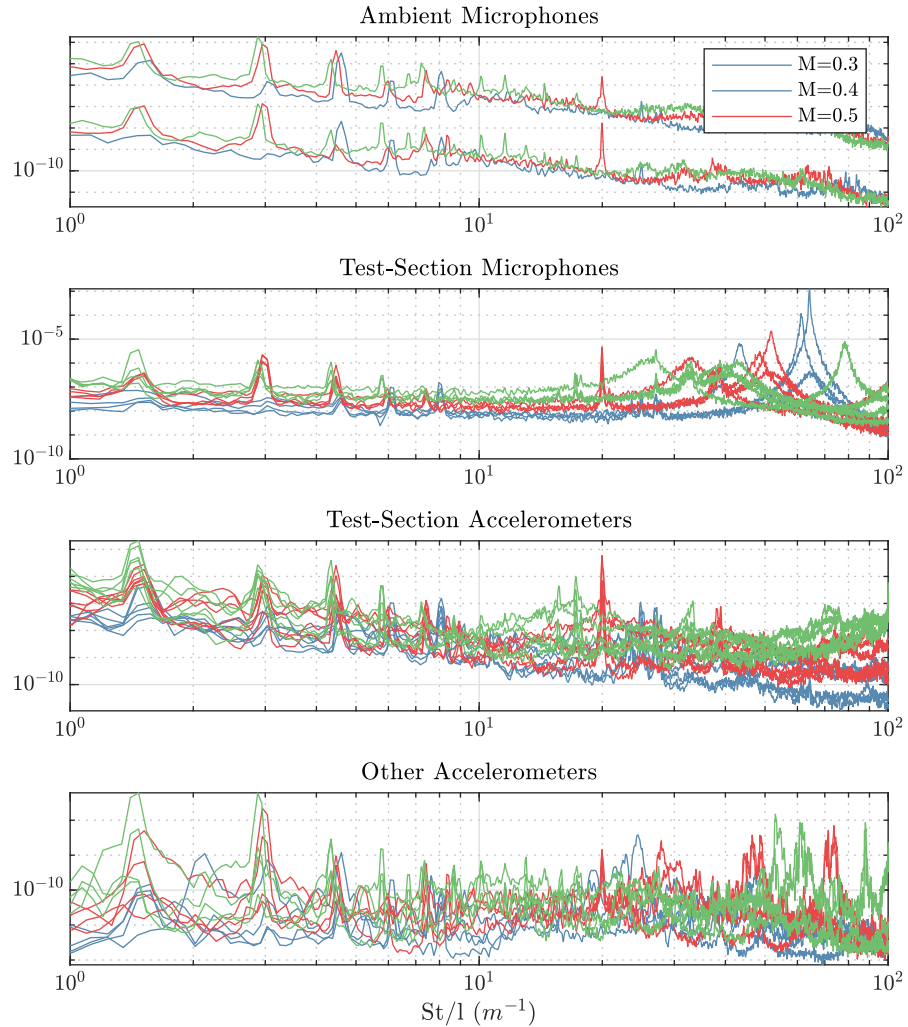


Figure 6.11. Power-spectra of the additional sensor measurements at the three Mach numbers tested. The x-axis is in Strouhal number per characteristic length (St/l).

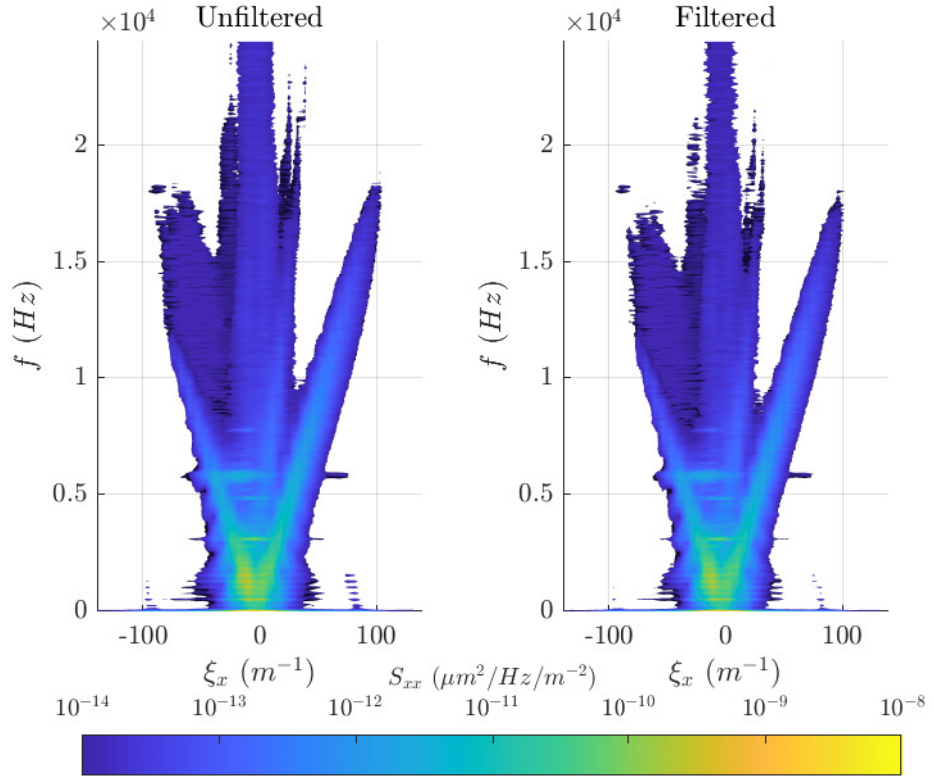


Figure 6.12. A multidimensional power spectrum of an unfiltered wavefront and the same wavefront filtered with the LSE-SPOD method using all 16 additional microphone or accelerometer measurements.

in which the spectral POD was performed on the data set that was Fourier transformed in time only. For the second technique, which will be referred to here as LSE-MSPOD, the spectral POD was applied to a data set in which the Fourier transform was performed in all dimensions of space and time, which is a portion of the computation for the multidimensional spectral estimation. Figures 6.12 and 6.13 show multidimensional power spectrum plots at a temporal block length of 2^{10} with no overlap. These plots show the f - ξ_x plane of the multidimensional spectrum that captures horizontally-moving (streamwise) plane waves with a portion of the acoustic cone isosurface wrapping behind it. Both of these methods performed effectively identically to one another with a 14.2% drop in overall RMS value of the filtered wavefront (both time and space). There is a significant drop in the signal at the blade-passing frequency and its harmonics, especially at the higher spatial frequencies. The stationary signal information is also significantly reduced along with the high temporal-frequency acoustic signal. The aero-optical boundary layer signal is also partially

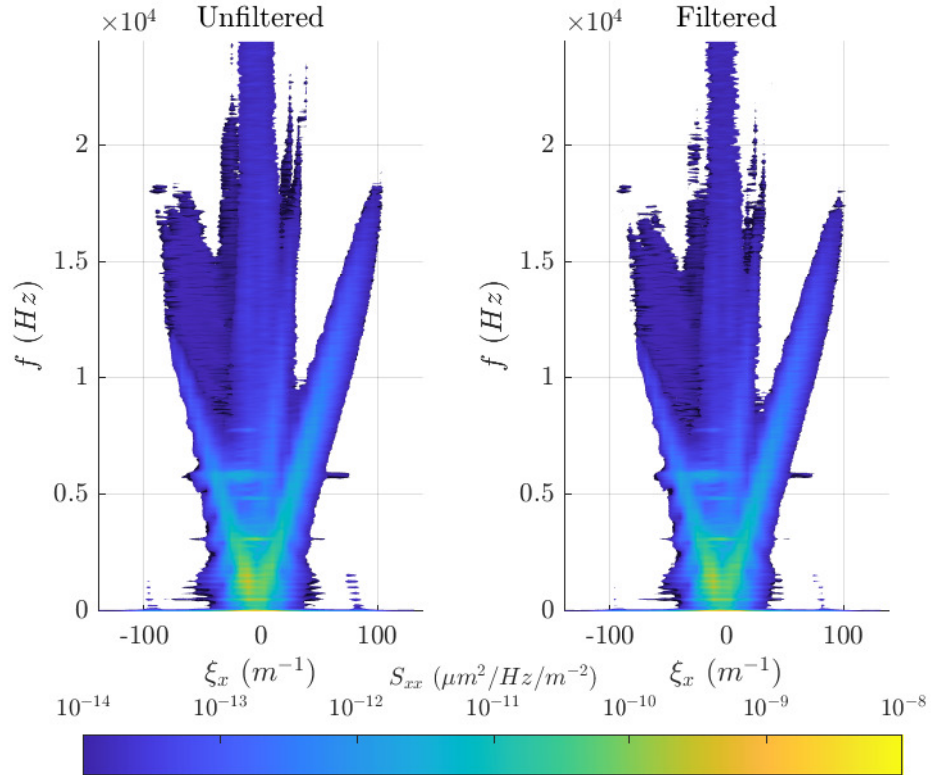


Figure 6.13. A multidimensional power spectrum of an unfiltered wavefront and the same wavefront filtered with the LSE-MSPOD method using all 16 additional microphone or accelerometer measurements.

TABLE 6.2

OPD_{RMS} (μm) COMPARISON OF USING DIFFERENT COMBINATIONS OF
ADDITIONAL SENSOR INFORMATION IN THE LSE-MSPOD FILTERING
PROCESS.

	M=0.3	M=0.4	M=0.5
Original	0.0561	0.0521	0.0824
Tip/Tilt Removal	0.0120(78.6%)	0.0195(62.6%)	0.0291(64.7%)
Accelerometers	0.0102(81.8%)	0.0168(67.7%)	0.0251(69.5%)
Ambient Microphones	0.0103(81.7%)	0.0170(67.3%)	0.0254(69.1%)
Duct Microphones	0.0103(81.6%)	0.0170(67.3%)	0.0255(69.0%)
Test-Section Sensors	0.0103(81.6%)	0.0168(67.8%)	0.0252(69.4%)
All Sensors	0.0099(82.3%)	0.0163(68.8%)	0.0242(70.6%)

reduced, which is most noticeable at higher temporal-frequencies.

Table 6.2 shows the time averaged OPD_{RMS} of three different data sets at a beam angle through the test-section of 90°. The data sets were at Mach numbers of 0.3, 0.4, and 0.5 and had an unfiltered OPD_{RMS} of 0.0561, 0.0521, and 0.0824 μm respectively. Note that in the raw processed wavefronts, the OPD_{RMS} at a Mach number of 0.3 was higher than the 0.4 case. There was a significant drop of between 62.6 and 78.6% in the OPD_{RMS} by removing the Zernike modes corresponding to tip and tilt. It is at this point the Mach number of 0.4 case has a higher OPD_{RMS} than the 0.3 case as would be expected [23]. Note that it is standard practice to remove optical tip/tilt from wavefront measurements, since tip/tilt is largely imposed by the measurement optics rather than the actual aero-optical flow.

Table 6.2 also shows the effect of five different combinations of additional sensors that were used for filtering with the LSE-MSPOD process (the bracketed percentage in Table 6.2 shows the percent reduction in OPD_{RMS} due to the filtering). The first set was all of the accelerometers which resulted in an additional drop in OPD_{RMS} of between 3 and 5%. The second and third sets used either the ambient or duct microphones and those sets had slightly less reduction than the accelerometers. The fourth set was the test-section sensors comprised of six window mounted accelerometers and four duct mounted microphones. This set of sensors performed the same as all of the accelerometers,

while the use of all of the additional sensors in the last set performed the best, with an additional reduction in OPD_{RMS} of 4 to 6% from the tip/tilt removal cases.

In summary, Table 6.2 shows that using either the temporal or multidimensional version of the LSE-SPOD filtering technique can help remove some of the narrow-band acoustic and vibration reduction in an optical wavefront. These temporally narrow-band signals have broadband spatial content that is attenuated. This additional reduction does seem to be somewhat tied to the number of sensors used with more sensors having a greater impact on the signal reduction. Since the vibrations and acoustics have the same primary source, the wind-tunnel fan, they seems to do a relatively equivalent job at filtering the optical contamination. Accelerometers have the benefit of easier installation but the microphones do not necessarily have to be installed inside of the wind-tunnel.

CHAPTER 7

COMBINATION OF FILTERS

The previous chapter investigated a series of filters that were applied in a singular fashion to a set of optical wavefronts. This chapter will discuss combining several of these filters together in series.

7.1 Velocity and LSE-SPOD Filter

In addition to the LSE-SPOD filter using all 16 additional sensors that was shown in Chapter 6, a velocity filter was applied to the wavefront first. Table 7.1 shows the summary of these filters when used separately or together. The LSE-SPOD was shown previously to remove vibration noise from wavefront measurements with an approximately 85% reduction in OPD_{RMS} at Mach of 0.3 [37]. Similar results were observed using the combination of optical tip/tilt removal and LSE-SPOD on both single dimension (temporal) and multidimensional spectra. Optical tip/tilt removal alone accounted for a 78.6% reduction in OPD_{RMS} , with a combination of 16 microphones and accelerometers and the LSE-SPOD bringing the reduction in OPD_{RMS} to 83.9% at Mach of 0.3. The combination of tip/tilt removal and the velocity filter showed a greater reduction of 82.3%. At a Mach number of 0.5, the use of optical tip/tilt removal, the velocity filter, and 16 sensors in LSE-SPOD, the OPD_{RMS} was brought down to $0.0181 \mu\text{m}$ and still showed a significant amount of narrow-band signals (see Figure 6.12 and 6.13). This is about a 30% reduction when compared with the other filters used in Table 7.2, and represents almost entirely an additional reduction in contamination to the aero-optical signal by removing the broadband disturbances. This was also significantly above the estimated OPD_{RMS} of $0.0142 \mu\text{m}$ for the $M = 0.6$ case (See Section 2.1.2 and [23]).

With the LSE-SPOD method the more sensors that were used in the filtering process the greater the reduction in the OPD_{RMS} , as can be seen in Figure 7.1. The combination of the DAQ and preamplifier used for the duct-mounted microphones had a significantly lower dynamic range when compared to the other sensors, possibly leading to a diminished reduction in the performance of the

TABLE 7.1

OPD_{RMS} (μm) COMPARISON OF USING LSE-MSPOD FILTERING PROCESS
WHEN COMBINED WITH A VELOCITY FILTER.

	M=0.3	M=0.4	M=0.5
Original	0.0561	0.0521	0.0824
LSE-MSPOD	0.0099(82.3%)	0.0163(68.8%)	0.0242(70.6%)
Velocity Filter	0.0090(83.9%)	0.0146(72.1%)	0.0217(73.7%)
Velocity+LSE-MSPOD	0.0075(86.7%)	0.0122(76.7%)	0.0181(78.0%)

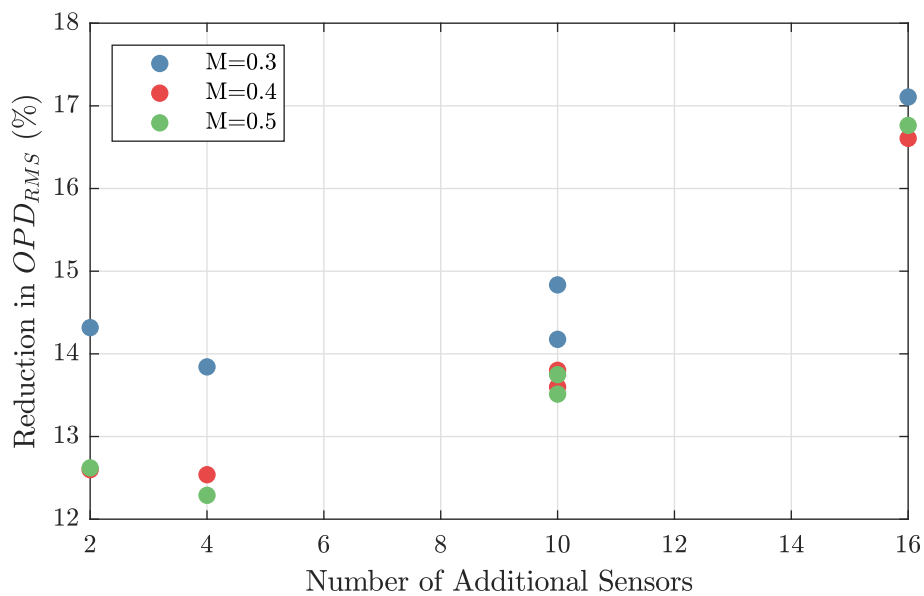


Figure 7.1. Percent reduction in OPD_{RMS} from the tip/tilt removed case using LSE-SPOD filtering.

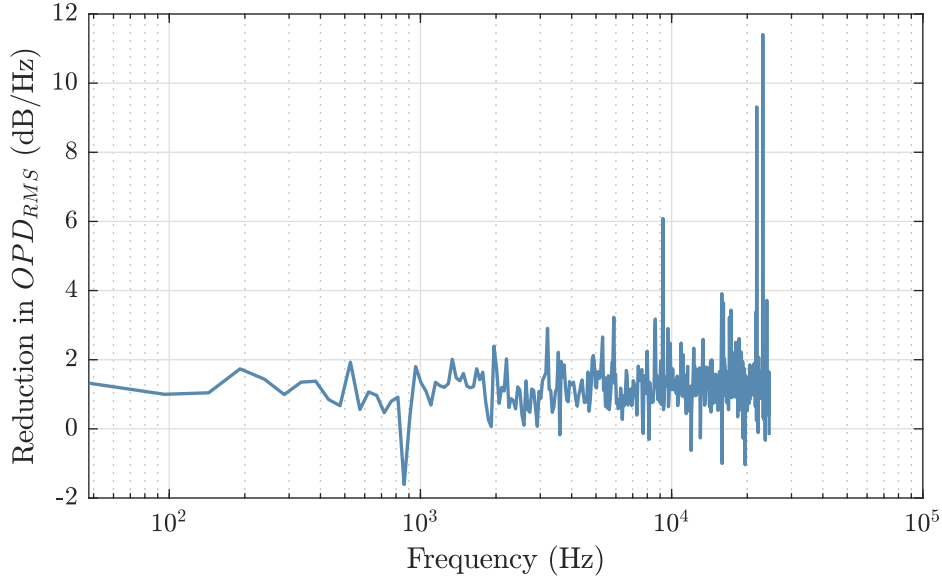


Figure 7.2. Reduction in $OPD_{RMS}(t)$ as a function of temporal frequency using 16 sensors with LSE-SPOD in the $M=0.5$ case when compared to tip/tilt removal.

four-sensor filtering. The signal reduction using all 16 sensors was fairly uniform with frequency, as shown in Figure 7.2. On average there was a 1.3dB/Hz reduction in the OPD_{RMS} with slight peaks at some of the significant narrow-band signals. At the blade-passing frequency (517 Hz) there was a 2dB/Hz reduction and for the narrow-band signals around 3 and 6 kHz there was a 3dB/Hz reduction. The first, second, and third harmonics of the blade-passing frequency, at 1034 Hz, 2068 Hz, and 4136 Hz, had a below average reduction in the signal.

While the use of additional sensor measurements to aid in filtering of optical wavefront measurements using LSE-SPOD showed little benefit in this study (at least compared to the single sensor filtering techniques), it could show significant benefit in future measurements. Specifically, for measurements with models that are likely to create narrow-band signal noise, additional sensor information could be used in conjunction with a baseline filter for determining which narrow-band signals that need to be retained in the spectrum.

7.2 Backward, Velocity, and Baseline Filter

Among the filters discussed, three are useful for isolating aero-optical signals from a wavefront. The first of these is a filter for separating the portion of the optical disturbances that are moving either upstream or downstream to the flow (Section 6.2). An undesirable effect of this filter is that

it may remove some of the aero-optical signal, which can happen to the boundary-layer signal¹ at low temporal frequencies. The second useful filter is the low-pass velocity filter which preserves the signal that is moving within a narrow velocity range (Section 6.3). The third is the baseline estimator (Section 6.4), which removes the narrow-band signals associated with the blade-passing frequency and its harmonics, the mean-lensing component, and other temporally narrow-band signals. However, some of these removed narrow-band signals could include part of the aero-optical signal of the wind-tunnel model.

Figure 7.3 shows the multidimensional spectra of the output of these three filters individually plus the spectra of these three filters combined. The backward moving filter, that removes all upstream-moving disturbances (Figure 7.3 top left), does remove some of the boundary-layer signal at low temporal frequencies. The portion of the acoustic cone and stationary modes that are on the downstream-moving portion of the spectrum are retained. The velocity filter (Figure 7.3 top right) removes most of the broadband signal from the various noise sources. There is a portion of the acoustic cone and stationary modes that intersect or lay near the boundary-layer signal that is slightly attenuated, producing a slight hump on the upstream-moving side of the boundary-layer that extends up to about 10 kHz and along the ξ_y axis over the range of about $\pm 25 m^{-1}$.

The baseline filter (Figure 7.3 bottom left) removes all of the temporal narrow-band signals including the mean-lensing portion of the spectra. The noisy surface of the spectra is removed which also eliminates some of the boundary-layer aero-optical signal. The combination filter (Figure 7.3 bottom right) applies the velocity and backward moving filter to the baseline filter. This filter loses some of the boundary-layer signal due to the noisy surface being smoothed out and the portion that crosses into the upstream-traveling portion of the spectrum. The portion of the acoustic cone and stationary modes that is the most contaminating in the velocity filter is removed due to the backward moving and baseline filter.

A zoomed in slice of the multidimensional spectra is shown in Figure 7.4 for the horizontal moving plane waves. A large portion of the signal contamination happens at the blade-passing frequency and its harmonics as well as in the mean-lensing region. This contamination is present in all of the multidimensional spectra that do not utilize the baseline filter. Even with the velocity filter there is significant contamination on the upstream-moving portion of the spectra due to these narrow-band signals as well as due to the presence of the acoustic cone and stationary modes. While the backward moving filter removes some of the boundary-layer signal it removes significantly more

¹These low frequency aero-optical disturbances may be a combination of the outer boundary layer and free-stream turbulence.

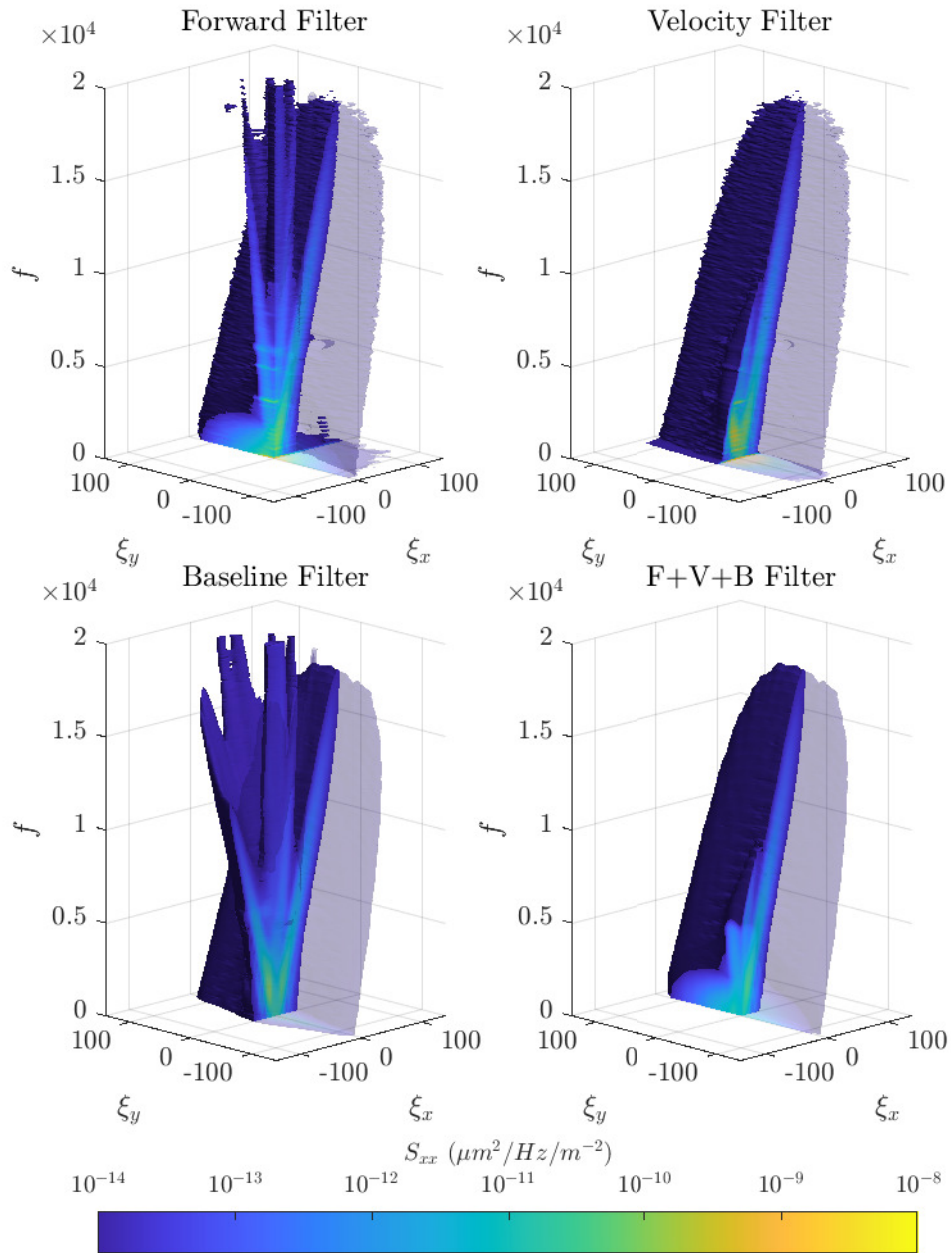


Figure 7.3. Multidimensional spectra of three single sensor filtering techniques and a combination filter.

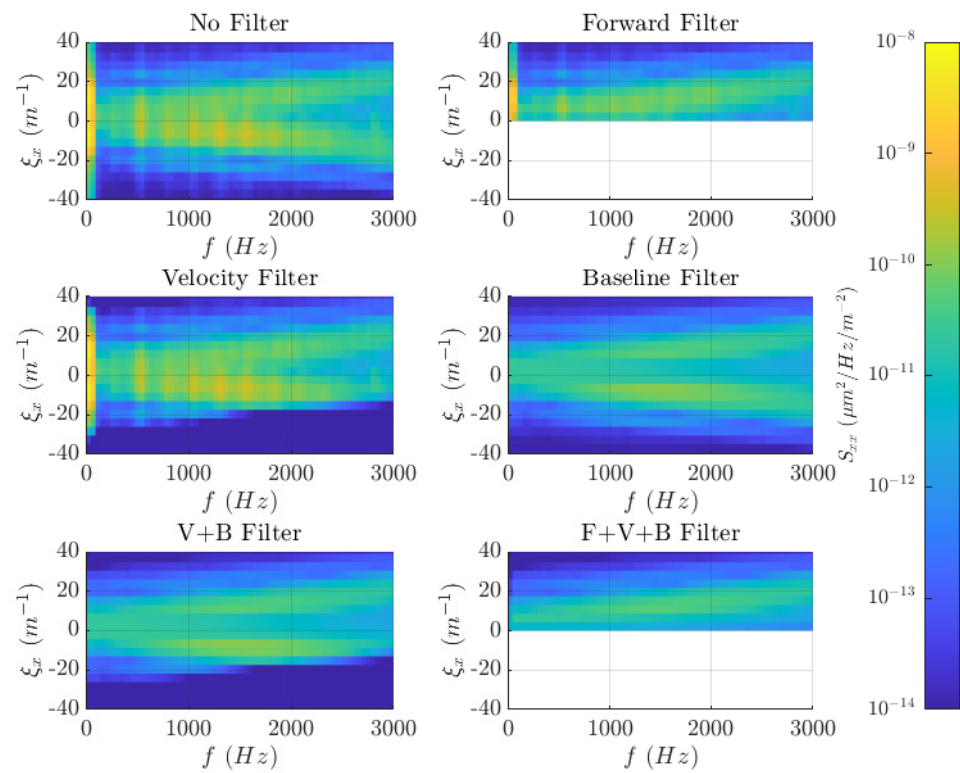


Figure 7.4. Multidimensional spectral slices for the various single sensor filtering techniques showing the horizontal moving plane waves.

TABLE 7.2
SUMMARY OF SINGLE SENSOR FILTERS

Filter	OPD _{RMS} (μm)
None	0.0260
Backward Moving	0.0166
Velocity	0.0238
Baseline	0.0156
V+B	0.0140
BM+V+B	0.0110

of the noise signals that would otherwise be present in the spectra with just the velocity and baseline filters applied.

Representative wavefronts were generated from these multidimensional spectra using the same process as generating a synthetic wavefront from the synthetic spectra in Chapter 5 in order to calculate the OPD_{RMS}. Table 7.2 shows the OPD_{RMS} values for the various filters used in Figure 7.4. Both the backward moving and baseline filters reduced the OPD_{RMS} of the wavefront a similar amount of 36 and 40% respectively. The velocity filter only reduced the OPD_{RMS} a small amount of 8.5% due to the retention of the strongest portion of the narrow-band signals. The combination of the velocity and baseline filters reduced the OPD_{RMS} of the wavefront by 46% but those still retain a significant portion of the acoustic cone and stationary mode signal. By combining these three single sensors filters, the OPD_{RMS} was reduced 58% but this is likely under the true value due to some loss of the boundary-layer signal from the backward moving filter at low temporal frequencies and the removal of the fluctuations from the baseline filter. There could be some narrow-band signals that would be generated by a model that would be removed with this filtering scheme. The estimated OPD_{RMS} from Gordeyev [23] (Equations 2.23 and 2.26) is 0.0142 μm for a double boundary layer, which puts the velocity and baseline filter combination in good agreement.

CHAPTER 8

CONCLUSION

When aero-optical measurements are made in a wind tunnel, there are a number of sources that contaminate the measurement with noise. This can be seen in Figure 8.1 which shows a multidimensional spectral estimation of an optical wavefront measurement made in a wind tunnel. Figure 8.1 shows the full multi-dimensional spectrum for wavefront data acquired in a wind tunnel, including streamwise and vertical spatial frequencies (ξ_x and ξ_y), and temporal frequencies (f); however, in Figure 8.1, the half of the isosurface which represents the portion of the signal that has a component that is traveling vertically downward has been made transparent to show some of the internal power spectrum of planar waves that are traveling parallel to the direction of flow.

In Figure 8.1, the aero-optical signal that is considered to be the objective of the measurement is the boundary layer which resembles a thin ellipsoid that has an angle in the $x - \xi_x$ plane (where the xi_x -coordinate represents spatial frequencies in the stream-wise direction) by an amount related to the free-stream velocity (see Equation 4.4). Acoustic duct modes make up a temporally broadband signal that forms a cone and have a significant portion of the signal that travels upstream. In the $\xi_x - f$ plane the outer surface of the acoustic cone is limited by the sonic lines at $u \pm c$, while in the $\xi_y - f$ plane the limit is at $\pm c$. The wind-tunnel fan produces temporally narrow-band acoustic and vibration modes that are able to contaminate the wavefront measurement at the blade-passing frequency (BPF) and its various harmonics.

Sources of noise shown in Figure 8.1 not related to the acoustics include stationary modes and mean-lensing. The stationary modes do not travel in any direction, their spatial frequencies are near zero and their signal strength is fairly constant in time. Due to the temporally white-noise nature of this signal, it is likely not physically relevant and could be optical mode noise from the laser, electronic noise in the camera, or even numerical noise from the processing code. At lower frequencies, especially around the blade-passing frequency or its harmonics, there is likely a significant number of stationary modes that are due to vibration of various optical elements. The mean-lensing portion of the signal ($\lesssim 100$ Hz) is a slowly varying signal with large spatial frequency content. A color coded multidimensional spectral estimation plot that allows for easier identification

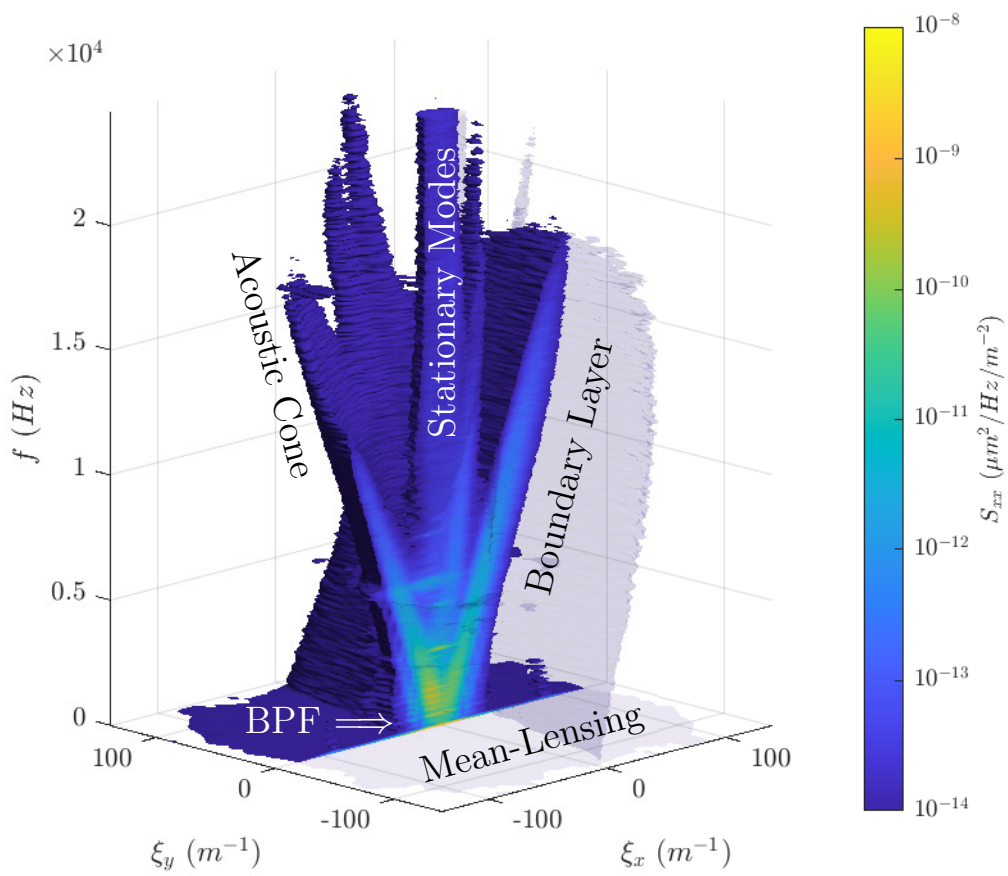


Figure 8.1. Multidimensional spectral estimation of an optical wavefront measurement made in a wind tunnel.

of the various component signals is shown in Figure 5.2 and was used for generating a synthetic wavefront. As such, a major contribution of this dissertation research is an improved understanding of the signals and contamination that appear in aero-optical data, and how those signals appear in multi-dimensional spectra. This information provides a better understanding of aero-optical data, as well as guidance towards methods of filtering out contaminating noise sources.

8.1 Filtering of Optical Wavefronts

Two main families of filtering techniques were examined in this dissertation. The first family was single sensor filters, Chapter 6, which operate on the optical wavefronts without knowledge of any other time resolved data. Some of these filters may rely on additional information about the average sampling conditions used to measure the wavefronts. The second family was multiple sensor filters, Chapter 7, which filter the optical wavefront using time resolved measurements from additional sensors.

8.1.1 Single Sensor Filters

The single sensors filters operated directly on the optical wavefront measurements. Most of these filters are based on Butterworth filters [9] that operate in the multidimensional Fourier domain using a transfer function, $\hat{H}(\xi_x, \xi_y, f)$,

$$\widehat{WF}(\xi_x, \xi_y, f) = \hat{H}(\xi_x, \xi_y, f) \text{FFT}_3(wf(x, y, t)), \quad (8.1)$$

which can be inverse Fourier transformed back into the physical domain or be used for calculating the multidimensional spectrum. Filtering can also be performed on the multidimensional spectrum using the gain function, $G^2 = \hat{H}\hat{H}^*$,

$$S_{xx}(\xi_x, \xi_y, f) = G^2(\xi_x, \xi_y, f) S_{xx}(\xi_x, \xi_y, f). \quad (8.2)$$

The only filter that was investigated that was not based on basic filters was a baseline spectrum estimator [55]. This filter removes narrow-band peaks and noise peaks along the temporal frequency axis smooth spectrum.

8.2 Other Useful Products

8.2.1 Synthetic Wavefront

A synthetic wavefront was developed in Chapter 5 to test various filters used in Chapter 6. In the process used to create the synthetic wavefront, each of these signal components was generated separately in the multidimensional spectrum. While this synthetic wavefront generation technique produced a qualitative approximation of a wavefront, it provided a useful set of fully known data to test various filters. There is some significant room for improvement in the process of creating synthetic wavefronts that are more physically accurate. Even without improvement this process may be useful in generating a set of synthetic wavefronts with a known aero-optical and noise components that can be used for training a neural network to filter [36] wavefront measurements. A neural network based filter may be able to separate the overlapping component signals at low frequencies.

8.2.2 Measuring Acoustic Field Optically

In section 3.2.2, optical wavefront were shown to have a fairly good agreement with a microphone for measuring the fluctuating field strength of a spherical wave generated by a speaker. The optical wavefront measurement however had issues when the acoustic field diverged from being nearly spherical. Optical wavefronts can be a method to non-intrusively measure an acoustic field, although the beam-path integrated results of the wavefront measurement require additional interpretation to extract information on the acoustic field.

8.2.3 Acoustic Mode-Marching

An acoustic mode-marching method was developed to quickly estimate the acoustic field within a wind-tunnel test-section assuming that the primary noise source was the wind-tunnel fan. Although, this is likely to have limited application in filtering of optical wavefronts, it is useful for assisting researchers in determining whether specific narrow-band signals are produced by the wind-tunnel fan and can be filtered out. Since there may be upstream-traveling components of the aero-optical signal such as that produced by recirculation zones or sound produced by the test model, the capability to definitively identify the optical signal produced by the wind-tunnel main fan is useful information. There also maybe some application during the initial design of a tunnel for estimating the acoustic field in some critical components.

8.3 Recommendations For Future Research

There is a lot of research that can still be done on various filtering techniques to remove signal contamination of aero-optical wavefront measurements. This is especially true for filters that can utilize additional sensor measurements. The process for creating the synthetic wavefronts used in this research was a qualitative approximation that can be made more physically accurate. Synthetic signal algorithms could be developed for types other aero-optical disturbances such as sheer layers [32]. Synthetic wavefront signals could aid in the testing of algorithms used on adaptive optic systems. The acoustic mode-marching analysis could be expanded to the case where a simple model in the wind-tunnel test section.

BIBLIOGRAPHY

1. 2pem. A schematic illustration of a shwfs. https://commons.wikimedia.org/wiki/File:Shack_Hartmann_WFS_lensletarray.svg.
2. R. J. Adrian. On the role of conditional averages in turbulence theory. In *Symposia on Turbulence in Liquids*, 1975.
3. M. An, I. Gertner, M. Rofheart, and R. Tolimieri. Discrete fast fourier transorm algorithms: A tutorial survey. *Advances in Electronics and Electron Physics*, 80:1–67, 1991. doi: 10.1016/S0065-2539(08)60607-1.
4. R. B. Blackman and J. W. Tukey. *The Measurement of Power Spectra - From the Point of View of Communications Engineering*. Dover, 1958.
5. M. Born and E. Wolf. *Principles of Optics*. Pergamon, 1965.
6. S. Braun, editor. *Encyclopedia of Vibration*. Academic Press, 2001.
7. Brüel & Kjær. 2670. <https://www.bksv.com/-/media/literature/Product-Data/bp1584.ashx>, November 2018. Product Data.
8. Brüel & Kjær. 4939. <https://www.bksv.com/-/media/literature/Product-Data/bp1851.ashx>, October 2021. Product Data.
9. S. Butterworth. On the theory of filter amplifiers. *Experimental Wireless and the Wireless Engineer*, 7:536–541, 1930.
10. B. L. Catron, M. R. Rennie, S. Gordeyev, and E. J. Jumper. Effect of acoustic disturbances on aero-optical measurements. In *2018 Plasmadynamics and Lasers Conference*, 2018. doi: 10.2514/6.2018-3903.
11. B. L. Catron, M. R. Rennie, S. Gordeyev, and E. J. Jumper. Filtering of acoustic disturbances from aero-optical measurements. In *AIAA Scitech 2020 Forum*, 2020. doi: 10.2514/6.2020-0683.
12. J. M. Cicchiello and E. J. Jumper. Far-field optical degradation due to near-field transmission through a turbulent heated jet. *Applied Optics*, 36(25):6441–6452, 1997. doi: 10.1364/AO.36.006441.
13. A. CO. Sound measurement microphone. https://www.aco-japan.co.jp/pdf/en_microphone.pdf. Product Catalog.
14. N. A. Cumpsty. *Compressor Aerodynamics*. Krieger Publishing, 1989.
15. N. De Lucca, S. Gordeyev, E. J. Jumper, and D. J. Wittich. Effects of engine acoustic waves on optical environment around turrets in-flight on aaol-t. *Optical Engineering*, 57(6), 2018. doi: 10.1117/1.OE.57.6.064107.
16. O. T. . E. Director. Fy99 annual report - airborne laser (abl). <https://www.globalsecurity.org/military/library/budget/fy1999/dot-e/airforce/99abl.html>, 2000.
17. A. Fresnel. *Mémoire sur la diffraction de la lumière*. Oeuvres complètes, 1818. Partially translated by Henry Crew in *The Wave Theory of Light* in 1900.

18. G. Gabard and R. Astley. A computational mode-matching approach for sound propagation in three-dimensional ducts with flow. *Journal of Sound and Vibration*, 315:1103–1124, 2008. doi: 10.1016/j.jsv.2008.02.015.
19. J. M. Geary. *Introduction to Wavefront Sensors*. SPIE Optical Engineering Press, 1995.
20. J. H. Gladstone and T. P. Dale. Researches on the refraction, dispersion, and sensitiveness of liquids. *Philosophical Transactions of the Royal Society of London*, 153:317–343, 1863.
21. J. W. Goodman. *Introduction to Fourier Optics*. McGraw-Hill, 1968.
22. S. Gordelyev and M. Kalensky. Effects of engine acoustic waves on aerooptical environment in subsonic flight. *AIAA Journal*, 58(12):5306–5317, 2020. doi: 10.2514/1.J059484.
23. S. Gordelyev, A. E. Smith, J. A. Cress, and E. J. Jumper. Experimental studies of aero-optical properties of subsonic turbulent boundary layers. *Journal of Fluid Mechanics*, 740:214–253, 2014. doi: 10.1017/jfm.2013.658.
24. D. P. Greenwood. Bandwidth specification for adaptive optics systems. *Journal of the Optical Society of America*, 67(3):390–393, 1977. doi: 10.1364/JOSA.67.000390.
25. R. W. Hamming. *Digital Filters*. Dover, 3rd edition, 1998.
26. L. Huang, M. Idir, K. Kaznatcheev, L. Zhou, and A. Asundi. Comparison of two-dimensional integration methods for shape reconstruction from gradient data. *Optics and Lasers in Engineering*, 64, 2015. doi: 10.1016/j.optlaseng.2014.07.002.
27. C. Huygens. *Traité de la Lumière*. Van der Aa, 1690. Translated by Silvanus P. Thomson as *Treatise on Light* in 1912.
28. F. Jacobsen and P. M. Iler Juhl. *Fundamentals of General Linear Acoustics*. John Wiley & Sons, 2013.
29. Z. Ji and Z. Fang. Numerical mode-matching approach for acoustic attenuation prediction of expansion chambers with single inlet and double outlets. In *Proceedings of Meetings on Acoustics*, Vol. 19, 2013. doi: 10.1121/1.4799442.
30. W. C. G. Jr., Y. Hidaka, and T. Tanzawa. Refractivity of combustion gases. *Combustion and Flame*, 40:213–219, 1980. doi: 10.1016/0010-2180(81)90124-3.
31. E. J. Jumper and E. J. Fitzgerald. Recent advances in aero-optics. *Progress in Aerospace Sciences*, 37(3):299–339, 2001. doi: 10.1016/S0376-0421(01)00008-2.
32. E. J. Jumper and S. Gordelyev. Physics and measurement of aero-optical effects: Past and present. *Annual Review of Fluid Mechanics*, 49:419–441, 2017. doi: 10.1146/annurev-fluid-010816-060315.
33. E. J. Jumper, M. A. Zenk, S. Gordelyev, D. Cavalieri, and M. R. Whiteley. Airborne aero-optics laboratory. *Optical Engineering*, 52(7), 2013. doi: 10.1117/1.OE.52.7.071408.
34. M. V. Klein and T. E. Furtak. *Optics*. John Wiley & Sons, 2nd edition, 1986.
35. D. T. Kyrazis. Airborne laser laboratory departure from kirtland air force base and a brief history of aero-optics. *Optical Engineering*, 52(7), 2013. doi: 10.1117/1.OE.52.7.071403.
36. J. T.-H. Lo. Synthetic approach to optimal filtering. *IEEE Transactions on Neural Networks*, 5(5):803–811, 1994. doi: 10.1109/72.317731.
37. N. D. Lucca, S. Gordelyev, A. Smith, E. Jumper, M. Whiteley, and T. Neale. The removal of tunnel vibration induced corruption in aero-optical measurements. In *45th AIAA Plasmadynamics and Lasers Conference*, 2014. doi: 10.2514/6.2014-2494.

38. K. P. Lynch, R. Spillers, N. E. Miller, D. R. Guildenbecher, and S. Gordeyev. Aero-optical measurements of a mach 8 boundary layer. In *AIAA AVIATION 2021 Forum*, 2021. doi: 10.2514/6.2021-2831.
39. P.-Y. Madec. Overview of deformable mirror technologies for adaptive optics and astronomy. In *SPIE Astronomical Telescopes + Instrumentation*, 2012. doi: 10.1117/12.924892.
40. V. N. Mahajan. Strehl ratio for primary aberrations: some analytical results for circular and annular pupils. *Journal of the Optical Society of America*, 72(9):1258–1266, 1982. doi: 10.1364/JOSA.72.001258.
41. V. N. Mahajan. Strehl ratio for primary aberrations in terms of their aberration variance. *Journal of the Optical Society of America*, 73(6):860–861, 1983. doi: 10.1364/JOSA.73.000860.
42. A. McAlpine, R. Astley, V. Hii, N. Baker, and A. Kempton. Acoustic scattering by an axially-segmented turbofan inlet duct liner at supersonic fan speeds. *Journal of Sound and Vibration*, 294:780–806, 2006. doi: 10.1016/j.jsv.2005.12.039.
43. J. H. McClellan. Multidimensional spectral estimation. *Proceedings of the IEEE*, 70(9):1029–1039, 1982. doi: 10.1109/PROC.1982.12431.
44. P. A. Mosier-Boss, S. H. Lieberman, and R. Newbery. Fluorescence rejection in raman spectroscopy by shifted-spectra, edge detection, and fft filtering techniques. *Applied Spectroscopy*, 49(5):630–638, 1995. doi: 10.1366/0003702953964039.
45. M. L. Munjal. *Acoustics of Ducts and Mufflers*. John Wiley & Sons, 2nd edition, 2014.
46. A. M. Nightingale and S. Gordeyev. Shack-hartmann wavefront sensor image analysis: A comparison of centroiding methods and image-processing techniques. *Optical Engineering*, 52(7), 2013. doi: 10.1117/1.OE.52.7.071413.
47. R. J. Noll. Zernike polynomials and atmospheric turbulence. *Journal of the Optical Society of America*, 66(3):207–211, 1976. doi: 10.1364/JOSA.66.000207.
48. PCB Piezotronics. 103B02. https://wwwpcb.com/contentStore/docs/pcb_corporate/pressure/products/specsheets/103b02_c.pdf, October 2020. Product Specifications - Revision: C.
49. PCB Piezotronics. 352C33. https://wwwpcb.com/contentStore/docs/pcb_corporate/vibration/products/specsheets/352c33_h.pdf, April 2008. Product Specifications - Revision: H.
50. Peerless. XT25SC90-04. <https://tymphony-driver-files.s3.us-west-1.amazonaws.com/files/driver/pdfs/XT25SC90-04.Rev1.MP1%20-%20Product%20Sheet.pdf>, August 2021. Product Sheet - Revision: 1.
51. Powell. Propagation of a pressure pulse in a compressible flow. *The Journal of the Acoustical Society of America*, 31(11):1527–1535, 1959. doi: 10.1121/1.1907660.
52. R. H. Randall. *An Introduction to Acoustics*. Dover Publications, 1951.
53. O. T. Schmidt and T. Colonius. Guide to spectral proper orthogonal decomposition. *AIAA Journal*, 58(3):1023–1033, 2020. doi: 10.2514/1.J058809.
54. G. Schulze, A. Jirasek, M. M. L. Yu, A. Lim, R. F. B. Turner, and M. W. Blades. Investigation of selected baseline removal techniques as candidates for automated implementation. *Applied Spectroscopy*, 59(5):545–574, 2005. doi: 10.1366/0003702053945985.
55. H. G. Schulze, R. B. Foist, K. Okuda, A. Ivanov, and R. F. B. Turner. A small-window moving average-based fully automated baseline estimation method for raman spectra. *Applied Spectroscopy*, 66(7):757–764, 2012. doi: 10.1366/11-06550.

56. J. P. Siegenthaler. *Guidelines for Adaptive-Optic Correction Based on Aperture Filtration*. Doctoral dissertation, University of Notre Dame, Notre Dame, IN, 2008.
57. J. P. Siegenthaler, S. Gordeyev, and E. Jumper. Shear layers and aperture effects for aero-optics. In *36th AIAA Plasmadynamics and Lasers Conference*, 2005. doi: 10.2514/6.2005-4772.
58. A. E. Smith, S. Gordeyev, and E. J. Jumper. Recent measurements of aero-optical effects caused by subsonic boundary layers. *Optical Engineering*, 52(7), 2013. doi: 10.1117/1.OE.52.7.071404.
59. A. Sommerfeld. *Optics, Lectures on Theoretical Physics*, volume 4. Academic Press, 1954.
60. W. Southwell. Wave-front estimation from wave-front slope measurements. *Journal of the Optical Society of America*, 70(8):998–1006, 1980. doi: 10.1364/JOSA.70.000998.
61. H. A. Stine and W. Winovich. Light diffusion through high-speed turbulent boundary layers. Technical Report RM A56B21, National Advisory Committee For Aeronautics, May 1956.
62. S. L. Valley. Handbook of geophysics and space environments. Technical Report ADA056800, Air Force Cambridge Research Laboratories, April 1965.
63. M. R. Whiteley and . S. Gibson. Adaptive laser compensation for aero-optics and atmospheric disturbances. In *38th Plasmadynamics and Lasers Conference*, 2007. doi: 10.2514/6.2007-4012.
64. A. G. Wilson. Propagation of acoustic perturbations in non-uniform ducts with non-uniform mean flow using eigen analysis in general curvilinear coordinate systems. *Journal of Sound and Vibration*, 443:605–636, 2019. doi: 10.1016/j.jsv.2018.11.023.
65. J. Zhao, H. Lui, D. I. McLean, and H. Zeng. Automated autofluorescence background subtraction algorithm for biomedical raman spectroscopy. *Applied Spectroscopy*, 61(11):1225–1232, 2007. doi: 10.1366/000370207782597003.